Multiple Simultaneous Optical Links for Space-Based Platforms

by

Alexa C. Aguilar

B.S., University of Idaho (2017)

S.M., Massachusetts Institute of Technology (2019)

Submitted to the Department of Aeronautics and Astronautics

in partial fulfillment of the requirement for the degree of

Doctor of Philosophy in Aeronautics and Astronautics

at the

MASSACHUSETTS INSTITUTE OF TECHNOLOGY May 2022

Author .....
Department of Aeronautics and Astronautics
March 7, 2022

Certified by.....
Kerri L. Cahoy
Associate Professor of Aeronautics and Astronautics
Thesis Supervisor

Certified by.....
Eytan H. Modiano
Professor of Aeronautics and Astronautics

Certified by.....
Jose E. Velazco
Chascii CEO and Founder

Accepted by.....
Jonathan P. How
R. C. Maclaurin Professor of Aeronautics and Astronautics
Chair, Graduate Program Committee

Multiple Simultaneous Optical Links for Space-Based Platforms

by

Alexa C. Aguilar

Submitted to the Department of Aeronautics and Astronautics on March 7, 2022 in Partial Fulfillment of the Requirements for the Degree of Doctor of Philosophy in Aeronautics and Astronautics

Abstract

Space-based Free Space Optical Communications (FSOC), or lasercom, offers key advantages over Radio Frequency (RF) communications in bandwidth, Size, Weight, and Power savings, and unregulated spectrum. Theoretical and demonstrated lasercom systems have shown higher data rates for similar or equal SWaP compared to their RF counterparts. New space-based network architectures, such as the broadband constellations currently being deployed by SpaceX and Telesat, among others, leverage optical intersatellite links to increase total system throughput and reduce the number of ground stations which lowers the overall system costs. Beyond LEO, the Artemis program infrastructure includes an optical communication relay between the Orion capsule and Earth, with eventual plans to expand to lunar orbiters for continuous surface coverage. Despite the performance advantages and increasing adoption across applications, state-of-the-art RF communication systems currently outperform lasercom systems in part because of optical communication systems' inability to support multiple simultaneous links. Techniques such as frequency reuse, access methods, and dynamic beam forming enable RF communication systems to work around bandwidth limitations and establish simultaneous links with other nodes within a network (*e.g.*, multiple ground stations, user terminals, etc). This work looks at extending this capability to laser communication systems, evaluates the technology required to support multiple simultaneous optical links, and quantifies the impact of multi-user lasercom within a network configuration. We develop a model to simulate the performance of such a system and verify it against existing models and data. The model is then applied to a LEO and deep-space network scenario which analyzes different access methods, network configurations, and terminal technologies such as fiber amplifiers versus photonic integrated circuits. We perform trade studies to identify the limitations and constraints of the proposed approach. We then make architecture recommendations for each scenario based on key performance parameters. For example, we find for the LEO case, a swarm of four, 6U cubesats can achieve a total system throughput of 12 Gbps with wavelength division multiple access in a mesh network configuration. Additionally, by using a photonic-based transceiver instead of a fiber-based one, an additional ~2.5X savings to mass can be achieved.

Thesis Supervisor: Kerri L. Cahoy
Title: Associate Professor of Aeronautics and Astronautics

Thesis Committee Member: Eytan H. Modiano
Title: Professor of Aeronautics and Astronautics

Thesis Committee Member: Jose E. Velazco
Title: CEO and Founder, Chascii; Former Technical Group Supervisor, JPL

Acknowledgements

I would like to thank my advisor, Kerri Cahoy, for her technical guidance, mentorship, and unfailing support. Through life and research, she has given me opportunities to pursue my interests unbridled. I would not be where I am in my career today without her.

I would like to thank the many people at JPL that provided technical expertise and aided in experimental research pertinent to this work: Leif Scheick and Amanda Bozovich from the Radiation Effects group, Alireza Azizi and Cheryl Asbury from the Parts Engineering and Reliability group, and Siamak Forouhar from the Microdevices Laboratory. I am especially grateful for the extra time and effort Leif Scheick, Alireza Azizi, and Cheryl Asbury graciously gave to mentor me during my time at JPL.

This work would not have been possible without the help of my STAR lab colleagues. I would like to thank those who came before me, and the shoulders of whom this work stands on: Raichelle Aniceto, for the opportunities to study radiation effects and development of lasercom terminal and unwavering support and mentorship throughout my academic career; Emily Clements for her extensive work on laser communication modeling and whom taught me nearly everything I know about statistical link budgets; Rachel Morgan, for her insight into photonic integrated circuits and constant support; Riley Fitzgerald, for his guidance on deep-space orbits.

I want to thank Michael Atakora for his insight into 5G terrestrial networks, and for providing the data required to verify this research.

I would like to thank my thesis committee members for their guidance and mentorship: Kerri Cahoy, Eytan Modiano, and Jose Velazco. Additionally, I want to thank Jose Velazco for the opportunity to use the ISOC terminal design as a reference.

I am immensely thankful for my readers for their involvement and time in vetting this research: Raichelle Aniceto, David Atkinson, and Herbert Hess.

Finally, I would like to thank my family – Francie, Buster, and Makenna – for their encouragement over the years. To my partner, Derek Barnes, there is not enough digital storage in existence to describe nor store my feelings of gratitude and appreciation for everything you've done to support me in this endeavor. My pursuits were and are unrealizable without you.

Contents

List of Figures

List of Tables

Chapter 1

Introduction

1.1 Background

Space-based free-space optical communications (lasercom) has emerged as an enabling technology for both near-Earth and Deep Space communications within the last few decades. In a single, point-to-point link, lasercom provides higher bandwidth and delivers higher power density to achieve similar data rates for less transceiver Size, Weight, and Power (SWaP) compared to Radio Frequency (RF) communications [1]–[3]. Lasercom currently avoids many of the spectrum licensing hurdles associated with operating at RF frequencies. These advantages have led to the development of space-based systems leveraging optical inter-satellite laser (OISL) to form networks for science applications [4], [5], broadband internet [6], [7]–[10], and Lunar and interplanetary communications [11], [12], [13]. Despite its increasing ubiquity, lasercom has yet to address its inability to maintain and field links from multiple concurrent users (nodes) within a network. Given the complexity and dynamics of space-based networks, the development of lasercom systems supporting multiple simultaneous links is essential if it is to compete with current state-of-the-art RF systems.

This chapter motivates the need for multi-user lasercom systems and the development of protocols supporting multiple simultaneous links. A brief background on terrestrial and space-based networks is provided, and comparison between state-of-the-art lasercom vs RF systems is presented. Gaps in the current literature are presented and research contributions of this work are summarized.

1.2 Space-Based Communication Networks

The concept of a satellite communication network that could provide continuous global coverage was popularized in 1945 when Arthur C. Clarke published an essay proposing such a system using

three, geostationary satellites [14]. Since then, architectures have shifted to lower orbits to reduce latency, and distributed systems have gained favor.

The first commercial satellite constellation was designed and launched by Iridium from 1997-2002 with the goal of providing telephone services via satellite. The full constellation was comprised of seventy-seven satellites in LEO that achieved global coverage [15]. While slow adoption and prohibitive costs led to the company's failure, it left a blueprint for next-generation systems to follow.

Several commercial broadband internet satellite constellations ("mega-constellations") have been proposed over the last seven years [3]–[6] with a few beginning deployment [5], [7]. The objective of these systems is to provide global, high-speed, low-latency broadband internet to previously unserved or under-served regions where installing new terrestrial infrastructure is cost prohibitive. Broadband constellations in particular stand to gain significant capacity from the use of inter-satellite links. Portillo [16] shows without crosslinks, constellation capacity is severely limited given the equal distribution of ground stations. Conversely, this means unless constellations have constant access to ground station, which requires wide-spread global deployment, these systems will be unable to support the speed and data volume required to provide high-speed global broadband and jeopardize the underlying business case.

NASA is currently developing a series of LEO swarm missions known as Starling. Starling1, the first series of missions, is a cubesat mission that aims to demonstrate three key capabilities for space-based swarms: 1) robust and autonomous communication protocols; 2) relative navigation without GPS; and 3) autonomous on-orbit software response that doesn't require operator-in-the-loop feedback [17]. These advancements are critical for the development of compact, low-cost satellites capable of coordinated observations.

The Tracking and Data Relay Satellite System (TDRSS) is a constellation of six Geostationary Orbit (GEO) satellites which provide tracking and communications between LEO and ground [18]. Signals are relayed from LEO to TDRSS then White Sands, New Mexico for processing. The Laser Relay Communication Demonstration (LCRD) was launched on December 7, 2021 [19], and aims to relay communications to Earth and LEO from GEO using optical communications [20].

The Mars Relay Network enables lander and rover spacecraft to carry smaller, lightweight antennas to relay information to orbiters instead of directly to Earth. The Mars Reconnaissance

Orbiter (MRO), Mars Odyssey, and MAVEN make up the Mars Relay Network and establish contact with the Deep Space Network (DSN), NASA's ground stations on Earth [21]. Due to orbital geometry constraints and interference from the Sun, constant contact between Earth and Mars is not currently achievable.

1.3 Laser Communications for Space-Based Networks

Lasercom offers increased gain (narrower beamwidth) and increased bandwidth compared with RF [3]. These advantages come at the cost of precision pointing and higher risk of link outages due to weather [3][22]. The latter has driven lasercom applications to inter-satellite crosslinks, where atmospheric disturbances are less prevalent in the channel environment.

From a system perspective, lasercom is an attractive alternative to RF communications. In small satellite platforms, SWaP constraints often limit data rates [23]. SWaP savings for equal or higher performance may translate to lower overall costs per satellite. This is significant when thousands of satellites are slated for launch, such as in the proposed broadband constellations [6]–[10], [24], [25]. Deep space missions are cost and mass limited, and lasercom can provide higher science return per unit cost and mass [26], [27]. Across all classes, lasercom affords additional link security due to the decreased beam footprint size, which reduces the chance of unintended users receiving data [28].

From a regulatory perspective, lasercom licensing may offer cost and time savings. To transmit at RF frequencies, The Federal Communication Commission (FCC) requires authorization prior to launch. The process of securing authorization is time and financially intensive; application fees are upwards of $100,000 per non-geostationary commercial orbit system and may take 2-3 years to get approval [29], [30]. Once approval is granted, authorization is valid for a finite amount of time, giving companies narrow windows for launch and use. Renewal applications are required for continuous use [29], [30]. While approval from entities such as the FAA and Laser Clearing House are required prior to operations, the lack of FCC regulation for lasercom frequencies is significant. These regulations are subject to change and the current FCC license savings may decrease with time.

1.3.1 Demonstrated and Future Lasercom Missions

Several missions across different mission classes have demonstrated optical downlinks and crosslinks within the last few decades. Table 1 summarizes demonstrated missions to date.

The first optical downlink was demonstrated in 1994 by the National Institute of Information and Communications Technology (NICT). Bi-directional links between the Laser Communication Experiment (LCE) payload onboard the Engineering Test Satellite (ETS-VI), a NICT optical ground station in Tokyo, Japan, and the Jet Propulsion Laboratory (JPL) Table Mountain Facility optical ground station achieved ~1-Mbps data rates. The LCE transmitter was a laser diode operating at 830 nm with 13.8-mW output power and used intensity modulation with Manchester coding [31].

In 2001, the first inter-satellite optical link was demonstrated by the European Space Agency (ESA) mission Semiconductor Inter-satellite Link Experiment (SILEX). The mission was comprised of two space-based terminals: one onboard the SPOT-4 French Earth-observation satellite in Low Earth Orbit (LEO), and the other onboard the ESA communication satellite ARTEMIS in Geostationary Orbit (GEO). The LEO-GEO link demonstrated 50 Mbps with NRZ coding at a range of ~40000 km. The LEO transmitter used a GaAlAs laser diode operating at 847 nm with 60-mW output power. The GEO receiver used a 25-cm receiver diameter and Slik Avalanche Photo Diode (APD) [32]. The SILEX ARTEMIS terminal also demonstrated optical downlink to an Optical Ground Station (OGS). Strategically stationed at the Teide Observatory in Tenerife Spain, OGS used a 1-m receive aperture and Si-APD. The transmitter was a GaAlAs diode operating at 819 nm with a 37-mW output power. Data rates up to 2 Mbps using Binary Pulse Position Modulation (BPPM) were achieved [33].

The SILEX mission was later augmented with a JAXA demonstration in 2004. Laser Utilizing Communication Equipment (LUCE), an optical terminal onboard the on the LEO Optical Inter-orbit Communications Engineering Test Satellites (OICETS) mission, demonstrated the first bi-directional optical crosslink from LEO to GEO. The LUCE terminal optical head was 110 kg, and the supporting electronics 30 kg, for a total terminal mass of 140 kg. The transmitter used a GaAlAs laser diode with a 100-mW average output power. The receiver was a 26-cm aperture with an APD. From LEO to GEO (~40000-km range), 50 Mbps data rates were achieved using NRZ modulation, and from GEO to LEO, 2 Mbps were achieved with 2 Pulse Position Modulation (2-PPM) [34].

Two nearly identical Laser Communication Terminals (LCTs) developed by The German Aerospace Center (DLR) flew on the US satellite Near Infrared Experiment (NFIRE) and on the German satellite Synthetic Aperture Radar for Earth Observations (TerraSAR-X) missions. In 2008, the two payloads successfully demonstrated LEO to LEO crosslinks at 5.625 Gbps at a range of 5000 km. Each LCT had a 12.5-cm aperture and optical output power of 700 mW at 1064 nm [35]. A new generation of 5 LCTs were developed and launched on the LEO Sentinel 1A, 2A, and 1B satellites, the GEO Alphasat satellite, and the GEO satellite Eutelsat-B as part of the European Data Relay System (EDRS) campaign. Many LEO-GEO link at 1.8 Gbps were demonstrated between 2014 and 2016 [36], [37]. The second generation LCTs used a 13.5-cm aperture and effective 100-mW output power at 1064 nm [38]. Data rates of 1.8 Mbps were achieved using BPSK modulation [39].

MIT Lincoln Laboratory designed and developed Lunar Laser Communication Demonstration (LLCD), which flew on the NASA Lunar Atmosphere and Dust Environment Explorer (LADEE) mission. In 2013, LLCD demonstrated an optical downlink from Lunar orbit (400,000 km) to the Lunar Laser Ground Terminal (LLGT) in White Sands, New Mexico, making it the longest range demonstrated optical link to date. The space terminal used a 1550-nm, 500-mW transmitter using a Master Oscillator Power Amplifier (MOPA) architecture with an EDFA. The receiver used four, 40-cm aperture telescopes and superconducting nanowire detectors capable of near-single photon counting. Downlink speeds of 622 Mbps were demonstrated using 4-PPM modulation [40], [41].

In 2014, NASA JPL demonstrated an optical downlink from the ISS using the Optical PAyload for Laser Communications System (OPALS) and JPL's Optical Communication Telescope Laboratory (OCTL) receiver. OPALS used a 1550-nm, 2.5-W transmitter, and OCTL was equipped with 1-m

Table 1: Demonstrated Lasercom Systems and Key Parameters

Name (Year)	Link Parameters		Transmitter Parameters			Receiver Parameters		
	Type	Max Range [km]	Terminal Mass [kg]	Optical Output Power [mW]	Max Data Rate [Mbps]	Number of Simultaneous Links	Aperture Diameter [cm]	Detection Type
LCE (1994)	Space-Ground	38700	22.4	13.8	1.024	1	150	Direct
SILEX (2001)	LEO-GEO	38000	150	60	50	1	25	Direct
SILEX (2001)	GEO-Ground	38000	157	37	2	1	100	Direct
LUCE (2004)	LEO-GEO	38000	140	200	50	1	25	Direct
LUCE (2004)	GEO-LEO	38000	157	37	2	1	26	Direct
LCT (2008)	LEO-LEO	5100	35	700	5.625	1	12.5	Coherent
LCT (2008)	LEO-Ground	1000	35	700	5.625	1	1	Coherent
LLCD (2013)	Lunar-Ground	400000	30	500	622	1	40 (x4)	Direct
OPALS (2014)	LEO-Ground	700	50	2500	50	1	1	Direct
EDRS LCT-Gen 2 (2014 & 2016)	LEO-GEO	45000	60	100	1800	1	13.5	Coherent
OSIRIS v2 (2016)	LEO-Ground	500	1.65	1000	1000	1	40	Direct
OSIRIS v1 (2017)	LEO-Ground	600	1.3	1000	1000	1	40	Direct
OCSD (2018)	LEO-Ground	500	2.31	2000	200	1	40	Direct

telescope aperture. A maximum data rate of 50 Mbps was achieved using On-Off Keying (OOK) modulation [42], [43].

In tandem with small satellite platforms, compact, high-performance lasercom terminals began to emerge in the mid 2010's. In 2015, NICT demonstrated laser downlinks using the Small Optical Transponder (SOTA) onboard the LEO Space Optical Communications Research Advanced Technology Satellite (SOCRATES). Two laser diode transmitters were used: one at 976 nm with a ~250-mW optical output, and one at 1549 nm with ~40-mW optical output. The 1-m Koganei ground station established a 10-Mbps link with SOTA [44], [45].

In 2016, DLR began the optical communication demonstrations on small platforms as part of its Optical Space Infrared Downlink System (OSIRIS) program. The LEO Earth observation BiROS satellite was launched with an OSIRIS v2 terminal. A year later, OSIRIS v1 terminal launched on the Flying Laptop satellite developed by the University of Stuttgart. Both terminals were equipped with 1550-nm, 1-W output power transmitters that used a laser diode seed laser and EDFA. OSIRIS v1 demonstrated a 200 Mbps downlink to DLR's 40-cm ground station. OSIRIS v2 can support data rates up to 1 Gbps, however, performance validation could only be performed via telemetry readings, and as of 2019, no optical downlink has been demonstrated [46],[47].

In 2018, NASA and the Aerospace Corporation demonstrated optical downlinks from two CubeSat missions: AeroCube 7-B and 7-C, also known as the Optical Communications and Sensors Demonstration (OCSD). Both terminals were built using a MOPA architecture with an Ytterbium Doped Fiber Amplifier (YDFA), meaning the center wavelength was at 1064 nm (vs. EDFA at 1550 nm). The downlinks were performed at 2-W output power. The ground station was a 40-cm aperture receiver and Si-APD detector located in El Segundo, CA. Data rates of 50, 100, and 200 Mbps have been demonstrated using OOK modulation [48].

SpaceX recently began launching a new generation of Starlink satellites to increase its broadband constellation capacity. In late 2021, new Starlink satellites were equipped with lasercom terminals used for OISL. Though successful tests have been documented, little is known about the current state of the program or quantitative performance [49].

There are several efforts currently underway from industry, academic institutions, and government programs to develop and deploy space-based lasercom systems. New programs are

increasingly appearing as the overall lasercom market is predicted to grow by 26.98% from 2021-2031 [50]. We discuss a subset of ongoing projects below.

Laser Infrared CrosslinK (CLICK) mission is ongoing Cubesat project at the Massachusetts Institute of Technology (MIT). CLICK-A (formerly the Nanosatellite Downlink Experiment, NODE), is an optical downlink experiment, while CLICK B/C is a crosslink experiment. CLICK-A aims to demonstrate 50 Mbps downlink and CLICK B/C will show full duplex communication with two, 10 Mbps links. CLICK B/C also aims to demonstrate precision ranging using an onboard Chip Scale Atomic Clock (CSAC) [23], [51], [52].

The Intersatellite Optical Communication (ISOC) is a novel omnidirectional optical terminal developed at JPL. A spherical arrangement of detectors and lasers enable full-sky coverage in both transmit and receive Field of View (FOV). The goal of ISOC is to demonstrate Angle of Arrival (AoA) tracking and maintain multiple simultaneous links [53], [54].

The Deployable Optical Receiver Array (DORA) Cubesat is a joint mission between the University of Arizona and JPL. DORA is equipped with four deployable receiver panels to increase the effective receiver size on the Cubesat terminal, and a single transmitter for downlink. Like ISOC, the goal of DORA is to demonstrate AoA tracking and 1 Gbps downlink [55].

Terabyte Infrared Delivery (TBIRD) is Cubesat currently under development by NASA and MIT Lincoln Laboratory. TBIRD plans to use commercial Wavelength Division Multiplexing (WDM) components to achieve 200-Gbps downlink data rates. Small aperture ground receivers on the order of 20 to 40 cm with commercial adaptive optics are also planned [56]–[58].

DLR is developing the next generation of OSIRIS terminals with OSIRIS v3 and OSIRIS4Cubesat which launched in January 2021 and program updates are expected imminently. OSIRIS v3 aims to demonstrate 10-Gbps downlinks from the ISS' Bartolomeo platform. OSIRIS4Cubesat is a 10 x 10 x 3 cm^3 (<1U) platform capable of 100-Mbps downlinks [47].

Tesat, a Germany-based company, is producing next-generation LCTs for commercial applications. For example, CubeLCT touts 100 Mbps downlinks in a <1U platform and SmartLCT is designed specifically for LEO applications, with 1.8 Gbps per second over 45,000km ranges advertised [37], [59]–[61].

Mynaric was recently selected by the DARPA's Space Based Adaptive Communications Node (Space-BACN) program to build reconfigurable, multi-protocol optical terminals [62]. Before extending to US markets, Mynaric was established in European markets as a lasercom terminal manufacturer. Current efforts underway include optical ground station and LEO terminals capable of 10-Gbps links over 45000-km ranges [63].

Telesat is one of the notable satellite broadband constellation developers due to the scale of their planned deployment [6], [24]. Named "Lightspeed", Telesat's constellation is notably smaller than other proposed broadband constellations, and requires OISL to maintain low-latency and system capacity. Thales Alenia Space was recently selected to deliver the constellation's optical terminals [64].

NASA launched the Laser Communication Relay Demonstration (LCRD) mission onboard the GEO satellite STPSat-6 in December 2021. This LLCD follow-on mission aims to demonstrate on-orbit optical relay services between LEO, GEO, and Earth. Two optical terminals, including electronics and modem, are connected via switch for real-time relay services. Both PPM and DPSK modulation formats are supported, with 311-Mbps and 1.244-Gbps data rates achievable, respectively [12]. The Integrated Low-Earth Orbit LCRD User Modem and Amplifier Terminal (ILLUMA-T) is the corresponding LEO terminal that will be hosted on the ISS, which is also being developed by NASA and MIT Lincoln Laboratory. From ILLUMA-T to LCRD, DPSK links of 1.244 Gbps are expected; from LCRD to ILLUMA-T, 51-Mbps links are expected [65].

NASA is also developing a number other optical communication technology to support the Artemis program. The Orion Multi-Purpose Crew Vehicle (MPCV) will be equipped with the optical terminal Orion EM-2 Optical Communications Demonstration (O2O) to support crewed Lunar flights. Direct to Earth communications with 80-250 Mbps downlink and 20-Mbps uplink rates using PPM will be supported. While a S-band link is the primary communication system for MPCV, the optical link will be used for high-rate data transfers, such as video streaming [13], [65].

Beyond Lunar exploration, NASA is developing a lasercom terminal for deep space. The Deep Space Optical Communication terminal (DSOC) is a technology demonstration payload onboard the PSYCHE spacecraft, which will make its way to the asteroid belt after launch. The objective of DSOC is to show 10-100 times data rate improvement over current RF systems without

incurring additional SWaP. From 2.6 AU, DSOC aims to demonstrate 2-Mbps downlink to Earth [66]–[68].

1.3.2 Photonic Integrated Circuits

There is significant overlap between early terrestrial fiber systems and current lasercom systems. Erbium Doped Fiber Amplifier (EDFA) transmitters and direct-detect receivers were initially used in the early 1980's for long-haul fiber networks and are commonly used in today's lasercom architectures. However, terrestrial systems have evolved considerably since the 1980's. Modern long haul, robust, high-capacity fiber networks have been made possible by several key technologies, including Photonic Integrated Circuits (PICs). We evaluate the viability of PICs for future space-based based as they are vital in Earth-based optical networks.

Like electronic ICs, PICs are semiconductor devices that combine multiple discrete components into a single monolithic chip. Commercial monolithic PICs emerged in the mid 2000's as a breakthrough solution for the telecommunication industry, enabling network scaling and power efficiency unattainable using discrete optics and electronics. Lasers, modulators, multiplexers, switches, photodetectors, waveguides, demultiplexers, demodulators, and other optical components could be placed on the same wafer chip and co-packaged together. Paired with large-scale production, monolithic PICs enabled the high-bandwidth optical systems used today in long-haul fiber networks, data centers, and cloud computing servers [69], [70]. Specifically, these devices enabled scalable optical architectures that could support Dense Wavelength Division Multiplexing (DWDM) and coherent modulation schemes. Coherent modulation can achieve higher data rates than direct-detect schemes by utilizing both amplitude and phase information whereas direct-detect uses amplitude-only. Both components play a key role in supporting fiber networks; DWDM components allow simultaneous transmission of multiple signals at different wavelengths in the same physical medium with little loss or interference, which increases the capacity of a single fiber. Paired together, these two changes to the 1980's fiber architecture gave way to the Terabit Per Second (Tbps) fiber links used today for broadband internet [71]. To realize the full potential of lasercom for space-based networks, a similar breakthrough is needed.

1.3.3 Medium Access Protocols

In order to address the emergence of networks in the 1970's and 1980's, the International Organization for Standardization (ISO) adopted a conceptual framework standard to allow wide-

spread interoperability. The Open System Interconnect (OSI) 7-layer model enabled diverse nodes to interact on the network by defining protocols at each layer. Table 2 shows a diagram of the OSI model and summarizes the functions of each layer.

Table 2: OSI Seven-Layer Network Model [72], [73]

	Layer		Function	Example Protocol or Standard
7	Application		Display received, decoded data to end-user.	Advanced Message Queuing Protocol (AMQP), Hyper Text Transfer Protocol (HTTP)
6	Presentation		Converts and translates data types to system-dependent data type.	File Transfer, Access, and Manager (FTAM)
5	Session		Manges opening and closing temporary end-user application sessions. Responsible for authentication and authorization.	Real-time Transport Control Protocol (RTCP)
4	Transport		Reassembles frames in sequence, removes duplicate frames, requests missing or erroneous frames.	Transmission Control Protocol (TPC), User Datagram Protocol (UDP)
3	Network		Maps the physical path for data based on network conditions, service priority, and routing.	Internet Protocol v4/v6 (IPv4/v6)
2	Data Link	Logic Link Layer	Sequences frames, acknowledges and resends unacknowledged frames.	I2C, IEEE 802.11
		Media Access Control	Tracks and sends frames to physical address. Corrects errors from physical layer. Manages access to the physical layer.	
1	Physical		Defines the electrical, optical, mechanical, and other physical specifications to interface with the network medium. Transmits and receives the physical signal.	USB, SPI, Bluetooth, Ethernet 1000BASE-X

Within the framework of the OSI model, this work is concerned with the physical layer and the data link layer, specifically the Media Access Control (MAC) sublayer. These two layers work closely together and often are defined in the same standard, such as with I^2C. In free-space optical communication, the physical layer definition is the free-space optical channel and use of optical wavelengths. MAC layer protocols used in satellite networks can be categorized into two broad class: channelization and random access.

Channelization protocols assign a physical attribute, either time, bandwidth, or code, to each user on the network to ensure data does not collide or interfere. Time Division Multiple Access (TDMA) assigns a time slot to each user in which they may transmit. Current communication satellite standard DVB-RSC2 use Multi Frequency TDMA (MF-TDMA) to support multiple, bursty transmissions from user terminals to large gateways [74], [75]. Frequency Division Multiple Access (FDMA) assigns each user a unique frequency (or wavelength) that they may use to transmit. Space Division Multiple Access (SDMA) provides each user with a unique location to transmit from. Modern phased array antennas field multiple simultaneous links from different users using a combination of FDMA and SDMA; phased array antennas are typically segmented into discrete parts, each with a unique frequency. When the segmentation pattern is large, frequencies can be reused on the same antenna to support different links at the same frequency. Code Division Multiple Access (CDMA) assigns each user an orthogonal sequence to encode or envelope transmitted data, however, requires additional computational resources to resolve unique users and data streams [76].

Random access methods do not allocate channel resources to users, but rather allow equal, random access to the channel medium. Pure Aloha allows users to transmit data whenever it is available. It does not monitor the channel for activity and has a high probability of a transmission colliding with other user transmissions, meaning data is often lost. Slotted Aloha attempts to overcome this problem by assigning discrete time slots to the channel wherein users can only transmit at the beginning of each timeslot and has been proposed for GEO communication satellites. Carrier Sense Multiple Access (CSMA) monitors the channel for activity and allows users to transmit when the channel appears clear. A variant known as CSMA Collision Avoidance (CSMA-CA) defers transmission for a random interval if the channel is busy and is used in modern WiFi network standards [76].

1.3.4 Comparison to RF Communication Systems

In practice, RF communications are often used in scenarios where multiple simultaneous links must be maintained. The methods developed to achieve this capability enable effective system throughput exceeding that of single point-to-point links.

To illustrate the performance advantage of space-based multiuser lasercom, a LEO case study is presented. A downlink budget incorporating multiuser support are used to compare three

systems: multiuser RF, point-to-point lasercom, and multiuser lasercom. System parameters documented in existing literature are used to determine the Carrier-to-Noise ratio (C/N).

$$\frac{C}{N} = \frac{P_{rx}}{P_n} \tag{1}$$

Where P_{rx} is the power seen at the receiver determined by Friis transmission equation in watts and P_N is the noise power in the system in watts.

$$P_{rx} = \frac{P_{tx}G_{tx}G_{rx}\lambda^2}{(4\pi R)^2} \tag{2}$$

Where P_{tx} is the transmit power in watts, G_{tx} and G_{rx} are the gain of the transmitter and receiver, respectively, and are unitless in linear scale, lambda is the wavelength of the signal in meters, and R is the separation distance in meters. For simplicity, the noise power is assumed to meet the fundamental performance limits of each system. For RF, Johnson (thermal) noise serves as the lower bound; for lasercom, quantum shot noise is the lower bound [1].

$$P_n = \begin{cases} kT_{sys}B, & RF\ system \\ hvB, & Optical\ system \end{cases} \tag{3}$$

Where k is Boltzmann's constant, T_{sys} is the effective system temperature including the antenna and receiver temperature in Kelvin, B is the system bandwidth in Hertz, h is Planck's constant, and v is the frequency of the selected wavelength in Hertz.

We assume the channel follows a Gaussian distribution. Once the carrier to noise ratio is calculated, the Shannon capacity limit is used to determine the maximum data rate a system can support.

$$R_{max} = Blog_2\left(1 + \frac{C}{N}\right) \tag{4}$$

A new metric called total system capacity is determined by the product of estimated number of users and the capacity.

$$R_{sys} = n_{users} R_{max} \tag{5}$$

The final metric, normalized capacity, is calculated by dividing the optical communication capacity by the RF capacity.

$$R_{norm} = \frac{R_{sys|optical}}{R_{sys|RF}} \tag{6}$$

The ratio in Eq. 6 summarizes two key system attributes: whether a system can increase data rates compared to RF, a core driver for lasercom (> 1 no, <1 yes) and the magnitude of performance difference.

Best- and worst-case scenarios are analyzed to capture system performance range. Baselined systems have slightly different orbital parameters but are all classified as LEO missions. To simplify the problem, a minimum range of 450 km and maximum range of 1000 km is assumed. This corresponds to a minimum elevation angle of 20° and a 450 km orbit altitude. Atmospheric losses are wavelength dependent and are taken from ITU atmospheric gas attenuation [77] for RF systems and [3] for optical.

1.3.5 RF Subsystem Parameters

In May 2019, SpaceX began deploying its "mega-constellation" known as Starlink [49]. The system will provide broadband internet service with pole-to-pole coverage using a total of 4409 satellites distributed between 4 different altitudes and inclinations and 75 orbital planes [25]. SpaceX has been allocated spectrum by the FCC in V-band, Ka-band, and Ku-band. In their FCC filings, SpaceX discloses that each space terminal regardless of frequency use will be equipped with a phased array with electronic beam steering and beam forming functionality at an EIRP of 31 dB (Ku-band) [8], [9], [25]. Table 3 summarizes the Starlink constellation parameters.

Table 3: Starlink Constellation Parameters from [8], [9], [25]

Altitude (km)	550	1110	1130	1275	1325	345.6	340.8	335.9
Inclination (°)	53	53.8	74	81	70	53	48	42

Frequency Band	Ka/Ku	Ka/Ku	Ka/Ku	Ka/Ku	Ka/Ku	V	V	V
Orbital Planes	24	32	8	5	6	2547	2478	2493
Satellites per Plane	66	50	50	75	75	1	1	1
Total Satellites	1584	1600	400	375	450	2547	2478	2493

This analysis uses user-downlink parameters outlined in the Ku- and Ka-band FCC filing [8] for comparison. Each spacecraft will use Right Hand Circularly Polarized (RHCP) Ku-band (10.7 GHz – 12.7 GHz) for return downlinks (satellite-to-user), with a minimum of 8 spotbeams available for dynamic allocation. This analysis uses the mean frequency value (11.7 GHz) to estimate performance. By incorporating spatial diversity in transmit beams, a frequency reuse factor of about 4 is achievable, meaning each center frequency allocated for downlink may be used 4 times without significant performance degradation due to interference [78]. For simplicity, this analysis assumes one Ku-band frequency is used 4 times within the space terminal, and Single Beam Per Carrier (SBPC) service is used. Note in practice more than one user may access a channel at a given center frequency. Standards such as DVB-S2 use Frequency Division Multiplexing (FDM) to accommodate multiple users by subdividing a carrier frequency band into smaller segments and assigning segments to users [79].

SpaceX also filed for a blanket license to use up to one million flat-panel user antennas [7]. While antenna gain specifications are available within the application, noise temperature is not. As a proxy, it is assumed user terminals will have similar or better noise performance than available Very Small Aperture Terminals (VSATs) and [80] is baselined. Table 4 lists the parameters used for this analysis.

1.3.6 Single User Optical System Parameters

OCSD, a downlink Cubesat developed by NASA and the Aerospace corporation, used a single user, current state of the art lasercom system [81]. The transmitter was a Master Oscillator Power Amplifier (MOPA) architecture that used an optical power amplifier fed by a seed laser to produce a

Table 4: Starlink System Parameters [7], [9]

Transmitter	
Antenna	Phased array, 8 dynamic spot beams
EIRP	31 dBW
Receiver	
Antenna	Flat panel array
Gain	33.2 dBi
System	
Frequency	11.7 GHz
Number of Users	4

2 W optical output power at 1064 nm [48]. The output beam was propagated through a single telescope aperture with body-fixed optics. The beam divergence was intentionally oversized beyond the diffraction limit to compensate for the spacecraft pointing error, and no active actuation was used for fine pointing. Coarse pointing was established using a star tracker and despite the additional power dispersion, data rates up to 100 Mbps were recorded at BER of 10^{-6} at 450 km ranges. The optical ground station was a 40 cm telescope retrofitted with a Silicon APD and operated by the Aerospace Corporation [48]. Table 5 lists the parameters used for this analysis.

Table 5: OCSD System Parameters [48]

Transmitter	
Output Power	2-4 W
Divergence	2.7 mrad
Gain	63.41 dBi
Receiver	
Aperture Size	40 cm
Gain	121.45 dBi
System	
Wavelength	1064 nm
Number of Users	1

1.3.7 Multi-user Optical System Parameters

JPL is developing a quasi-omnidirectional laser communications terminal for a 6U mission known as the Intersatellite Optical Communicator (ISOC) [53], [54], [82]. With a truncated

dodecahedron chassis, an array of 32 miniature transmitters is fitted into each facet, and detectors are housed at each vertex. The mission objectives include maintaining multiple simultaneous 1 Gbps links at >100km crosslink ranges as well as an optical downlink. The baseline ISOC configuration is in a LEO swarm with a total of 4 spacecraft (mission details are found in Chapter 4). For this analysis, it is assumed one terminal can support multiple simultaneous links between all spacecraft and the ground station totaling 4 users. It is assumed the system is power limited to 1 W total optical power output, with 250 mW allocated per link, and the divergence achieves the diffraction limit. The same optical ground station used for OCSD is assumed.

Table 6: ISOC System Parameters [53], [54], [82]

Transmitter	
Output Power	250 mW
Divergence	576.11 urad
Gain	76.83 dBi
Receiver	
Aperture Size	40 cm
Gain	121.45 dBi
System	
Wavelength	850 nm
Number of Users	4

The downlink analysis is summarized in Table 7.

This analysis reaffirms point-to-point link capacity is higher with optical systems, however, when factoring in multiple users, the maximum capacity of state-of-the-art lasercom systems is a fraction of RF. OCSD's normalized capacity is less than 1, meaning it cannot compete with a single Starlink satellite despite having a higher point-to-point data rate. With Starlink supporting multiple users, OCSD offers about 40% of the data throughput. ISOC however, even with a larger beam divergence and lower output power, can support roughly 7-8 times more capacity than Starlink. In order to compete with state-of-the-art RF systems, multiuser lasercom is required.

1.4 Enabling Multiuser Lasercom Systems

As space-based networks continue to expand and employ lasercom to connect spacecraft, protocols defining access methods, novel architectures, and technology infusion are needed to support these systems. Methods for quantifying the system-level impact of relevant parameters are required.

Table 7: LEO Downlink Case Study Performance

System		SpaceX Starlink		OCSD		ISOC		Units
		Best Case	Worst Case	Best Case	Worst Case	Best Case	Worst Case	
Range		4.50E+05	1.00E+06	4.50E+05	1.00E+06	4.50E+05	1.00E+06	m
Frequency		1.17E+10	1.17E+10	2.81E+14	2.81E+14	3.52E+14	3.52E+14	Hz
Wavelength		0.26	0.26	1.06E-06	1.06E-06	8.50E-07	8.50E-07	m
Target BER		1.00E-06	1.00E-06	1.00E-06	1.00E-06	1.00E-06	1.00E-06	
Pointing Loss		-0.50	-0.50	-3.00	-3.00	-3.00	-3.00	dB
Propagation Loss		-146.90	-153.83	-254.51	-261.45	-256.46	-263.40	dB
Atmospheric Loss		-1.86	-3.72	-2.22	-3.00	-2.22	-3.00	dB
Transmit Power				6.02	3.01	-6.02	-10.00	dBW
Transmit Gain	*EIRP*	31.00	31.00	63.41	63.41	76.83	76.83	dBi
Losses				-3.00	-3.00	-3.00	-3.00	dB
Bandwidth		2.50E+08	2.50E+08	6.00E+08	6.00E+08	1.00E+09	1.00E+09	Hz
Receiver Gain		33.20	30.60	121.45	121.45	123.40	123.40	dBi
Noise Temp		41.00	56.00	-	-	-	-	K
System Temp		166.00	181.00	-	-	-	-	K
Noise Power		-122.42	-122.04	-99.52	-99.52	-96.32	-96.32	dBW
Boltzmann's Constant		-228.60	-228.60	-	-	-	-	dBW/Hz-K
Power Received		-85.06	-96.45	-71.85	-82.58	-70.47	-82.17	dBW
C/N		37.36	25.59	27.67	16.94	25.85	14.16	dB
Shannon Limit		3.10	2.13	5.52	3.39	8.59	4.76	Gbps
Number of Users		4	4	1	1	4	4	
Capacity (Max)		12.41	8.50	5.52	3.39	34.37	19.03	Gbps
Capacity (Norm)		1	1	0.44	0.40	6.23	5.61	-

1.4.1 Media Access Protocols for Lasercom Systems

Several efforts have been made to define MAC protocols and corresponding algorithms to enable space-based networks. Terrestrial fiber communications support multiusers and high data rates using WDM and WDMA [64],[65]. Passive Optical Network (PONs) components can multiplex and demultiplex wavelengths using Arrayed Waveguide Gratings (AWG). Active components utilizing photonic technology accomplish the same function but in smaller monolithic systems [83]i. Jiang et al. show a single telescope fitted with a fisheye lens can support multiple wavelengths at separations up to 400 km . Six wavelengths each have a dedicated detector and filter to separate the incoming signal. The receiver uses Space Division Multiplexing (SDM) assuming that within the +/- 60° field of view of the receiver, transmitters are sufficiently spatially diverse and the corresponding signals nominally never meet within the telescope optical path. Using WDMA in this way is not scalable to large numbers of users as dedicated paths with discrete optics are used to differentiate users. An alternative to discrete components is an integrated solution such as PICs. There is hesitancy to use photonics in space-based systems because the free-space coupled technology is relatively new, making the Technology Readiness Level (TRL) low and the flight heritage non-existent.

Optical phased array technology has shown promise for multiuser lasercom support. Miniscalco et. al [84] built and tested a custom liquid crystal phased array transceiver supporting two users during the same experiment. The transmit beam electronically steered to communicate with spatially diverse users during an assigned timeslot (STDMA). Precise pointing is required to rapidly hop between users, and persistent acquisition and tracking of the idle node was implemented. MIT Lincoln Laboratory proposed a telescope receiver array each fitted with a fast-steering mirror and an array of APDs [85]. The concept uses individual elements to increase the effective size of the aperture. Multiuser support and multiple access methods are not explicitly discussed in this work, but this architecture may be utilized for multiuser lasercom through TDMA, SDMA, WDMA (with the addition of filters), CDMA, or a combination.

Fox et al. developed one of the first gimbal-less optical terminals for a GEO satellite that used a single telescope designed to underfill a detector array, capitalizing on spatial diversity in the image plane to detect and respond to users in LEO (SDMA). This architecture was a point-to-multipoint system and the LEO satellites did not support multiple access [86].

Optical Code Division Multiple Access (OCDMA) was initially proposed by Salehi in 1989 for fiber communications [87]. Each user is assigned an optical signature designed with low out-of-phase autocorrelation and low cross-correlation. Users may then transmit simultaneously across a shared channel and the receiver detects the desired user. This has been extended to terrestrial free-space systems to support data delivery to end-users (last-mile) [88]–[90] and wireless mesh networks [91]. OCDMA has been proposed for intersatellite links [92], with [87] applied specifically to CubeSats with hardware demonstration. While the latter is a comprehensive analysis of OCDMA in small satellites, the accompanying hardware is not omnidirectional and multiuser detection and applications to lasercom protocols are not discussed.

Current DVB-S2 protocols define the modulation and coding schemes for MPEG file format broadcast. It also specifies ground terminals to multiplex signals using time division and frequency division to increase total data throughput to ground gateways. This approach specifically defines methods for satellite broadcasting to ground and ground-to-ground links, but does not mention satellite-to-satellite links [74], [79].

Hybrid CDMA/TDMA protocols for Cubesats have been proposed by [93], [94], [95]. Satellite clusters using TDMA and CDMA uplinks, downlinks, and crosslinks are proposed. Each cluster has a master satellite that receives signals from slave satellites or other master satellites. The hybrid system throughput and delay are compared to a CDMA-only and CSMA/RTS/CTS protocols and shows the hybrid system is superior. Simulations performed in INET showed anomalies for ground station passes where packet losses inexplicably occurred, and no overall supported data rate is presented [95].

1.4.2 Technology for Lasercom Transmitters

Transmitters are a key segment of the lasercom system as they typically determine the unique characteristic that identifies them from other users on a network. Historically, lasercom terminals are based on MOPA architectures wherein a dedicated fiber amplifier is responsible for amplifying a modulated signal to power levels needed to transmit over the free-space channel. Fiber amplifiers achieve the high-peak power levels required for PPM modulation and thus have been widely adopted for new architectures as well [1], [96]–[98]. Although fiber amplifiers have made efforts to miniaturize, they still remain bulky components and consume much of the mass and size budget for small satellites [51], [99]. It has been documented that the useable bandwidth of a single EDFA is 10% of its intrinsic bandwidth, resulting in ~3.5 nm of bandwidth [100]. In order to support access

methods such as FDMA (WDMA), multiple amplifiers would be required multiple seed lasers with a wideband amplifier is required. Gain performance varies across the full bandwidth, and certain users with assigned colors may experience decreased performance. A multi-amplifier transmitter architecture is mass-prohibitive for small satellite platforms, and mass-inefficient for larger platforms.

Vertical Cavity Surface Emitting Lasers (VCSELs) have been proposed for short range, ground-based free-space optical communications [101]–[104], and space-based systems [105]. Small semiconductor lasers can be directly modulated, are straightforward to implement, and have less mass than fiber amplifier counterparts. In practice, semiconductor lasers exhibit low extinction Ratio (ER), meaning there is little difference between the output levels of the laser when it is on versus off, and produce additional transient spectra when driven at speeds > 10s of GHz. Both factors contribute noise to the link and limit the overall receiver sensitivity [1]. For links requiring high data rates with photon-level sensitivity, these characteristics may be prohibitive.

Strides in adapting PICs for space-based transmitters are currently underway. A full overview and description of radiation environments and effects are out of scope of this work, however, the reader is directed to Edmunds et. al for additional information [106]. Monolithic InP transmitters are power-limited to a ~100-mW output and suffer from poor beam quality [107],[108], and performance in the space environment is largely unknown [69], [70], [109], [110]. Freedom Photonics have demonstrated >9 W continuous output power at 980 nm with high beam quality, but high frequency modulation performance is unknown [111]. A 3-W, 1550-nm diode laser designed by Freedom Photonics has also been demonstrated for LiDAR applications, but like the 980-nm device, higher frequency modulation performance is not reported [112]. Tzintzarov [113] showed passive PIC structures such as waveguides are tolerant to transient effects induced by heavy-ions. Gambini [114] showed that for devices similar to the Zhao transmitters [107],[108], wavelength shifts up to 1 nm can be expected for Total Ionizing Dose (TID) levels representative of 3-year LEO missions. Full device characterization across other types of radiation was not performed. Device type and structure are unspecified, however, Dean [115] showed parametric shifts such as lasing threshold will shift as a function of absorbed Total Non-Ionizing Dose (TNID). While a better understanding of radiation effects on PICs must be developed, it is clear active PIC devices are sensitive to radiation. The limited data available can provide a starting point for system-level mitigation strategies to reduce these effects while enabling a space-based optical terminal that can support higher data rates than current state-of-the-art.

1.4.3 System Modeling

To quantify the system-level performance of a space-based system, analysis tools beyond link budgets are needed. Efforts to quantify the impact of protocols to a system have been performed. IEEE standards for space links are beginning to emerge. 802.11b is 802.11 for Wireless Local Area Networks (WLAN) modified for intersatellite links. Inter-frame space time is adjusted to accommodate longer propagation delays experienced in ISL vs WLAN (3 km vs 300 m). Analysis showed as satellite separation and number of nodes increases, delays for PCF and DCF are 100s of ms and neither adaptation can meet 1 Mbps [116].

Developers of Nanolink-55, a data link layer protocol designed for CubeSat applications and optimized for low bandwidth-delay product, determined the maximum supported data rate of their protocol is 9.6 kbps. While this protocol can adapt to dynamic physical channel conditions, the low rate is not conducive for optical links [117].

Atakora and Chenji have proposed a novel algorithm to support users capable of multicasting, wherein a transmitter broadcasts several narrow beams, in a hybrid RF and optical network. They show data rates of ~45 Gbps can be supported with separation ranges up to 150 m. Algorithm performance in space-based environments, which experience 1000's of km separations, is unknown [118]. Extending the algorithm to satellite networks wherein ranges and relative velocities between nodes are orders of magnitude higher may be useful in developing protocols for lasercom systems.

Studies on space-based systems and capacity have been performed. Portillo [16] developed a model to quantify the network performance between different proposed constellations and the impact of ground station placements to capacity. Three fixed rates are assumed for intersatellite links, but methods to enable multiple simultaneous crosslinks or additional analysis to support the crosslink data rates is not shown.

Clements [28] developed a probabilistic model to quantify risks associated with technology adaptations for Cubesats, and accepting more risks in lasercom Cubesats can yield higher performance than traditional system engineering methods. Downlink rates of 50-Mbps are estimated using the CLICK-A architecture. Point-to-point simulations are performed, but multiple simultaneous links are not discussed.

Velazco [53], [54], [119] has developed an optical transceiver suited for multiple simultaneous links, which is a key capability required for the ISOC Q4 mission. Protocols supporting these links have not been defined, and the use of multiple VCSELs within the payload volume at the advertised data rate have not been demonstrated.

1.4.4 Contributions

To summarize the current gaps, lasercom systems are unable to support multiple simultaneous users without adding a dedicated lasercom transceiver for each user, which is mass-inefficient and often prohibitive for small satellite platforms. Technology to enable multiple access protocols for multiuser lasercom, such as PICs, have not yet been used on-orbit for free space optical intersatellite transceiver technology despite performance benefits. The performance of lasercom systems supporting multiple simultaneous links through access protocols and novel technology is unknown.

In this thesis, we address the gap in current laser communication architectures to support multiple simultaneous users by analyzing the performance effect of introducing multiple access methods within networks. We perform trade studies between protocols to understand the limitations and considerations of each. We survey the current state-of-the-art laser communication technologies and address the needs of a lasercom transceiver supporting multiple simultaneous links versus the available hardware. We evaluate the performance of several existing systems to show improvements to current state of the art, as well as new systems to demonstrate applications to a range of case studies.

The resulting contributions of this thesis are:

1. A protocol supporting space-based multiuser laser communications

2. Design and analysis of a space-based laser communication system supporting multiple users

3. Verification of contributions 1 and 2 through simulation

1.5 Thesis Organization

The remainder of this thesis is organized as follows: Chapter 2 is the overview of approach and introduction of the model developed to evaluate the comparisons between protocols. Here the trades of each access method and the limitations of each are investigated. Chapter 3 is a comparison of the model to current state-of-the-art systems. Chapter 4 is the evaluation of different scenarios enabled by multiple user optical systems as well as a proposed optical terminal for each scenario. Chapter 5 presents a summary of the results and future work.

Chapter 2

Approach

This chapter describes the approach for analyzing lasercom systems using different medium access schemes and discusses the high-level trades such as network architectures, access selection, and technology trades. Network formation over the course of an orbit is analyzed as well as the process in which links are established. The simulation is time-based and that accounts for orbital dynamics, channel dynamics, and resource limitations (e.g., mass and power). The model is validated against existing systems in Chapter 3, and new findings for proposed systems are discussed in Chapter 4.

2.1 Model Setup

An overview of the model is presented in Figure 1. A time series of data representing a given mission, as well as the desired network, access, and technology configuration are specified as inputs. The model then determines relative positions, valid groupings, and links for a desired network architecture, and calculates the data rate supported between users. These calculations are repeated until the end of the time series. Afterward, the key metrics, system capacity, system delay, and mass efficiency are output.

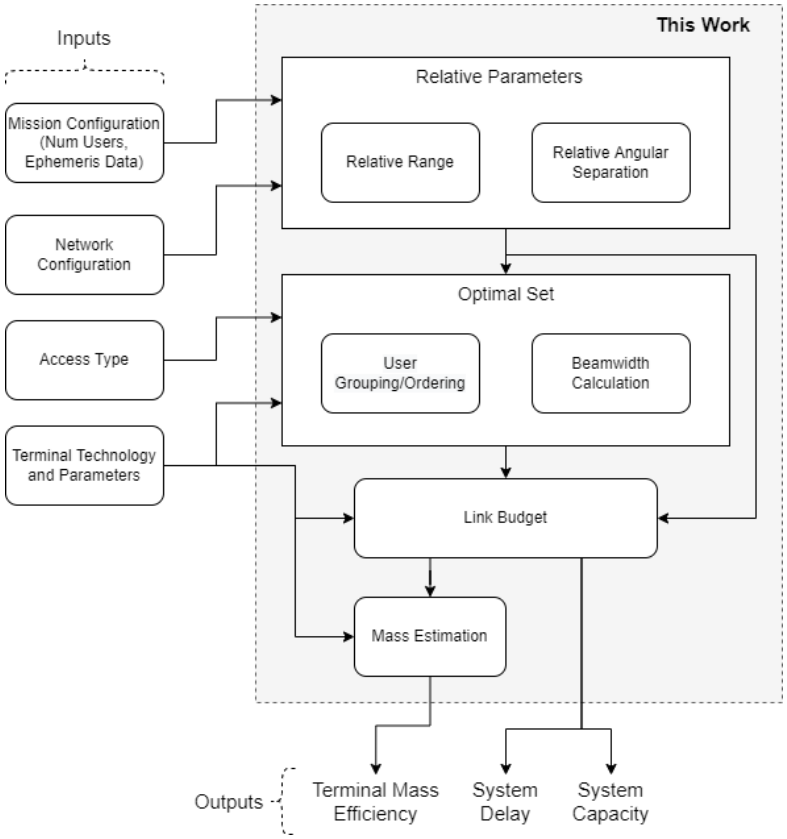

Figure 1: Functional diagram of model used to evaluate multiuser lasercom system performance. Inputs are the left and outputs, which are used as the key metrics, are pictured at the bottom.

2.1.1 Inputs

Four inputs are used to analyze a given mission: mission configuration, network configuration, access type, and terminal technology.

Mission configuration includes the number of users and the associated ephemeris data (position and velocity vectors as a function of time). This work looks at two different mission configurations: a LEO swarm mission and a deep-space mission, which were selected based on recent trends in lasercom missions and are discussed in detail in Chapter 4. Ephemeris data for the LEO mission is generated using STK, and the deep-space mission is from NASA JPL's Horizons System.

Network configuration defines the valid links within the simulation and can be selected as broadcast, relay, or multicast. In a broadcast configuration, only a single user can transmit to all other users. In a relay, all users can transmit but valid transmissions are restricted to specified

combinations e.g., user 2 can transmit to user 1 and 4 only. In a multicast configuration, links between all users are valid. Figure 2 illustrates the differences in connections between the three architectures.

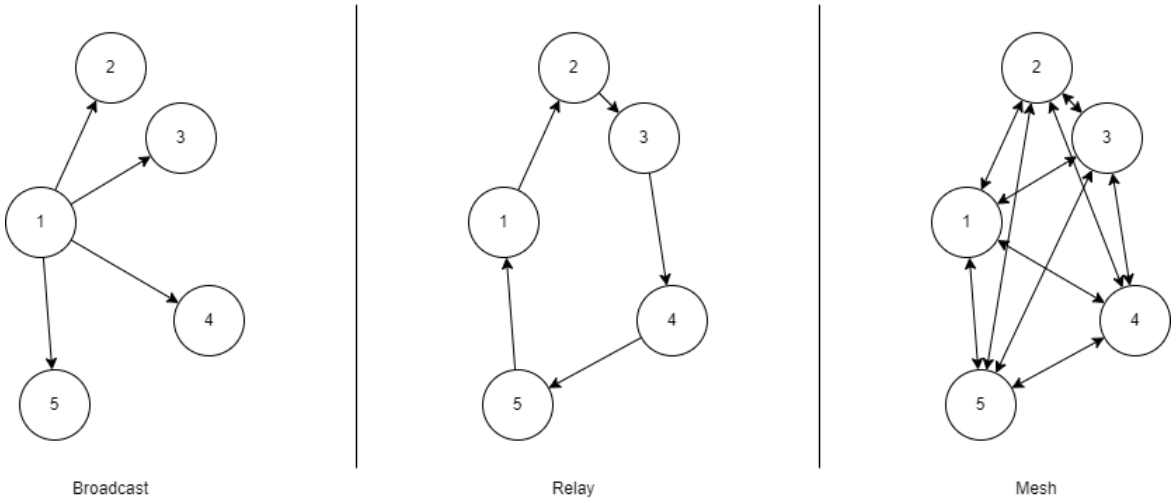

Figure 2: Different network architecture types. Broadcast systems assign a single user as the transmitter, and all other uses as the receivers. Relay systems form a ring joining all users together; only specific users may transmit/receive to/from other users. Multicast systems allow all users to transmit and receive from all other users.

Terminal technology is used to estimate the terminal mass and output power and has two selectable options. The first is a MOPA-transmitter architecture that uses a seed laser and fiber amplifier and serves as the standard approach to space-based lasercom transmitters. The second is a PIC-based transmitter architecture leveraging commercially-available photonics, which is novel for free-space lasercom transmitters. Terminal technology defines other relevant parameters for the link budget. Transmitter and receiver aperture size, modulation type and order, receiver detector type, terminal efficiency, and atmospheric conditions are all captured by this input.

Access type defines the type of medium access scheme to use for the analysis. As mentioned in Chapter 1, there are several access schemes to choose from. TDMA partitions the channel between all users in time. Each user sharing the channel is assigned a time slot during which they can transmit over the full channel bandwidth. TDMA allows each user to approach channel capacity when transmitting for a low number of users. Unfortunately, because users must wait for their timeslots to transmit data, channel utilization (bandwidth efficiency) is low and delay time is high

for bursty data. Additionally, all users must be synchronized with one another to know when to transmit. Only a single user may access the channel at once, which doesn't allow for multiple simultaneous link operation and creates communication breaks. This could lead to insufficient spatial sampling for the Pointing, Acquisition, and Timing (PAT) system and result in more link acquisitions which creates longer delays and exacerbates intermittent links.

CDMA assigns all users a unique signature that accomplishes two things: first, it spreads the data over a wider spectrum than it initially occupies, and secondly, it gives each user a unique, identifiable code. Characteristics of the signatures include low cross-correlation and high auto-correlation properties that allow all users to access the channel simultaneously. Optical CDMA was originally developed for terrestrial fiber systems [120], but the technique has been proposed for CubeSat constellations [87]. CDMA allows all users to fully utilize both time and wavelength spectrum and allows for network scaling. With CDMA, users can maintain multiple simultaneous links without duty cycling time, giving the system higher bandwidth efficiency compared with TDMA. In order to spread the data across a larger spectrum, the signature sequences are divided into smaller windows (chips) than the data itself and operate at much higher frequencies than the baud rate (see Figure 3).

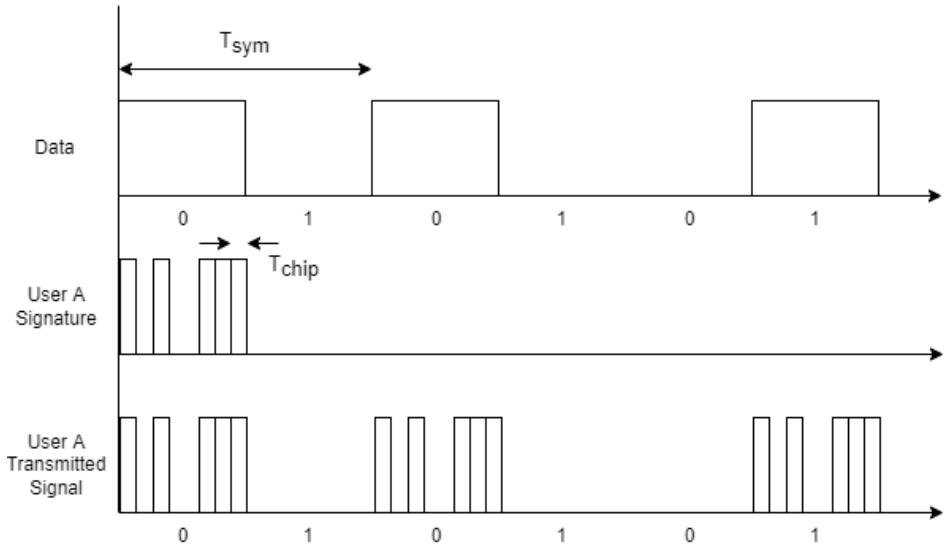

Figure 3: Example of a CDMA output signal. The top graph represents a binary PPM signal wherein an arbitrary waveform needs to be transmitted. The second graph gives an example of a user signature with smaller "chip" waveforms. The third row is the output signal masked with the signature code.

Strict synchronization is required to discern these signature sequences with similar issues to TDMA. Asynchronous CDMA may also be considered; however, the required signature lengths are longer and the SNR is lower [91].

SDMA divides users into unique locations such that a transmission received from a certain position identifies the user. This method allows users to fully utilize time and spectrum, but is fundamentally limited by the receiver FOV. Additionally, unless users are primarily stationary or can maintain their unique positions (e.g., geostationary satellites), users lose their unique spatial signature. Given the dynamics of the selected scenarios, SDMA is not considered in this analysis.

WDMA (FDMA) divides the bandwidth between all users in which each user transmits at a specified wavelength (or frequency) for the full transmission time. With narrow optical bandwidths, users can approach channel capacity and maintain multiple simultaneous links without the need for strict time synchronization. This method doesn't scale well with discrete optical elements as each wavelength requires a dedicated optical train. PICs are well suited to handle scaling a space-based optical network, but the Technology Readiness Level (TRL) for this approach is low and further analysis and testing are required to determine feasibility for space applications.

A stop-light chart is presented in Table 8. Each line item represents a desirable characteristic for the access method, and each column is an investigated access method. Green indicates the method has a desired characteristic, yellow shows that under certain conditions, the method has this characteristic but degrades with number of users, and red signals the method does not have this desired trait. The primary factor in selecting an access method is the capacity per user. CDMA and SDMA can support multiple simultaneous users, however, the capacity per user are not as competitive compared to TDMA and WDMA and are not considered further for analysis.

2.1.2 Performance Modeling

This work introduces and describes a novel approach to simulate the performance of a given system enabled by multiuser lasercom. Using a time-based simulation and fixed period (e.g., several orbits), instantaneous performance metrics can be determined and illustrates how the system changes through the period.

Table 8: Stoplight chart of different considered access methods.

Scheme	Wavelength Division		Optical Code Division	Time Division	Space Division
	Discrete	Photonics			
Capacity per user					
Frequency Utilization					
Time Utilization					
Simplicity					
Scalability					
TRL					
Multiple Simultaneous Links					

2.1.2.1 Relative Parameters

The relative parameters function takes ephemeris data from each user and creates a matrix of relative ranges and a matrix of angular separation between all users. For user 1, the range and angular separation to user 2 is calculated:

$$R_{1,2}(t) = \sqrt{\left(x_1(t) - x_2(t)\right)^2 + \left(y_1(t) - y_2(t)\right)^2 + \left(z_1(t) - z_2(t)\right)^2} \tag{7}$$

$$\theta_{1,2}(t) = \arctan\left(\frac{y_1(t) - y_2(t)}{x_1(t) - x_2(t)}\right) \tag{8}$$

$$\phi_{1,2}(t) = \arccos\left(\frac{z_1(t) - z_2(t)}{R_{1,2}(t)}\right) \tag{9}$$

The output matrices are structured as:

$$R_{all}(t) = \begin{bmatrix} R_{1,2}(t_0) & R_{1,3}(t_0) & \dots & R_{1,k}(t_0) & R_{2,1}(t_0) & \dots & R_{k,k-1}(t_0) \\ R_{1,2}(t_1) & R_{1,3}(t_1) & \dots & R_{1,k}(t_1) & R_{2,1}(t_1) & \dots & R_{k,k-1}(t_1) \\ & & & \ddots & & & \\ R_{1,2}(t_n) & R_{1,3}(t_n) & \dots & R_{1,k}(t_n) & R_{2,1}(t_n) & \dots & R_{k,k-1}(t_n) \end{bmatrix} \tag{10}$$

$$\theta_{all}(t) = \begin{bmatrix} \theta_{1,2}(t_0) & \theta_{1,3}(t_0) & \dots & \theta_{1,k}(t_0) & \theta_{2,1}(t_0) & \dots & \theta_{k,k-1}(t_0) \\ \theta_{1,2}(t_1) & \theta_{1,3}(t_1) & \dots & \theta_{1,k}(t_1) & \theta_{2,1}(t_1) & \dots & \theta_{k,k-1}(t_1) \\ & & & \ddots & & & \\ \theta_{1,2}(t_n) & \theta_{1,3}(t_n) & \dots & \theta_{1,k}(t_n) & \theta_{2,1}(t_n) & \dots & \theta_{k,k-1}(t_n) \end{bmatrix} \tag{11}$$

$$\phi_{all}(t) = \begin{bmatrix} \phi_{1,2}(t_0) & \phi_{1,3}(t_0) & \dots & \phi_{1,k}(t_0) & \phi_{2,1}(t_0) & \dots & \phi_{k,k-1}(t_0) \\ \phi_{1,2}(t_1) & \phi_{1,3}(t_1) & \dots & \phi_{1,k}(t_1) & \phi_{2,1}(t_1) & \dots & \phi_{k,k-1}(t_1) \\ & & & \ddots & & & \\ \phi_{1,2}(t_n) & \phi_{1,3}(t_n) & \dots & \phi_{1,k}(t_n) & \phi_{2,1}(t_n) & \dots & \phi_{k,k-1}(t_n) \end{bmatrix} \tag{12}$$

Where n is the number of time steps, k is the number of users, $R_{all}(t)$ is in units of meter, and $\theta_{all}(t)$ and $\phi_{all}(t)$ are in units of radians. Each user represents k columns, and the full matrix size is (n-1) x (k x (k-1)).

2.1.2.2 Optimal Sets

The optimal set function takes the relative variables and determines user groupings as well as beamwidth sizes. Before transmission, each transmitter seeks to minimize the number of acquisitions and transmissions by grouping receiver nodes into sets. The optimal set grouping starts with a given transmitting user at time t.

It is assumed each transmitter has coarse position knowledge of each receiver. Coarse position is assumed to be derived from ephemeris position knowledge transmitted either by the ground or via RF crosslink from other nodes, with an accuracy of +/- 3 m, which is standard for GPS-based position knowledge.

A single transmission group (set) starts with a single receiving user and the beamwidth set to a maximum divergence, which is dependent on the mission configuration (see Chapter 4). The transmitter then sweeps the beam in a clockwise direction and looks for other users that may be adjacent to the current receiving user.

If two users or more users are within the beamwidth of the transmitting user, it is assumed they all simultaneously establish a link with the transmitting user, the other users are added to the current set, and the beamwidth for that set is equal to the maximum divergence. Otherwise, the set is comprised of a single receiving user, the transmitting user moves on to the next set and receiving user, and the beamwidth is equal to the minimum divergence. Figure 4 illustrates optimal set groupings.

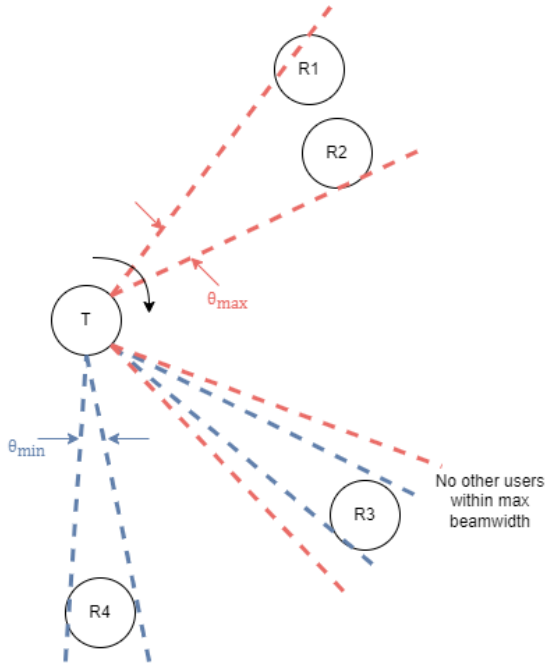

Figure 4: Example of optimal set groupings. In order to reduce retransmission of data, receiving users are grouped together in a set if within the transmitters FOV.

The set formation algorithm is structured as:

$S_j = \{R_i\}$
for $i = 1{:}\,k-1$
    if $\left(\theta_{T,R_{i+1}}(t) - \theta_{T,R_i}(t)\right) < \theta_{max}$ AND $\left(\phi_{T,R_{i+1}}(t) - \phi_{T,R_i}(t)\right) < \theta_{max}$
        $S_j = \{R_i, R_{i+1}\}$
        $\theta_{div}(t) = \theta_{max}$
    else
        $j = j + 1$
        $S_j = \{R_{i+1}\}$
        $\theta_{div}(t) = \theta_{min}$
    end
end

Where T denotes the transmitting user, R_x denotes the receiving users (not the same as range R in Eq. (7)), $\theta_x(t)$ and $\varphi_x(t)$ are values from the relative parameters $\theta_{all}(t)$ and $\varphi_{all}(t)$ matrices, and $\theta_{div}(t)$ is the beam divergence in units of radians.

This is based on the work done by [118], however, instead of an explicit time-based optimization, this work uses spatial groupings as a proxy to reduce the number of re-transmissions, and therefore time. A comparison of the two approaches is presented in Chapter 3.

2.1.2.3 Link Modeling

The link budget calculates the maximum supported data rate for each link between users as well as the individual delay components for time *t*. The Friis transmission equation is used to determine the power received [121]

$$P_{rx} = \frac{P_{tx} G_{tx} G_{rx} \eta_{tx} \eta_{rx}}{L_{fs} L_{atm} L_{point}} \tag{13}$$

$$G_{tx} = \frac{4\pi}{\Omega} \tag{14}$$

$$\Omega = 2\pi \left(1 - \cos\left(\frac{\theta_{div}(t)}{2}\right)\right) \tag{15}$$

$$G_{rx} = \left(\frac{\pi D_{rx}}{\lambda}\right)^2 \tag{16}$$

$$L_{fs} = \left(\frac{\lambda}{4\pi R(t)}\right)^2 \tag{17}$$

Where P_{tx} is the output power at the transmitter in Watts, G_{tx} is the transmitter gain which is unitless in linear scale, G_{rx} is the receiver gain which is also unitless, η_{tx} and η_{rx} are the transmitter and receiver efficiencies (unitless), L_{fs} is the free-space path loss (unitless in linear scale), L_{atm} is the atmospheric loss (unitless), L_{point} is the pointing loss (unitless), Ω is the beam solid angle in steradians, D_{rx} is the receiver aperture diameter in meters, and λ is the wavelength in meters. Values for each parameter are given for each analysis in Chapter 4.

Atmospheric attenuation caused by absorption and scattering from atmospheric constituents reduces the overall received power. Water vapor (H_2O), oxygen (0_2), and carbon

dioxide (CO_2) are the dominant species responsible for attenuating signal in the IR spectrum [122]. Specifically, water vapor absorption is the dominant mechanism of attenuation in the IR. The total attenuation is dependent on path length and can be scaled by the telescope viewing angle (zenith angle). Transmission through the atmosphere is typically referenced to 0° zenith angle (ZA) and decreases as the local ground station ZA increases. Biswas [123] has shown this relationship can be represented as

$$L_{atm} = T_0^{\sec(ZA)} \tag{18}$$

Where T_0 is the wavelength-dependent transmittance at 0° ZA and accounts for the additional path length through the atmosphere.

In addition to attenuation, atmospheric turbulence changes the beam wavefront as it propagates through the atmosphere and changes the irradiance pattern at the receive aperture. To quantify the limitations imposed by atmospheric turbulence as it applies to lasercom, this work first looks at the optical system resolution limits.

In ideal conditions, an optical system with a circular aperture can resolve feature sizes given by the width of a point-spread function known as an Airy disk. The system is said to be diffraction-limited when the Airy disk width is given by the Rayleigh criterion:

$$\theta = 1.22\frac{\lambda}{D} \tag{19}$$

Where θ is the angular resolution of the system in radians, λ is the wavelength in meters, and D is the receiver aperture diameter in meters. In other words, an optical system cannot resolve features smaller than the Rayleigh criterion.

Under turbulent atmosphere conditions, resolution is limited by the Fried parameter defined by [124]:

$$r_0 = \left[0.42\, k^2 \int_0^L C_n^2(z) dz\right]^{-\frac{3}{5}} \tag{20}$$

$$k = \frac{2\pi}{\lambda} \tag{21}$$

Where k is the wavenumber in m^{-1}, C_n^2 is the refractive-index structure with units $m^{-2/3}$, and z is the path length in meters.

Also known as the atmospheric coherence length, r_0 is a mathematical description of the performance of an optical system while operating in turbulent atmosphere. Large r_0 values correspond to "good" seeing conditions (minimal atmospheric disturbances) and small r_0 values are considered "bad" seeing conditions (more disturbances). The resolution ratio introduced by [125] describes the relationship between resolution and D/r_0:

$$\eta_R = \frac{R}{R_{max}} \cong \frac{\left(\frac{D}{r_0}\right)^2}{\left[1 + \left(\frac{D}{r_0}\right)^{\frac{5}{3}}\right]^{\frac{6}{5}}} \tag{22}$$

When r0 << D, the system is not operating at the "limiting resolution" described by R_{max}, and instead at a percentage $1/\eta_R$ of the achievable limit. Figure 5 illustrates this ratio.

In lasercom systems, lower resolution effectively reduces the receiver aperture size. As described in [123], r_0 can also be thought of as increasing the size of the beam image in the receiver focal plane, which is also analogous to a reduced aperture size. This work accounts for the change in effective aperture size by scaling the receiver diameter using Eq. 24 for given atmospheric conditions. Under poor atmospheric conditions, D_{scaled} is reduced to a percentage of the physical receiver size to give an effective lower collection area.

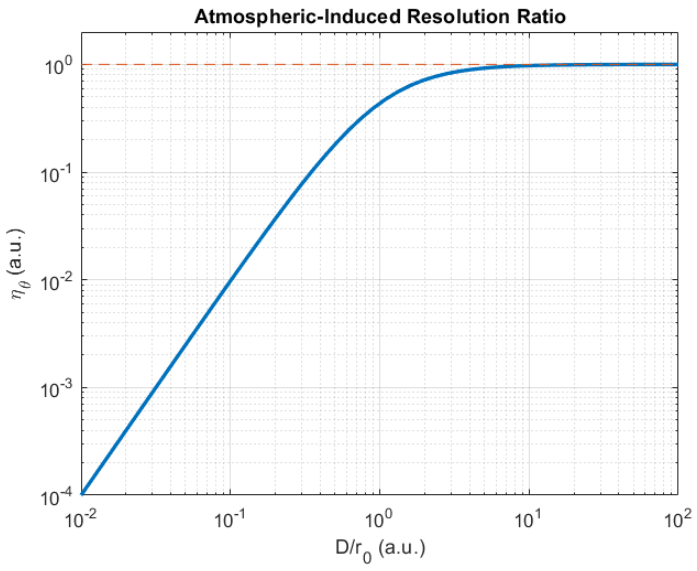

Figure 5: Resolution ratio. As atmospheric turbulence increases, the resolution at the focal plane decreases as a function of physical aperture size and atmospheric seeing conditions.

$$D_{scaled} = \eta_R \, D_{rx} \tag{23}$$

$$D_{scaled} = \frac{\frac{D_{rx}^3}{r_0^2}}{\left[1 + \left(\frac{D_{rx}}{r_0}\right)^{\frac{5}{3}}\right]^{\frac{6}{5}}} \tag{24}$$

After the link parameters and received power are calculated, the maximum supported data rate, or capacity, of the single point-to-point links is calculated. This analysis assumes a Pulse Position Modulation (PPM) for the deep-space case as it has been used and proposed for a range of missions from lunar and deep space [13], [41], [66], [126].

Moision et. al have shown the capacity of a deep-space (photon-starved) PPM link can be approximated by [127]:

$$C_{i,k,PPM}(t) = \frac{1}{\ln(2)\, E_\lambda} \frac{P_i^2}{P_i \frac{1}{PPM} + P_n \frac{2}{PPM - 1} + P_i^2 \frac{PPM\, T_s}{\log(PPM)\, E_\lambda}} \tag{25}$$

Where E_λ is the wavelength-dependent photon energy in Joules, P_i is the received power required to close the link in Watts, *PPM* is the modulation order (ranging from 2 to 128), P_n is the noise power in Watts, and T_s is the slotwidth of the PPM signal in seconds. The denominator values are separated into three additive noise components; From left to right, the first component represents the quantum limit, the second the background noise limit, and the third is the bandwidth limit. The units of capacity are given in bits/sec.

Q-factor analysis is used to determine the required power at the receiver [1], [23], [99], [128]. This accounts for the noise present in the receiver and is specific to each scenario. While the deep-space optical channel has been shown to be a Poisson process, exact numerical and analytical solutions yield small deviations from the Gaussian process representation [1] and Gaussian is used in this work to calculate receiver sensitivity.

$$BER \cong Q\{SNR\} \tag{26}$$

$$SNR = \frac{\mu_1 - \mu_0}{\sqrt{\sigma_0^2 + \sigma_1^2}} \tag{27}$$

$$\mu_0 = RM\left(P_{bkg} + P_{rx}ER_0\right) \tag{28}$$

$$\mu_1 = RM\left(P_{bkg} + P_{rx}ER_1\right) \tag{29}$$

$$\sigma_{shot,0}^2 = 2qBW_eF\left(RM^2\left(P_{bkg} + P_{rx}ER_0\right) + i_{dark}\right) \tag{30}$$

$$\sigma_{shot,1}^2 = 2qBW_eF\left(RM^2\left(P_{bkg} + P_{rx}ER_1\right) + i_{dark}\right) \tag{31}$$

$$\sigma_{therm}^2 = \frac{4kT_{rx}BW_e}{R_L} \tag{32}$$

$$\sigma_0^2 = \sigma_{shot,0}^2 + \sigma_{therm}^2 \tag{33}$$

$$\sigma_1^2 = \sigma_{shot,1}^2 + \sigma_{therm}^2 \tag{34}$$

Where μ_0 and μ_1 is the mean signal power received during a symbol transmission of a 0 or 1, respectively, in amps. This analysis refers the signal to the input of the demodulation and decoding electronics at the receiver and is in units of amps. The variables σ_0^2 and σ_1^2 are the signal variances which capture the noise present in the receiver and are reported in units of amps^2. Noise power is comprised of two values: shot and thermal noise; the former is typically the dominant factor in

optical systems while the latter is dominant in RF systems. R is the sensor responsivity typically reported in units of amps/Watt and is related to the quantum efficiency of the detector. M is the detector gain which is unitless. P_{bkg} and P_{rx} are the background and received powers, respectively, in Watts. ER_0 and ER_1 are scaling factors that account for the transmitter's finite extinction ratio. The constant q is the elementary charge constant in Coulombs. BW_e is the noise-equivalent bandwidth of the receiver in Hertz. F is the excess noise factor which is typically > 1 in APDs and equal to 1 otherwise. The dark current, i_{dark}, is a measured characteristic of the detector in units of amps. K is Boltzmann's constant in units of Joules per Kelvin. T_{rx} is the effective receiver temperature in Kelvin. R_L is the load resistance typically matched to 50Ω, but may be higher depending on the application. It can be advantageous to increase the load resistance as it reduces the thermal noise, however, this is traded with receiver speed which is proportional to $1/R_L$.

After the point-to-point capacity is determined, delay is calculated:

$$d_k(t) = d_{prop}(t) + d_{align} + d_{Tx}(t) + d_{access} \tag{35}$$

$$d_{prop}(t) = \frac{R_{i,k}(t)}{c} \tag{36}$$

$$d_{Tx}(t) = \frac{G}{C_{i,k}(t)} \tag{37}$$

Where d_k is the total delay in seconds, d_{prop} is the propagation delay of the signal through space in seconds, d_{align} is the alignment delay in seconds, d_{access} is the delay associated with the selected access method in seconds, $R_{i,k}(t)$ is the relative range in meters between users i and k at time t, c is the speed of light in meters per second, G is the total data volume in bits to transmit, and $C_{i,k}(t)$ is the capacity between users i and k at time t in bits per second. Propagation delay is the physical time it takes for a signal to traverse the link range. Alignment delay is held as a constant 3 seconds and represents the time it takes to accurately point and establish a link between users. Transmit delay is the time it takes to send a data payload of volume G using data rate $C_{i,k}(t)$. This works assumes G is a fixed value of 50 MB, which is about the size of a data payload from a hyperspectral Synthetic Aperture Radar (SAR) node [129] or a few hyperspectral images [130]. Access delay is assigned a value only for TDMA analysis and describes how long it takes for all users to transmit *i.e.*, how long other users must wait before transmitting their own data.

2.1.2.4 Mass Estimate

After the link budget calculation, the terminal mass is estimated based on the selected terminal technology. Mass estimates can provide a quantitative system-level metric for a lasercom terminal. Mass comparisons and mass normalized by the data rate can highlight the differences between current state-of-the-art terminals and next-generation terminals leveraging technology such as PICs. Here, we define this as the mass efficiency metric:

$$\eta_M = \frac{\mu_C}{M_{terminal}} \tag{38}$$

Where $M_{terminal}$ is the estimated mass in kg, and μ_C is the mean transmitting user link capacity in bits per second.

The terminal mass is estimated based on the input technology. For a traditional, current-state-of-the-art input, such as a MOPA transmitter using a fiber amplifier, the mass is estimated as:

$$M_{terminal} = M_{aperture} + M_{amplifier} \tag{39}$$

$$M_{aperture} = D_{Tx}^{2.57} K \tag{40}$$

$$M_{amplifier} = 1.152 P_{out} + 1 \tag{41}$$

Where K is a fit value equal to 0.00181, D_{Tx} is the transmitter aperture diameter in meters, and P_{out} is the output power in Watts. This approximation was adopted from [131], which set the mass of the DSOC predecessor, Deep space Optical Terminal (DOT). Here, it has been modified to extend to Cubesat-class spacecraft based on recent developments of miniaturized terminals that were not accounted for in [131].

For PICs, a similar approach is applied, however, the PIC mass with supporting electronics is approximated instead of an amplifier. Little data is available on the exact mass specifications of PICs, especially in a transceiver configuration as most end-users (such as datacenters and ground-based telecommunication customers) are not mass constrained.

This analysis uses the density of commonly used semiconductor materials (primarily III-IV semiconductor materials) to approximate the mass of a PIC-based terminal. A single photonic

transmitter or receiver footprint can vary widely, but recently literature shows single devices range from ~4 mm – 9 mm x ~1 mm – 3 mm x ~0.4 mm – 0.5 mm [132]. Here, an average volume of 6.5 x 2 x 0.45 mm^3 is assumed. Commonly used materials include Indium Phosphide (InP), Silicon (Si), Lithium Niobate (LiNbO3), and Gallium Arsenide (GaAs), among others. Table 9 lists the densities for each.

Table 9: Common PIC materials with corresponding densities and approximate chip mass based on a 6.5 x 2 x 0.45 mm^3 device

Material	Density (g/cm^3)	Approximate Chip Mass (g)
InP	4.81	0.0281
Si	2.33	0.0136
GaAs	5.32	0.0311
LiNbO3	4.65	0.0272

This approach assumes a uniform material and continuous structure within the volume, both of which are untrue in PIC fabrication. Multiple materials and structures are used to propagate light within the chip, however, without insight into exact quantities and geometries, an accurate mass estimate is difficult to approximate. The mass of supporting electrical components and packaging is also challenging to estimate due to lack of publicly available information and low Technology Readiness Level (TRL).

Telecom transceivers are used as a proxy for a complete integrated system include the chip, electronics, packaging and other considerations such as temperature control and channel isolation [71]. Example characteristics are shown in Table 10. Compared to the approximated InP chip mass in Table 8, the total mass is ~4000X greater and likely dominated by the packaging and electronics.

Telecommunication PICs are specialized for low-power, high-speed, coherent modulation, while free-space lasercom requires high peak-power, coherent or direct-detect modulation. A few PICs have been designed for free-space-like applications and are summarized in

Table 11. Based on the size of the devices and known packaging and electronics multiplier, the estimated terminal mass is calculated.

Table 10: Cisco plug-and-play 400G optical modules for terrestrial optical communication applications. Key specifications are listed with an emphasis on advertised mass.

Module	Mass (g)	Average Transmit Power per Channel (mW)	Wavelength (nm)	Num Channels
QDD-400G-DR4-S	100	2.51	1310	4
QDD-4X100G-LR-S	100	3.02	1310	4
QDD-400G-FR4-S	100	2.24	1270 - 1330	4

Table 11: Existing PICs that have been proposed or have applications to free-space lasercom.

Name	Wavelength (nm)	Max Output Power (mW)	Extinction Ratio (dB)	Size (mm^2)	Primary Material	Estimated Chip Mass (g)	Estimated Terminal Mass (g)
Deep Space PIC [133]	1527	~35	28	6 x 0.5	InP	0.007	28.86
Multi-Modulation PIC [134]	~1530 - 1560	7.5	25	Not Given	InP	-	-
Wideband PIC [107]	~1525 - 1565	18	13	5.5 x 0.36	InP	0.005	19.05
High Power Transmitter [108]	1556	79.4	5.8	3.5 x 0.36	InP	0.003	12.12
Local Oscillator [135]	1543	100	-	4.3 x 0.54	InP	0.006	22.34
QUAD Transmitter [136]	~1520 - 1570	~11	25	~3.5 x 0.5	InP	0.004	16.84
TunIT [137]	~1535-1595	2.5	-	~3.5 x 0.5	InP	0.004	16.84

The relationship between mass and PIC output power can be determined from the available high output power PICs and their estimated mass. First, we consider applying a linear fit.

$$M_{terminal} = M_{aperture} + M_{PIC} \tag{42}$$

$$M_{PIC} = \alpha P_{out} + \beta \tag{43}$$

$$\alpha = 2.6x10^{-3} \tag{44}$$

$$\beta = 19.2351 \tag{45}$$

Where α and β are linear coefficients.

Figure 6 shows the linear fit applied to the existing data. Outliers such as the High-Power PIC, which produces considerable output power compared to devices of the same size, and Deep Space PIC, which outputs relatively low power for its size, skew the fit. The maximum difference error for the fit vs actual data is -9.5 g (under estimating) seen in the Deep Space PIC. Additional data is needed to develop a higher fidelity estimate, however, for this analysis the approximation is considered sufficient as the error is on the order of grams, whereas payload masses are on the order of kilograms.

2.1.3 Outputs

The key metrics for this analysis are the three outputs: system capacity, system delay, and mass efficiency. System capacity is the sum of all the data rates for a given time *t*. At the end of the simulation, the maximum data rate the system supported at any given time is shown. System delay is the sum of all delay components for a given user *k* across all time. This metric is meant to illustrate how much time each user spends on each task (e.g., transmitting, waiting, aligning, etc.). Mass efficiency is a two-step calculation: the average capacity of each user over all time is first calculated, then divided by the estimated terminal mass for a given technology. This metric is meant to capture the system-level performance of a terminal. For example, PICs have a lower output power compared to their EDFA counterparts and may result in lower data rates for a given mission configuration. The mass efficiency for a PIC system, however, may be higher than that of an EDFA terminal which further motivates increasing the TRL for PIC-based transmitters for some application instances. Results for the model are shown in Chapter 4.

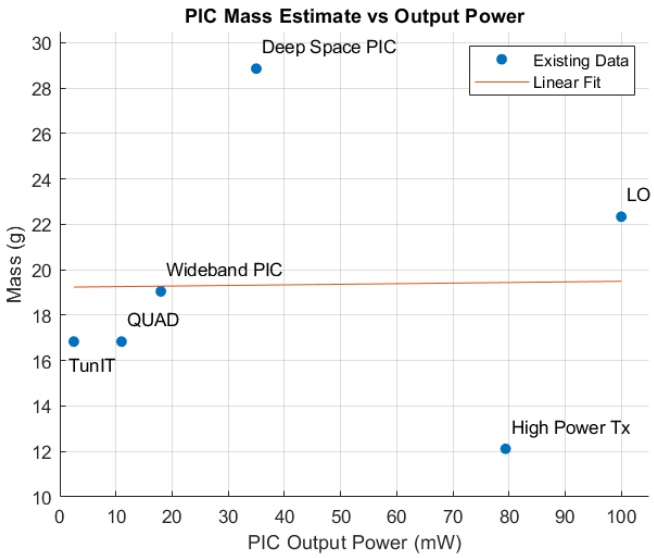

Figure 6: Plot of existing transmitter PICs' mass vs output power. A linear fit is applied and displayed again the existing data.

Chapter 3

System Verification

Verification is separated into two sections. First, a high-fidelity link budget is presented and compared with existing DSOC performance results [66]–[68], [138], [139]. Nominal and worst-case deterministic link budgets including atmospheric turbulence are presented and compared to the existing DSOC performance predictions. Secondly, a protocol performance verification is presented using an optical-based 5G backhaul application [118].

3.1 DSOC Overview

DSOC is a technology demonstration payload onboard the Discovery-class mission PSYCHE which is scheduled to launch in August 2022 [66], [140]. PSYCHE's final destination is a metalloid asteroid between Mars and Jupiter known as Psyche-16 thought to be the remnants of a planetary core. During transit, the Psyche spacecraft will point the DSOC terminal toward Earth to demonstrate the longest-range optical downlink to date. Data rates ranging from 0.2 – 200+ Mbps are planned over link ranges spanning 0.2 to 2.7 AU [66].

The DSOC Concept of Operations (CONOPS) is:

- A 5-kW, 1064-nm laser beacon located at Table Mountain Facility near Wrightwood, California, points toward Psyche. The beacon signal is received on DSOC's photon-counting camera and used for precision pointing toward Earth.
- Once DSOC is pointed accurately toward Earth, the 4-W, 1550-nm flight laser on Psyche initiates the downlink.
- The downlink signal is received at the 5-m Hale telescope located at the Palomar Observatory near San Diego, California. The signal is focused and directed toward a Superconducting Nanowire Single Photon Detector (SNSPD) receiver.

3.1.1 Ground Beacon

The uplink beacon is hosted at JPL's Optical Communications Telescope Laboratory (OCTL) and uses a 1-m primary aperture for transmission. The 5-kW output power is achieved by spatial power combining multiple lasers in free-space. Each laser is slightly offset in wavelength to avoid interference. Wavelength diversity is also desirable to mitigate atmospheric effects and maintain a constant average power at the spacecraft. The beacon has two divergence settings used for different acquisition phases. A 100-urad divergence is used for coarse acquisition, then 40-urad is used for precision acquisition or when higher SNR is required at the spacecraft. Low data rates up to 1.6 kbps using PPM-2 are supported [66].

3.1.2 Flight Terminal

The laser assembly was built and delivered by Fibertek and houses a 1550nm, 4-W, MOPA laser using an average-power limited EDFA. Originally, the average power requirement for the flight terminal was set to 10 W but was descoped due to reliability issues in the fiber-coupled output[1]. The laser has a measured extinction ratio of > 33 dB, which exhibits high peak power levels for higher-order PPM. The EDFA is built with a two-stage amplifier and radiation tolerant Er- and Er/Yb-doped fibers. The terminal has a ~10% wall-plug efficiency and requires ~100 W during downlink operations. This is comparable to the Mars Reconnaissance Orbiter (MRO) Ka-band downlink terminal, which requires ~110 W for a 1.8 Mbps downlink [141]. The primary aperture is 22 cm and the downlink beam has a 14-urad full angle $1/e^2$ divergence (7-8-urad half angle), which is limited by the pointing mechanism (vs. limited by the diffraction limit).

The Point Ahead Mirror (PAM) was built and delivered by CTEC/L3-Harris and compensates for the relative velocities between bodies (*i.e.*, the position of Earth at the start of the downlink is different than the position of Earth when the downlink signal traverses the separation range; the PAM assembly directs the beam to the estimated position of Earth after the signal has propagated over the link range). At DSOC's maximum separation (~2.6 AU), the downlink spot size is expected to be ~2722.7 km in radius, which is about 43% of the Earth's radius. The PAM has a +/- 2.5 urad pointing error corresponding to a maximum of 1.18 dB pointing loss. The beam divergence

[1] C., Asbury, personal communications, March 2021

is oversized to compensate for the pointing loss such that 76% of the transmitted power will reach the ground receiver in a worst-case pointing scenario [67], [131], [142].

The Photon Counting Camera (PCC) was designed and built by MIT Lincoln Laboratory to acquire the uplink beacon from Earth. The PCC uses a 32 x 32 array of InGaAsP Avalanche Photodiodes (APDs) operating in Geiger mode to detect faint signal photons from Earth. It also simultaneously images the downlink beam to provide pointing feedback for the PAM assembly [143].

3.1.3 Ground Receiver

The ground receiver is hosted at the Hale telescope within the Palomar observatory complex. The primary aperture is a 5-m telescope retrofitted with the receiver optics and electronics. The receiver detector is a Tungsten Silicide (WSi) Superconducting Nanowire Single Photon Detector (SNSPD) capable of detecting faint signal photons at 1550 nm. The detector is segmented into four quadrants for position tracking and has a total active area of 79,000 um^2. To mitigate thermal noise as much as possible, the detector is cryogenically cooled to 1K, and the preceding lens and filters are cooled to 4 K and 40 K, respectively. Blackbody background radiation from thermal effects still dominate the noise counts with ~10,000 counts per second (cps) registered across the full array area. The detector converts ~70% of photons into counts under nominal operating conditions but have shown higher efficiency with larger bias current and voltage [144]–[147].

The SNSPD detection mechanism is fundamentally different than traditional photodetection. Instead of generating an electron-hole pair, an incident photon induces a spatial change to current flowing through the nanowire. The directional change pushes the current to the readout electronics, which register a voltage spike. Alternatively, the incident photon creates a localized area of high resistance which causes a re-direction of nanowire current to the readout electronics. The subsequent voltage spike is then amplified and time-tagged using a Time-to-Digital Converter (TDC) which is interpreted and demodulated by an FPGA. After photon detection, the current within the nanowire requires some time to resume nominal flow. This is known as dead time and any photons incident during nanowire deadtime will not be registered. Ground receiver SNSPDs have a dead time of 28 ns [144]–[147].

The optical communication standards released by the CCSDS specify deep-space optical communication modulation parameters, specifically, high-photon efficiency signaling methods (e.g.,

PPM) must support modulation orders of M = [16, 32, 64, 128] and selectable slot widths of T_s = [0.5, 1, 2, 4, 8] nanoseconds. These requirements restrict the minimum timing resolution (maximum error) at the receiver. For the SNSPD receiver, the measured timing jitter is ~120 ps, with roughly half of that attributed to the TDC.

3.1.4 Atmosphere

Hale telescope is positioned at 1.7 km above sea level. Though the local site has not been recently characterized for atmospheric propagation and transmission properties, the beacon site at Table Mountain Facility has been extensively characterized [123]. These sites are not co-located but are separated by ~195 km. Downlinks performed after the spacecraft passes a range of 0.2 AU will illuminate both sites simultaneously. While the atmospheric channels above each ground station aren't identical, they will be occupied simultaneously for the majority of the planned downlinks over the mission and can be considered similar enough for atmospheric analysis.

Atmospheric characteristics at Table Mountain Facility have been rigorously simulated and measured by Biswas et. al [123]. Using MODTRAN, sky irradiance models were developed across a 500-2000 nm spectrum for different viewing and atmospheric conditions. For these models, it is assumed the Sun Zenith Angle (ZA) is 45° and the telescope ZA varies between 10°, 40°, and 70° (-35°, 5°, and 25° relative to the sun). The relative azimuth angle between the sun and telescope is set to 0°. It is assumed the aerosol boundary layer starts at 1 km above sea level, and the aerosol concentration is varied to produce 5-km visibility (high concentration) and 23-km visibility (low concentration). Note that the 40° ZA case produces the largest sky irradiance values due to the low sun separation angle [123].

This analysis uses the 70° ZA, 2-km altitude, 5-km visibility case at 1550 nm ([123] page 160) as a representative daytime sky irradiance. Other point sources, such as star irradiance or planetary irradiance, are not used for daytime observations as they are orders of magnitude lower than Sun irradiance [123]. For the nighttime case, it is assumed the brightest object in the receiver FOV is Mars.

Fried parameter, r0, statistics for TMF are also given in [123] for 1064 nm. Measurements at 2 km above sea level show r0 ranging from 10-30 cm, with a worst-case simulated values down to 3.6 cm for large ZA [123]. This analysis assumes r0 worst-case is 3 cm, and nominal is 5 cm [142].

3.1.5 Link Verification Results

Existing models from early systems engineering studies and more recent DSOC results were used to verify the results of this work. First, the early DSOC systems engineering terminal named Deep space Optical Terminal (DOT) is discussed, and a link budget is used to compare the results of this work and the DOT results. Newer results from recent DSOC design and implementation are then used for capacity vs. range comparisons.

Initially, the DSOC ground receiver was baselined as the Large Binocular Telescope (LBT) in Mount Graham, Arizona. The effective receiver aperture size using dual 8.4-m apertures is 11.8 m. Using parameters outlined in [131] and the provided link budget, nominal and worst-case day and nighttime links were compared. Note the LBT DOT analysis excludes several of the parameters discussed in previous sections within this chapter, including the receiver dark count rate and efficiency, as well as the transmitter finite extinction ratio. It is assumed the dark current and extinction ratio are 0, and the assumed receiver efficiency is given by [131]. Table 12 summarizes the model results and [131] results. Link analysis and capacity estimation is performed using the approach presented in Chapter 2.

Table 12: Link Budget Comparison Between the Performance Predicted by This Work and Existing Data for the Deep-space Optical Terminal (DOT), the Precursor to DSOC [131].

	Daytime				Nighttime				
System	**This Model Nominal**	**This Model Worst Case**	**DOT Nominal**	**DOT Worst Case**	**This Model Nominal**	**This Model Worst Case**	**DOT Nominal**	**DOT Worst Case**	**Units**
System Parameters									
BER	1.00E-06	1.00E-06	1.00E-06	1.00E-06	1.00E-06	1.00E-06	1.00E-06	1.00E-06	-
PPM	16.00	16.00	16.00	16.00	16.00	16.00	16.00	16.00	-
Pointing Loss	-1.17	-1.17	0.00	0.00	-1.17	-1.17	0.00	0.00	dB
Tx Parameters									
Output Power	6.02	6.02	6.02	6.02	6.02	6.02	6.02	6.02	dBW
$1/e^2$ Beamwidth	8.00	8.00	7.00	7.00	7.00	7.00	7.00	7.00	urad
Transmitter Gain	113.98	113.98	113.98	113.98	113.98	113.98	113.98	113.98	dBi
Transmitter Loss	-5.47	-5.88	-5.47	-5.88	-5.47	-5.88	-5.47	-5.88	dB
Channel Parameters									
Range	0.42	0.42	0.42	0.42	0.42	0.42	0.42	0.42	AU
Free Space Path Loss	-354.14	-354.14	-354.14	-354.14	-354.14	-354.14	-354.14	-354.14	dB
Zenith Angle	40.00	70.00	40.00	70.00	60.00	70.00	60.00	70.00	deg
Atm. Transmission Loss	-0.26	-0.92	-0.26	-0.91	-0.26	-0.92	-0.26	-0.91	dB
r0	5.00	3.00	5.00	3.00	15.40	7.90	15.40	7.90	cm
Rx Parameters									
Aperture Diameter	11.80	11.80	11.80	11.80	11.80	11.80	11.80	11.80	m
Receiver Gain	147.57	147.57	147.57	147.57	147.57	147.57	147.57	147.57	dBi
Receiver Losses	-5.27	-6.07	-5.27	-6.07	-5.27	-6.07	-5.27	-6.07	dBi

Background Radiance	1.90E-03	8.50E-03	1.90E-03	8.50E-03	8.90E-04	8.90E-04	8.90E-04	8.90E-04	W/cm^2/sr/mm
Background Flux	1.08E+07	4.84E+07	1.21E+07	4.15E+07	5.07E+06	5.08E+06	4.31E+06	4.31E+06	ph/s
Signal Flux	2.59E+08	1.65E+08	1.22E+08	1.42E+08	2.18E+08	1.65E+08	1.22E+08	1.42E+08	ph/s
Power Required	4.40E-12	3.58E-12	6.23E-12	1.15E-11	4.05E-12	3.53E-12	2.21E-12	1.10E-12	W
Power Received	3.32E-11	2.11E-11	1.56E-11	1.82E-11	2.80E-11	2.11E-11	1.56E-11	1.82E-11	W
Margin	8.78E+00	7.70E+00	4.00E+00	2.00E+00	8.40E+00	7.77E+00	8.50E+00	1.22E+01	dB
Margin Error Ratio	-	-	2.19	3.85			0.99	0.64	-

The final metric used to measure the difference between the two analyses are given in the last row as the "margin error ratio", which evaluates the ratio between the modeled link budget margin and the existing analysis margins from [131]. The largest discrepancy between the model in this work and the existing data is in the worst-case (daytime) analysis, which shows a factor of 3.85 difference. This is likely due to a discrepancy in how margin is calculated. The model in this work directly calculates the power received and power required values (Eq. 13 and 29) and uses the ratio (or difference in log scale) as margin. Biswas et. al does not explicitly describe the method used to calculate margin. We interpret this to be the ratio of the power received to power required. We apply the stated margins (4X for the nominal case, and 2X for the worst-case) to calculate the power required from the reported power received [131]. Another interpretation of margin is the ratio of signal photon flux to background flux. By inspection of Table 12, the maximum difference ratio between the signal flux values is a 2.12 factor between the daytime nominal cases and the background flux values show a maximum error of 18% for the nighttime cases. Margin interpreted as the ratio of signal to background flux shows an overall lower error compared to the ratio of power required to power received.

Updated models for the DSOC mission were also used for validation. The same values presented in Table 12 are used for comparison with the model in this work with slight changes. First, based on updated measured values, the transmitter loss has been updated to -2 dB to include optics and wavefront losses [148]. The receiver parameters are updated to reflect the measured 70% SNSPD efficiency from end-to-end testing and includes dark count rate [140], [144], [147], and the receiver diameter is set to 5 m to represent the Hale telescope. Three data sets from literature were used to capture DSOC's feasible data rates as a function of range. Figure 7 shows the calculated link capacity compared to existing literature.

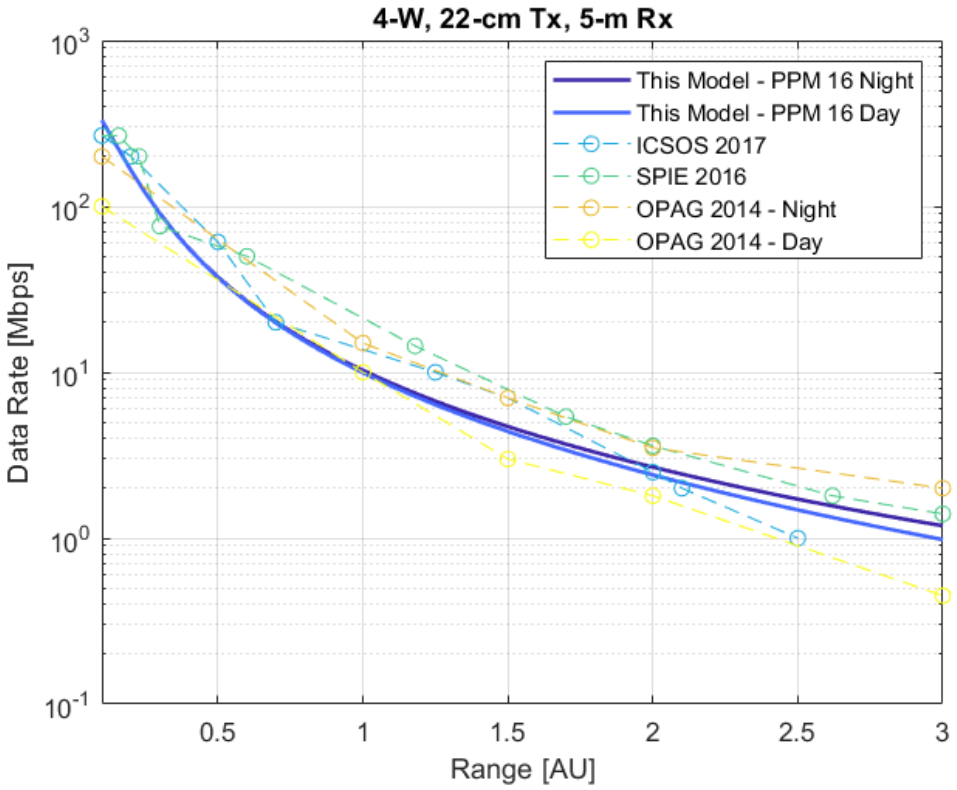

Figure 7: Capacity Results from The Model in This Work Compared to Existing Literature [66], [138], [140], [142].

There is a noticeable difference between the day and night capacity cases produced by this work compared to [138] day and night capacity. This may be attributed to a change in receiver FOV to optimize data rate, which is discussed in [66] but not modeled in this work. Using a smaller receiver FOV could increase receiver sensitivity (require less power for a given signal and increase SNR) which would result in a higher capacity in day or night conditions. This could also be from different realizations of atmospheric conditions. Biswas reports using MODTRAN to model atmospheric conditions but does report the realization of the random process. This would affect the difference between night and day data rates reported in OPAG.

Overall, both scenarios which require different model inputs show reasonable agreement with the existing literature. Chapter 4 discusses how to apply this model to predict the performance of systems that leverage multiple simultaneous optical links.

3.2 Protocol Validation

The protocol performance is verified using a model developed by Atakora for terrestrial optical communications in 5G backhaul [118]. Atakora uses several optimal set algorithms to compare relative performance, however, this work uses a simplified version of the author's time-based, delay minimization S-AP and S-HEU algorithms. With the help of the author, additional data points were provided from the models described in [118] specially for the broadcast ("multi-cast") S-AP and S-HEU cases for this work.

This comparison uses five static receiver nodes positioned at arbitrary positions defined as (40, 160), (80, 130), (20, 170), (42, 160), (23, 165) meters and a transmitter at (0,0). The transmitter rotates in a clockwise direction and determines if a set can be formed with the nodes in its field of view. It then transmits to the set (or single node), then repeats the sequence until all nodes have established contact. The transmitter uses 60 mW of output power and has a positioning uncertainty of 3 m corresponding to GPS positioning uncertainty. Each receiver uses a 12 mm aperture with a sensitivity of 6 photons/bit. The transmitter divergence is designed to be adjustable as needed to accommodate as many receivers as possible within a set. Figure 8 shows a layout of the simulated space with the nodes grouped together in sets as determined by this work.

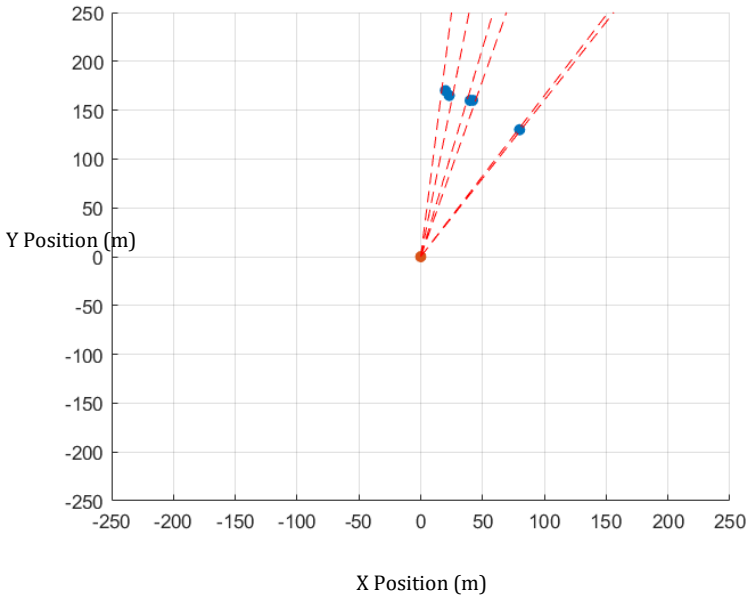

Figure 8: Simulated Network Consisting of 5 Receiver nodes and 1 Transmitter Node

The author shows that the S-HEU and S-AP results output the same results for this configuration[2]. Each algorithm groups the nodes in a total of 3 sets, and achieves an 85.7, 129.7, and 228.6 Gbps per set, respectively. The node positions and terminal characteristics are used as inputs to the model proposed in this work then compared to the Atakora results. The protocol inputs are broadcast network and WDMA with 5 users. Table 13 summarizes the outputs of this work as well as the Atakora results. Figure 9 shows the capacity plotted together along with the uncertainty bounds from the position +/- 3m position uncertainty.

Table 13: Comparison of Results from 5G Terrestrial Multicast Optical Network [118] vs The Model In This Work

	5G Backhaul	The Model in This Work
Nodes per Set	{2,2,1} Total: 3 sets	{2,2,1} Total: 3 sets
Capacity per Set (Gbps)	85.7 129.7 228.6	88.45 125.22 223.1
Error	-	3.2% 3.5% 2.4%

[2] M. Atakora, email correspondence, March 2021

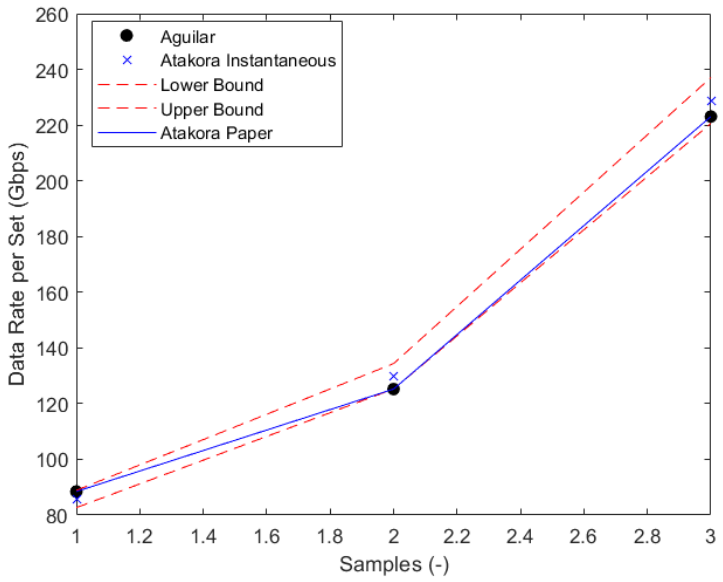

Figure 9: Data Rate per Set Validation. Note position uncertainty bounds the capacity uncertainty since it is assumed the transmitter divergence changes as a function of node position within its FOV

The predicted data rate per set using a broadcast configuration shows good agreement with Atakora's results, with a maximum error of 3.5% and within the bounds of uncertainty. The underlying assumption that each node's individual link contributes to the overall system capacity holds, which is key in estimating system throughput performance and round-trip delay. This method can now be extended to estimating the performance of space-based systems.

Chapter 4

Enabled Architectures

This chapter presents the results from the model described in Chapter 2. To start, detailed trades between TDMA- and WDMA-enabled architectures are discussed. Parameters are down-selected and flowed into the scenario analysis. Two different scenarios are selected for evaluation: a LEO swarm and a deep-space network. Both cases utilize multi-user lasercom.

4.1 WDMA Trades

4.1.1 Size, Weight, and Power for WDMA

In terrestrial applications, WDMA and WDM systems scale well because there are few resource constraints. A common implementation approach is to use a demultiplexer to separate wavelengths transmitted within a fiber, then use dedicated optics and electronics for each wavelength to process the signal [149]. This approach lends itself well to systems with large SWaP budgets, such as typical ground-based systems. It is unknown if the WDMA architecture scales well with space-based systems.

WDM receivers are often passive devices with low-power opto-electronics in the receiving chain, so it is assumed that the additional power required to scale to multiple wavelengths is negligible compared to the total payload power. Receiver size is highly dependent on architecture realization, the build specifics, and is beyond the scope of this research. This model uses a mass estimate to determine an upper limit to the number of supported users given a WDMA architecture and technology.

For this study, the upper limit of a lasercom terminal is set to 31% of the total spacecraft mass based on average payload mass [150]. Several spacecraft masses are used for comparison and are summarized in Table 14.

Table 14: Examples of Satellite Missions with Corresponding Mass and Size Classification

Representative Mission/Satellite	Size Classification	S/C Mass (kg)	Terminal Mass (kg)
3U [151]	Cubesat	6	1.86
6U [151]	Cubesat	12	3.72
12U [151]	Cubesat	24	7.44
OneWeb [152]	Smallsat	150	46.5
Starlink [153]	Smallsat	260	80.6
Lunar Atmosphere and Dust Environment Explorer (LADEE) [154]	Small/Medium	383	118.73
Mars Reconnaissance Orbiter (MRO) [155]	Medium/Large	1000	310

An additional relationship between number of users *n* and spacecraft mass is formulated.

$$m_{req} = m_0(1 + 0.1n) \tag{46}$$

$$m_0 = m_{pwr} + 2m_{opt} \tag{47}$$

Where m_{req} is the required mass to support an optical transceiver, in kilograms, for n number of users, m_0 is the mass of a single-user, point-to-point optical transceiver in kilograms, and m_{pwr} and m_{opt} are the mass of the optical head and opto-electronics in kilograms, given in Chapter 2. It is assumed the mass of the terminal grows by 10% to account for the added optics and opto-electronics on the receiver size. The optical mass is doubled as it assumes in order to support more than a single user simultaneously, another aperture shall be positioned along a different axis to increase the total transceiver FOV.

Four terminals corresponding to each size classification are evaluated and results are shown in Figure 10-12. The Cubesat case assumes a 500-mW transmitter with an 8-cm primary aperture, which is representative of point-to-point lasercom Cubesat missions [23], [48], [51], [54]. The fiber-based terminal can support up to 6 users in a 6U platform and 22 users in a 12U platform,

while the PIC-based terminal can support 14 users in a 3U platform, and more than 30 users in a 6- and 12U platform.

The smallsat case uses a total output power and aperture diameter to 1 W and 10 cm, respectively. This reduces the total number of users supported by the fiber system to 11 in a 12U platform, but can be used in larger spacecraft to support more than 50 users. For large mega-constellations with thousands of satellites and globally available ground stations, this estimate suggests a small fiber-based terminal may support up to ~200 users and requires minimal modifications to existing technology. For PICs, a 12U platform may support up to 44 users, 328 users for a OneWeb-sized satellite, and 500+ users for all other satellite size classifications.

The medium-sized case uses power and aperture size representative of the DSOC mission with 4-W output power and 22-cm aperture diameter [66]. While this architecture is not compatible even with large cubesats, the fiber-based terminal may support 19 users for a OneWeb-sized satellite, 40 users for a Starlink-sized satellite, 79 users for a LADEE-sized satellite, and 181 users for an MRO-sized satellite. The PIC-based terminal may support 34 users in a OneWeb-sized satellite, 67 users in a Starlink-sized satellite, 128 users in a LADEE-sized satellite, 282 users in an MRO-sized satellite.

The large-spacecraft terminal is based on estimates by [66] for EIRP requirements that could be made for immediate improvements to the DSOC terminal. Output powers on the order of 20 W and apertures of 50 cm can be achieved in the near future for higher performance deep-space optical communication terminals. Only LADEE-sized and MRO-sized spacecraft can accommodate terminals with these modifications, which makes sense considering this terminal is designed for deep-space applications. Fiber-based transceivers may support 3 users in a LADEE-sized spacecraft, and 18 users in an MRO-sized spacecraft. PIC-based transceivers may support 7 users in a LADEE-sized spacecraft, and 26 users in an MRO-sized spacecraft.

In all instances, PICs can support more users for a given spacecraft size, or the same users for less mass. This is expected due to the known SWaP reduction seen in terrestrial fiber systems. These results come with many caveats; one worth repeating is that current state-of-the-art PICs have not yet been demonstrated at output powers greater than a 100's of milliwatts at the time of writing. Additional technology development is required to get PICs to watt-level or 10+ watt-level output powers. This further motivates the need to develop a path-to-flight for PICs and increase

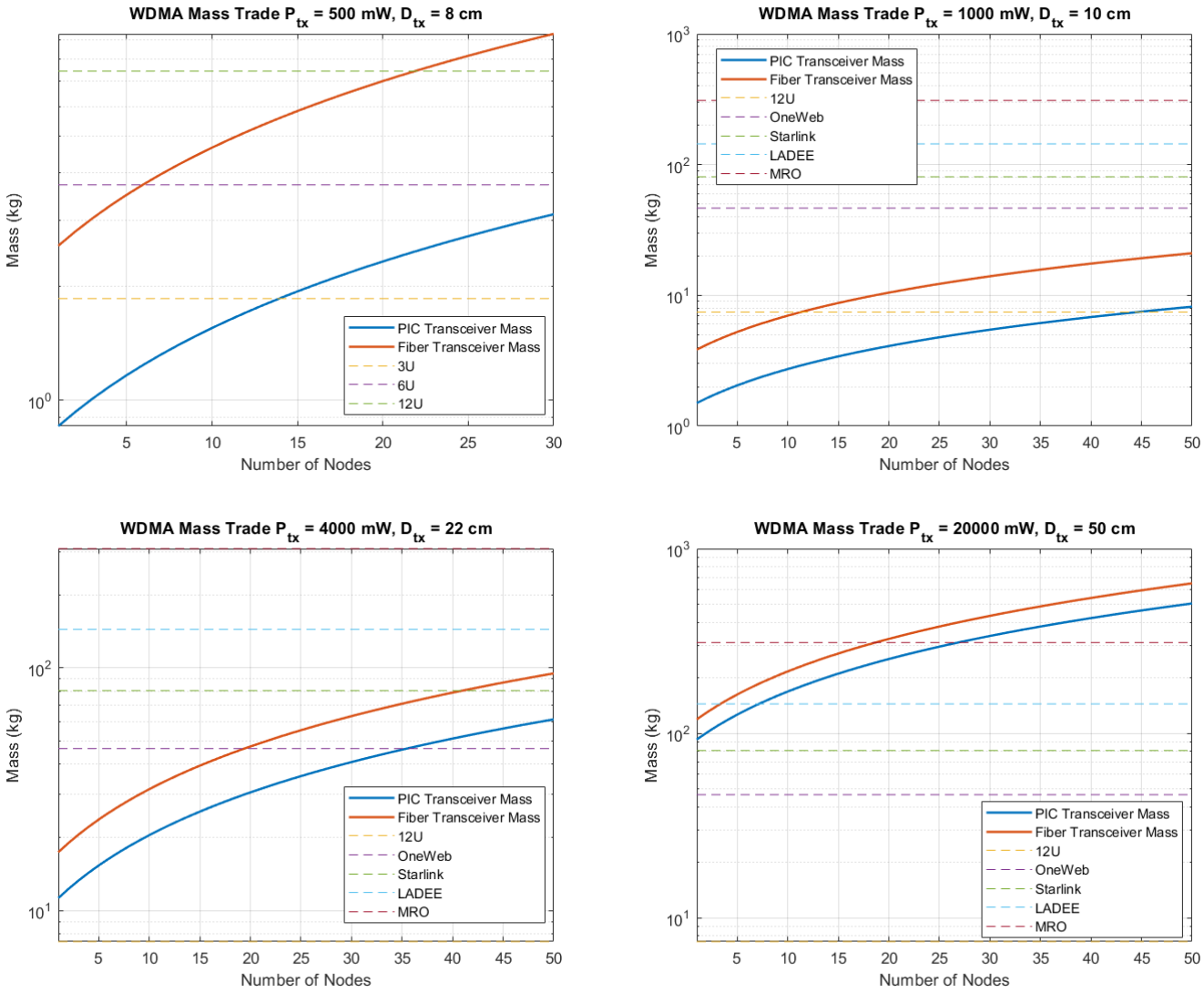

Figure 10-12: WDMA Mass vs Number of Nodes Trade for Different Spacecraft Sizes.
(Top-Left) Cubesat; (Top-Right) Smallsat; (Bottom-Left) Medium; (Bottom-Right) Large

the TRL for PIC-based transceivers.

4.1.2 Bandwidth Limitations for WDMA

It is important to verify the performance of PICs in the space environment. A point of particular concern is how PICs will perform in the radiation environment as they depend on charge movement and electron energy transitions to operate properly [69].

A test performed by Gambini with InP PIC transmitters (C-band) show a wavelength shift of ~0.9 nm after 50 krad(Si) absorbed gamma radiation [114], which is an environment representative of a 10-year LEO mission with 300 mils (7.62 mm) of shielding, which is typically considered substantial protection for near-Earth missions [156].

Wavelength shifts require widening the optical bandwidth filters on transceivers and reduces the total number of users that may use the telecommunication C-band wavelengths, which span 1530-1565nm. Assuming the wavelength shift can be either red or blue (+/-), each user would need to be allocated 2-nm of optical bandwidth. This implies PICs have an upper limit of 17 users for any spacecraft platform unless additional telecommunication bands, such as the O-band (1260-1360 nm) or L-band (1565-1625 nm) are used. The latter requires additional technical development.

The bandwidth limitation imposed by drifting PIC wavelengths implies for deep-space applications, fiber-based systems may support equal or more users than PIC-based ones.

4.2 TDMA Trades

4.2.1 Timing for TDMA

In PPM, narrower slot widths times (*i.e.,* shorter pulses) enable higher data rates for a given order. In order to resolve pulse positions within a given symbol, precision timing is key for low-error, high-rate communications. Within the context of TDMA, reducing slot width enables higher data rates that may compete with WDMA, which operates at longer slot widths. This increase in data rate follows the PPM data rate:

$$R_{PPM} = \frac{\log_2 PPM}{T_s \, PPM}$$

Where PPM is the PPM order and Ts is the slot width which can range from 0.125, 0.25, 0.5, 1, 2, 4, and 8 ns under the CCSDS optical communication recommendations [157]. Using PPM 16 and a slot width of 0.5 ns, which is used by current state-of-the-art optical communication systems [66], [146], a slot width gain, G_{Ts} can be found:

$$G_{T_S} = \frac{R_{PPM}(T_s)}{R_{PPM}(0.5\ ns)} = \frac{T_s}{0.5\ ns}$$

This suggests that by reducing the slot width to 0.25 ns or 0.125 ns, the corresponding data rate gain should be a factor of 2 or 4, respectively.

Achieving narrower slot widths requires advancement in timing technology. Current state-of-the-art systems are limited in the time-domain by short-term random fluctuations and disturbances known as jitter, which is analogous to phase noise in the frequency domain [52]. Serra shows to achieve an uncoded BER of 10^{-6} with PPM, the total system jitter must be less than 200 ps [52]. CCSDS Optical Communication Physical Layer Recommended Standards [158] requirements state that the RMS jitter shall be <10% of the slot width. This suggests in tandem with the recommended slot widths, improvements to timing must be made in order to achieve lower slot widths (e.g., anything below 1.2 ns).

Different components are used to achieve precision timing, and while an exhaustive list is out of the scope of this work, the reader is directed to [52] for a complete overview and discussion. Current relevant systems include the DSOC ground receiver, which utilizes a TDC with the SNSPD array to time-stamp pulses, and has recorded a total system jitter < 120 ps [145]–[147]. Atomic clocks are ubiquitous in timing and navigation systems both in space and on the ground in order to meet accuracy requirements. Chip-Scale Atomic Clocks (CSACs) have gained popularity in recent years, especially for CubeSat applications, due to their low SWaP and power requirements [51], [52], [159].

Serra demonstrated the viability of current COTS CSACs for both time transfer and lasercom applications [52]. A novel, lasercom transceiver, Miniature Optical Communications Transceiver (MOCT), was built using a CSAC to generate pulses in an FPGA-based modulator, and a TDC to timestamp the received signal. End-to-end testing showed < 200 ps precision time can be achieved for greatly reduced SWaP compared to other systems with similar performance [52]. Despite the impressive timing performance of these systems, a 10X improvement to current state-of-the-art

precision timing is required to operate at the narrowest recommended slot width (0.125 ns) to meet the CCSDS standard.

4.2.2 Capacity Limits for TDMA

The upper limit on a strict, time-allocation based TDMA network is bounded by individual link capacity, as the underlying assumption is that only a single user may occupy the channel at a given time. The delay, however, is directly proportional to the number of users within a network as well as the allocated time for each individual user as shown in Eq. (49).

$$d_{tdma} = d_{tx} + d_n(n-1) \tag{48}$$

$$d_{tx} = d_n$$

$$d_{tdma} = d_n n \tag{49}$$

Assuming each user waits their full transmission period regardless of whether they have data or not, the relationship simplifies to a simple linear equation where d_n is the individual user transmission time and n is the number of users within the network.

Figure 13 shows the TDMA delay in units of seconds within a system as a function of users and individual transmission time. By maximizing the number of users (30) and transmission time (100 sec), the maximum delay is 3000 sec (as expected), while the lowest achievable delay for more than 1 user is 2 ms. This approach can aid in sizing TDMA access time slots for different scenarios. For example, compared with other physical delay limitations such as propagation delay (limited by the speed of light through vacuum), TDMA access delay may be small in comparison.

Figure 15-15 show access delay normalized to propagation delay at 400 km, which is representative of a LEO mission, and 1 AU, which is representation of a deep-space mission. At 400 km, TDMA access delay for 2 users at 1 ms transmission time is 1.5X the propagation delay. This means user transmission time in a LEO or shorter-range mission should be kept as low as possible to prevent significant delay. At 1 AU, up to 5 users can be allocated 100 seconds of transmission time before approaching propagation delay. This means larger user transmission times may be allocated without incurring significant delay in the network. For the scenario analyses, the LEO

mission using TDMA uses 1 ms user transmission time, and deep-space uses 60 sec transmission times.

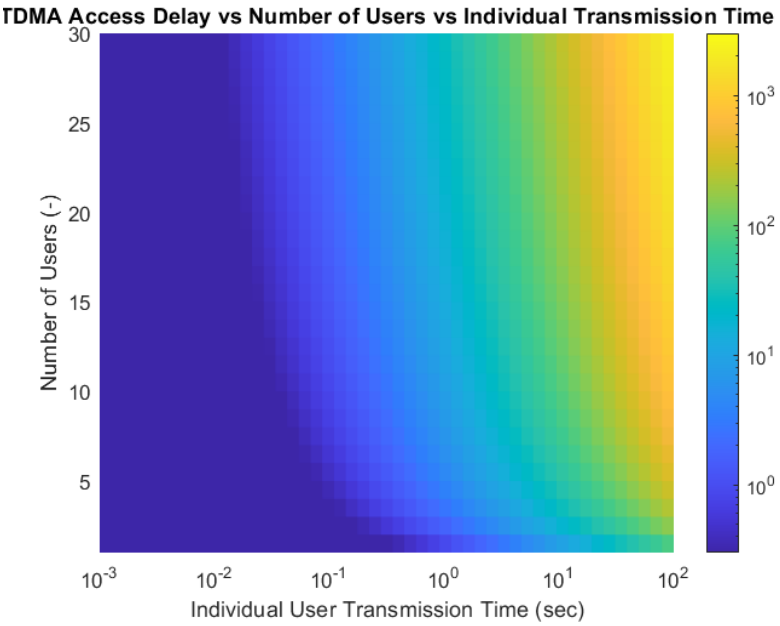

Figure 13: Access delay as a function of number of users and allocated user transmission time. Total delay increases linearly with number of users at a given user transmission time.

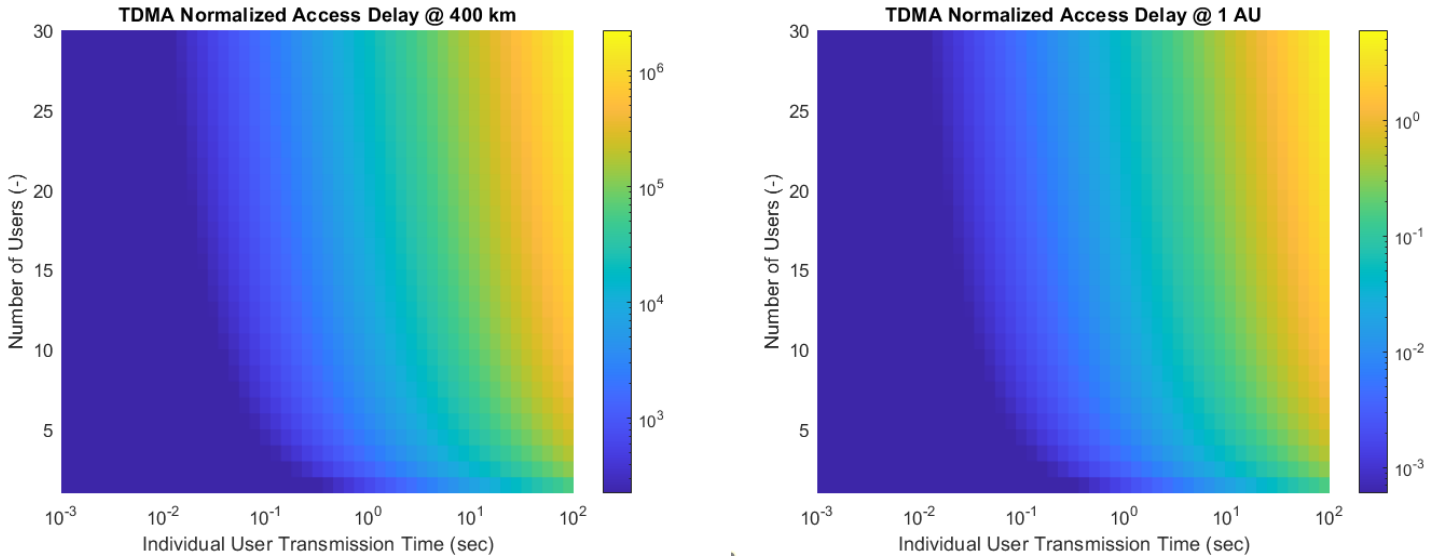

Figure 15-15: Access delay normalized to physical limitations Introduced by the channel (propagation delay). (Left) Access delay normalized to propagation delay at 400 km. (Right) Access delay normalized to propagation delay at 1 AU. Transmission delay should be selected for each scenario such that the sum of the delay within the system does not significantly increase. For a LEO system, this corresponds to user transmission times around 1 ms, while deep space systems may use 10's of seconds for each user without adding significant delay.

4.3 TDMA vs WDMA

A direct comparison of access methods for similar architectures is made in this section. Considering the limitations for both, such as the bandwidth limitations in WDMA, and the timing limitation in TDMA, bounds can be introduced that enable performance estimates to be made.

In terms of data rate performance, WDMA systems are difficult to outperform. This can be seen not only from the results shown in Figures 17-20, but also the architectures currently used in terrestrial fiber communications, data centers, etc. It is expected that long-term solutions will likely use WDMA-based architectures, however, TDMA is a viable interim solution. Precision timing transceivers capable of supporting 0.5 ns slot widths have been demonstrated in lab and on-orbit [51], [159], while realizing WDM-scalable hardware for space applications is still an active area of research [160], [161]. Based on lower complexity and higher TRL, we look at ways in which TDMA could approach the theoretical WDMA performance as a bridge until WDMA hardware is realizable.

One of the ways TDMA could rival WDMA is in increased output power for each transmitter. As mentioned in Section 4.1.1, near-future improvements to deep-space transceivers include output power up to 20 W. Figure Figure 16Figure 17 show the capacity curves for TDMA-based systems using different transmit powers compared to a WDMA-based system using a 4-W transmitter. The range is set to 1 AU and the individual user transmission time is 100 ms. As expected, by increasing the transmit power, TDMA can match or exceed WDMA capacity in specific cases. For an 18-20-W transmitter with 30 users within the network, TDMA system capacity is greater than WDMA up to 30 users. Note that 4-W WDMA and 4-W TDMA are not equal at 1 user. This is due to the assumption that WDMA requires a slightly larger optical filter bandwidth for each user, while TDMA can be narrower since only a single wavelength is used. The TDMA curves are constant across all users because while individual user data decreases proportionally to the inverse of number of users, the, the total system capacity is assumed to be the sum of all users, which scales proportionally with the number of users.

These results also suggest that over a range of 1 AU, a network of 30+ users could use TDMA with 20-W transmitters and achieve a network capacity of ~600 kbps. While modest, this type of network could increase availability and network coverage deeper into the solar system than current state-of-the-art. This is further discussed in Section 4.5.

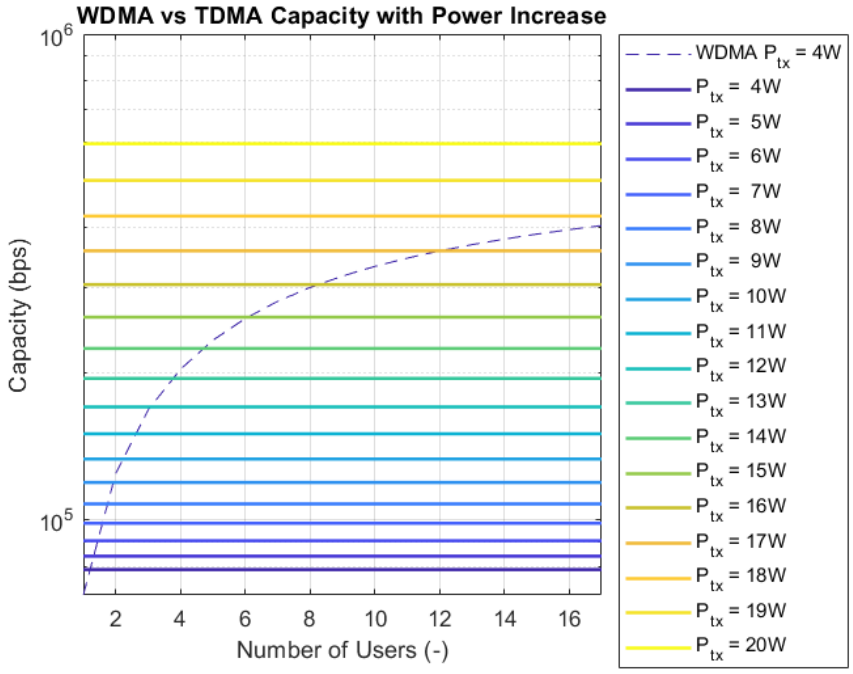

Figure 16: WDMA vs TDMA with increasing transmit power. WDMA is fixed at a 4 W output power. The proposed application for this type of terminal would be a deep-space mission, which requires output powers on the order of 10's of watts to increase link ranges beyond Mars [66].

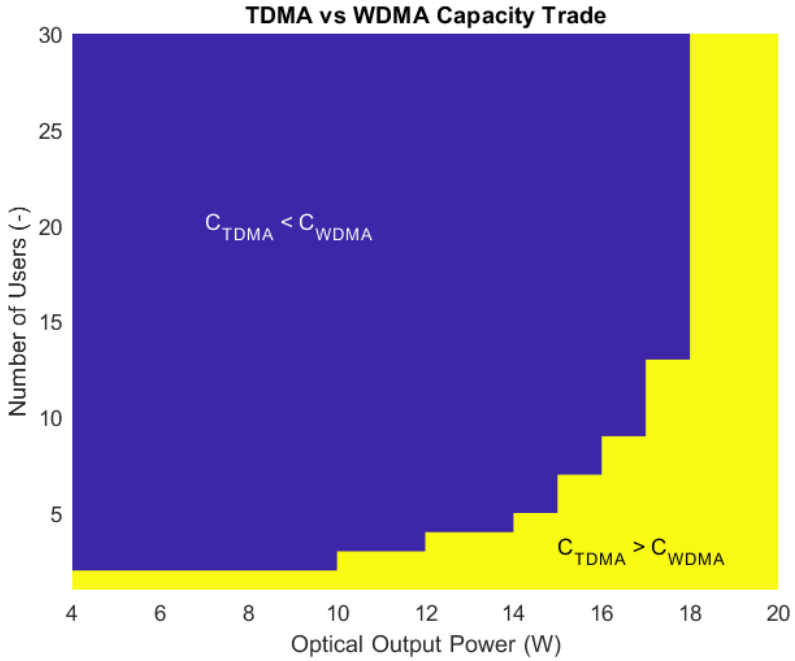

Figure 17: Data rate comparison between TDMA and WDMA as a function of output power and number of users. WDMA transmit power is fixed at 4 W. Yellow regions indicate combinations

where the supported data rate of a TDMA system is higher than WDMA, while blue is the opposite. The proposed use-case for this is again deep-space for terminals requiring high output power.

The corresponding LEO case is shown in Figure 18-20. Unlike the deep-space case, there is less of trade between higher-power TDMA and WDMA. Note that WDMA is scaled to 250-mW output power based on [51], [107], and TDMA ranges from 250 mW-2 W of output power. Only single-user TDMA outperforms WDMA. Again, this is due to the increased optical bandwidth assumption associated with WDMA. The high-power TDMA capacity in this instance is limited by slot width and PPM order and the capacity saturates at 500 Mbps using PPM-16 and 0.5 ns slot widths.

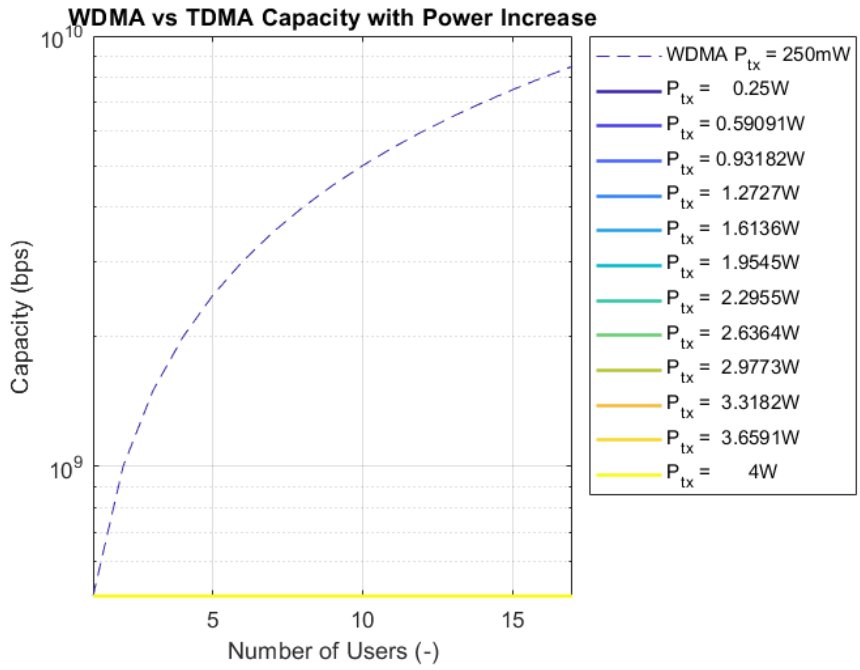

Figure 18: WDMA vs. TDMA with increasing transmit power. WDMA is fixed at a 250-mW output power. This is representative of LEO system which requires lower output power. Aside from a single user system, the total system capacity supported by WDMA is greater than TDMA.

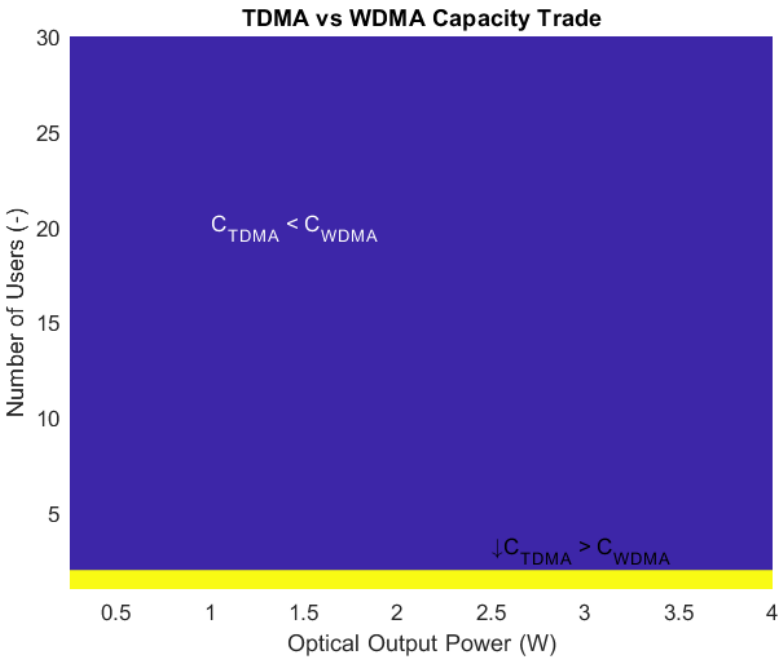

Figure 19: Data rate comparison between TDMA and WDMA as a function of output power and number of users. Yellow regions indicate combinations where the supported data rate of a TDMA system is higher than WDMA, while blue is the opposite.

4.4 LEO swarm

This section discusses multi-user optical communications for cubesat LEO missions. First, the LEO swarm case is introduced. Different architectures and access schemes are analyzed, and a recommended network architecture is presented.

4.4.1 ISOC Overview

The LEO swarm mission is based on a novel transceiver architecture known as the Inter-Satellite Omnidirectional Communicator (ISOC) [54], [119]. ISOC is a novel lasercom transceiver designed to support multiple simultaneous OISLs in CubeSat swarms. The terminal is designed to fit in a 1U (10x10x10 cm^3) structure and nominally operates in a 6U bus [119], but is not limited to Cubesat-sized busses. The transceiver is comprised of an array of transmitters and receivers arranged in a truncated icosahedron geometry enabling near full-sky FOV (4π steradian). A detector is placed at each vertex for communications and Pointing, Acquisition, and Tracking (PAT) Angle of Arrival (AoA) estimation. Each transmitter is comprised of miniature telescope with collimation optics, a MEMS mirror for ±36° beam steering, and a 1-W, 850-nm laser. Figure 20 depicts the transceiver. A

full overview of the transceiver architecture can be found in [54], [119]. ISOC was selected as a case study for the LEO scenario due to its potential to support multiple simultaneous optical links.

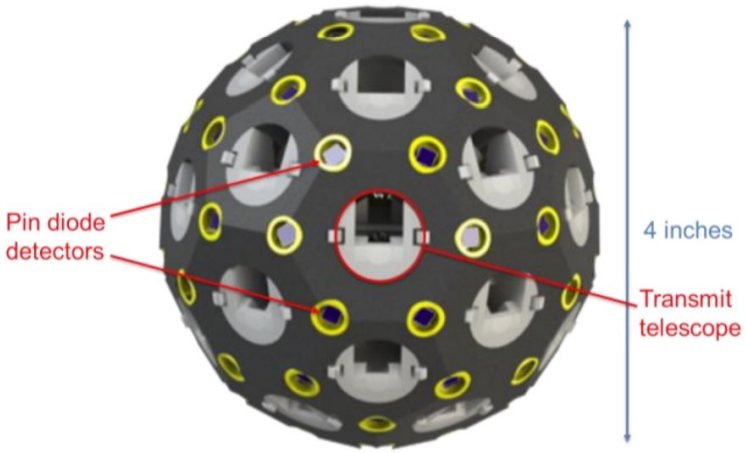

Figure 20: ISOC Transceiver Geometry and Architecture. ISOC leverages a truncated icosahedron chassis with a single transmitter centered on each face and photodetectors placed at the vertices. Reproduced with permission by Dr. Velazco

4.4.2 Mission Configuration

A mission known as Q4 has been proposed to demonstrate the ISOC transceiver [119]. Featuring a total of four, 6U cubesats, Q4 is a LEO swarm at ~400km altitude, 51.6° inclination. A single cubesat (leader) is positioned at the center of the swarm while the three remaining (followers) co-orbit the leader. The leader is placed in a circular orbit while the followers are placed in a slightly elliptical orbit. This work used the underlying orbital parameters (altitude and inclination) to create an STK simulation representative of Q4 and produce the ephemeris data required for the model input. Table 15 summarizes the orbital parameters.

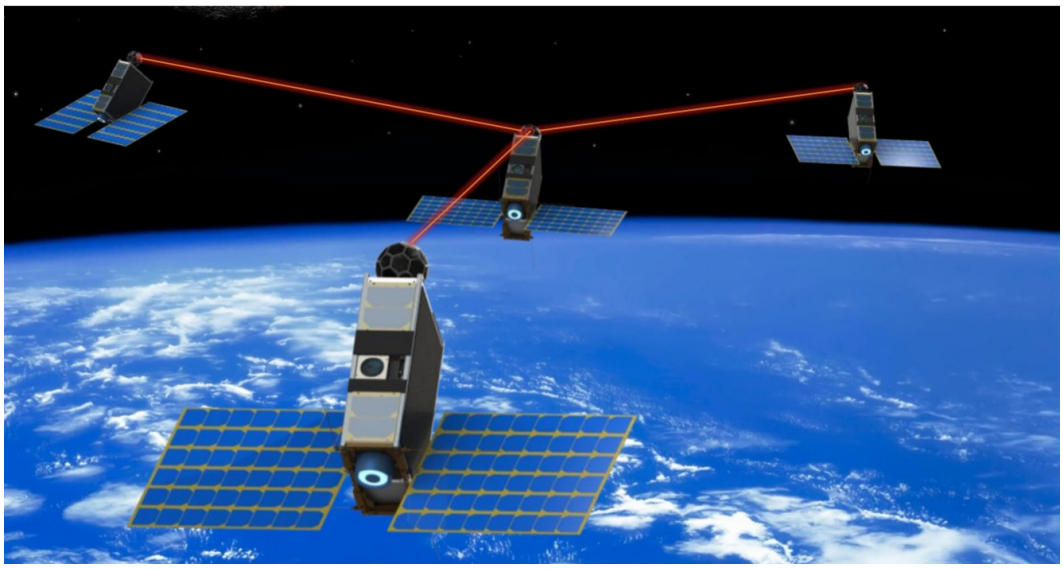

Figure 21: Notional Q4 Mission Respresentation. Four, 6U cubesats are placed in LEO. Three of the 6U's co-orbit a center spacecraft. All are equipped with ISOC transceivers. Reproduced with permission from Dr. Velazco.

Figure 22-24 show the 3D and 2D ground tracks produced by the STK analysis for a single orbit (~90 minutes). The scale of the default STK 3D and 2D viewers illustrates how closely spaced the ISOC spacecraft are relative to each other (up to 30 km relative range). Figure 24 shows a magnified view of the co-orbiting spacecraft. Three instances from the orbit spaced 16.5 minutes apart are captured to show the co-orbiting mechanics in Figure 24.

Table 15: ISOC Swarm Orbital Parameters

S/C	Semimajor Axis (km)	Inc (°)	Eccentricity	Argument of Perigee ω (°)
ISOC_0	6788.1	51.6	0	-
ISOC_1	6794.9	51.6	1.00E-03	90
ISOC_2	6794.9	51.6	1.00E-03	180
ISOC_3	6794.9	51.6	1.00E-03	270

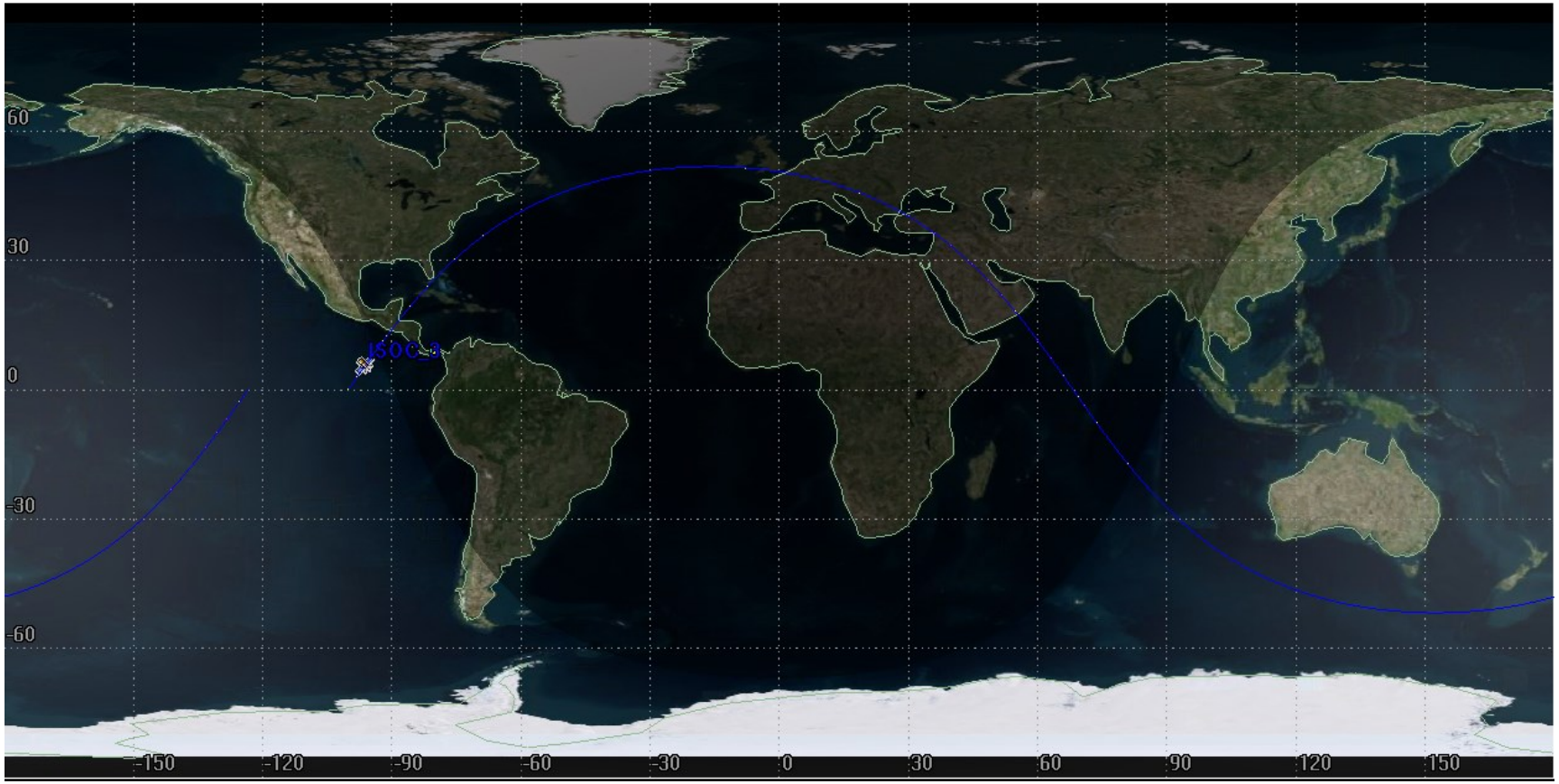

Figure 22: STK 2D Ground Track for the Simulated LEO Scenario with the ISOC Terminal

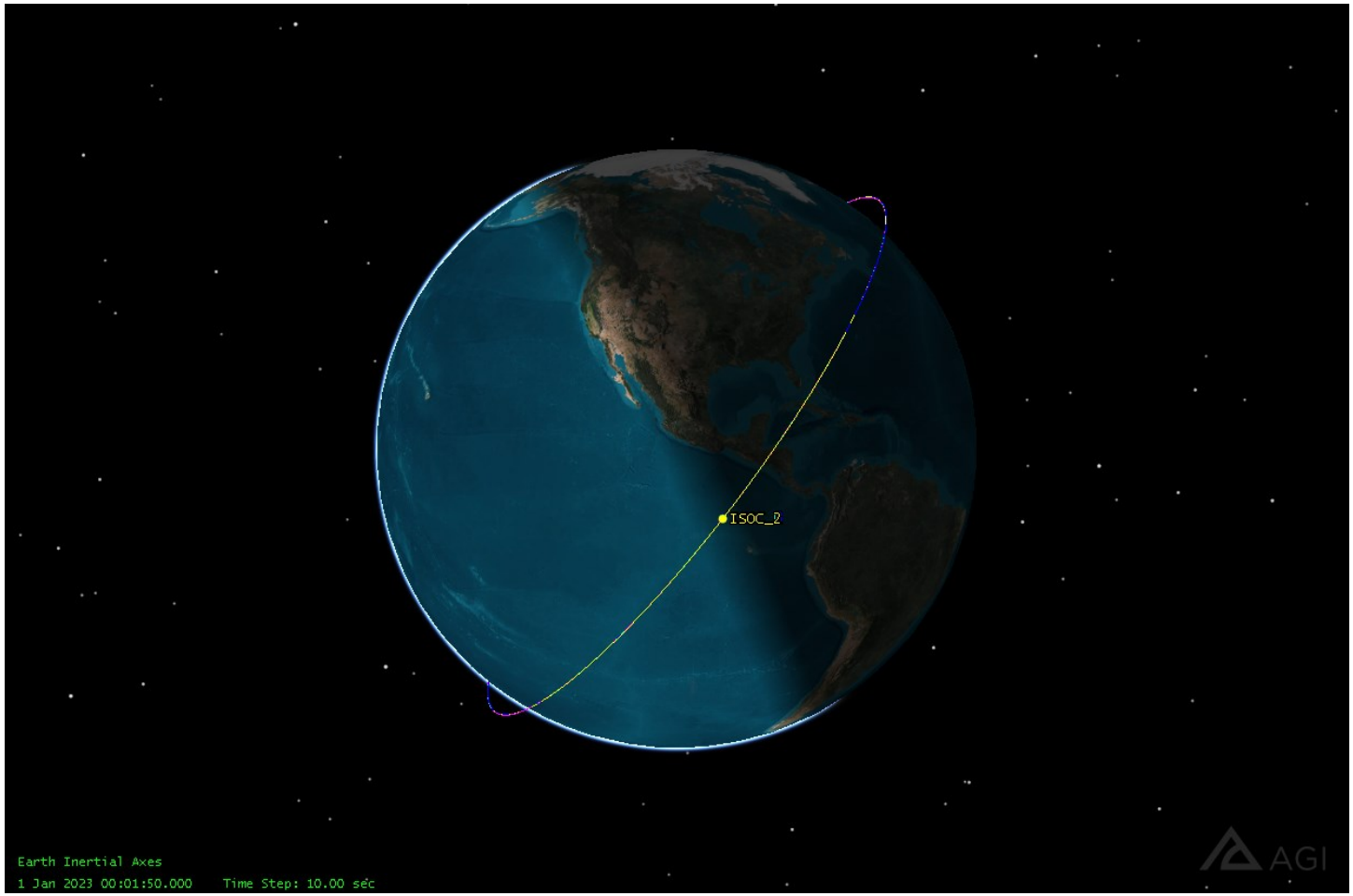

Figure 23: STK 3D View of the LEO Scenario Using the ISOC Terminal

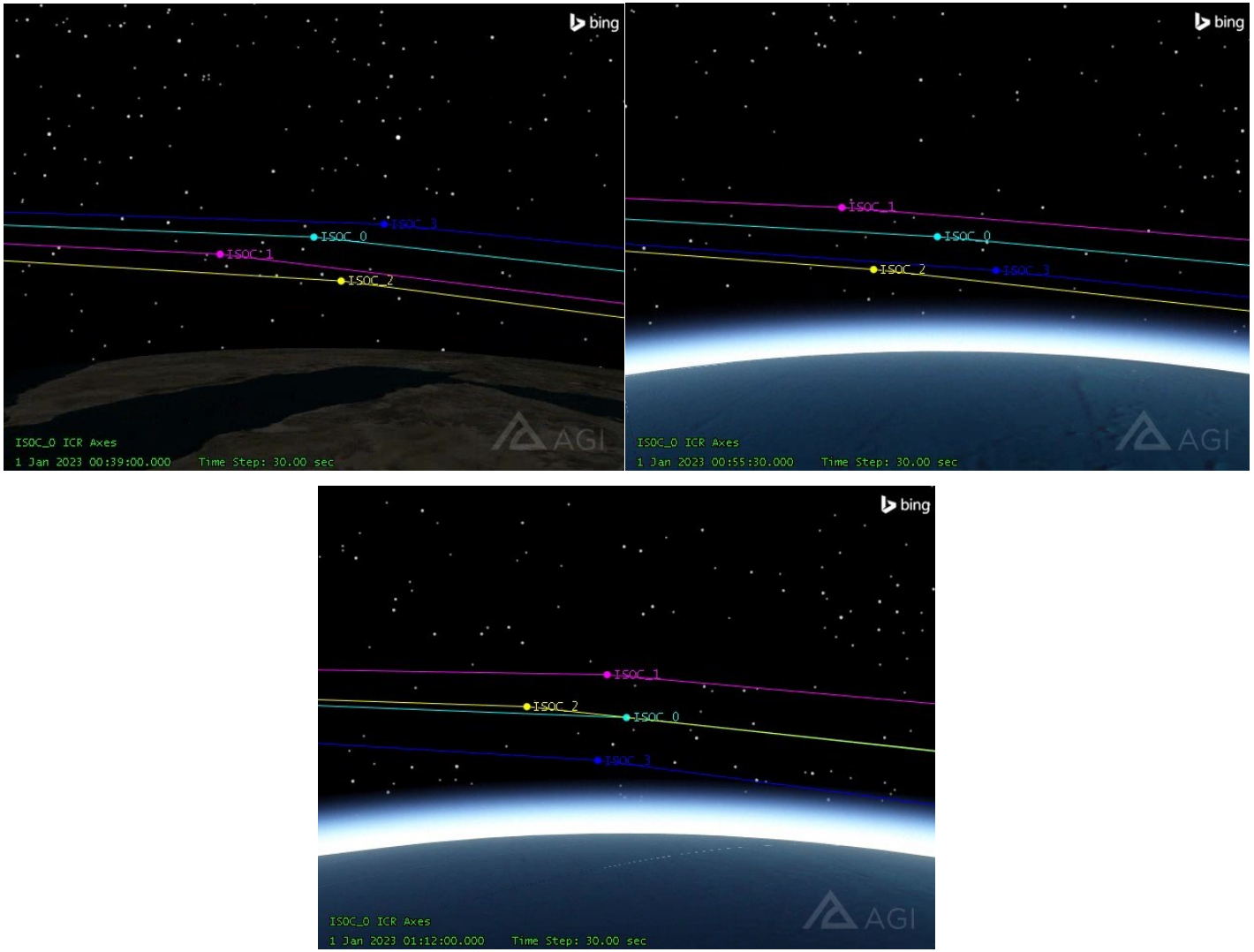

Figure 24: Zoomed-in Image Frames of ISOC Orbit Position Instances from STK Analysis. Frames are spaced apart in time by 16.5 minutes. ISOC_0 remains at the center for all frames while ISOC 1-3 co-orbit the Earth and center ISOC.

4.4.2.1 Doppler Analysis

One of the primary concerns for communication systems is managing the carrier frequency change that occurs from Doppler shifts. The relative velocity between two bodies can lead to carrier frequency shift that is out-of-band on the receiver. Using the ephemeris data velocities, the carrier frequency shift can be calculated by:

$$\Delta f = \frac{\Delta v}{c} f_0 \tag{50}$$

Where Δf is the change in carrier frequency in Hz, Δv is the difference in velocity between the spacecraft (also known as the range rate) in meters per second, c is the speed of light in meters per second, and f_0 is the original center frequency. The carrier frequency in a vacuum is related to the optical wavelength through the relationship:

$$f = \frac{c}{\lambda} \tag{51}$$

Where f is the resultant frequency in Hz, c is the speed of light in meters per second, and λ is the wavelength in meters. Table XX summarizes the minimum, maximum, and average range and range rate between each ISOC spacecraft. The expected Doppler shift is calculated for each min, max, and average value using Equation 50.

Table 16: Range, Range Rate, and Doppler Shift Between All ISOC Spacecraft Over a Single Orbit

S/C	Min Range (km)	Max Range (km)	Mean Range (km)	Min Range Rate (m/s)	Max Range Rate (m/s)	Mean Range Rate (m/s)	Min Doppler Shift (MHz)	Max Doppler Shift (MHz)	Mean Doppler Shift (MHz)
0 - 1	6.72	15.28	9.80	-8.73	8.49	-0.76	-10.27	9.99	0.89
0 - 2	6.56	13.56	10.00	-7.37	7.64	0.65	-8.67	8.99	-0.76
0 - 3	6.20	17.74	10.43	-10.46	6.48	-3.53	-7.63	12.31	4.16
1 - 2	9.55	17.47	13.54	-11.94	9.67	0.89	-11.38	14.05	-1.02
1 - 3	9.55	17.47	13.54	-17.50	12.99	-4.30	-15.28	20.59	5.08
3 - 2	13.45	30.59	20.06	-11.94	10.55	-3.87	-12.41	14.05	4.57

The maximum change carrier frequency occurs between ISOC 1 and 3 at 20.59 MHz. Using Eq. 51, to solve for wavelength, the new carrier wavelength with the maximum doppler shift is 849.99 nm.

4.4.3 Link Analysis

First the TDMA relay and mesh network results are presented, then the WDMA relay and mesh network results. Individual point-to-point links are presented followed by the total system level performance for each configuration. The parameters used in the ISOC analysis is summarized in Table 17. To keep the power requirements low and three multiple concurrent uses conservative, it is assumed the peak output power is 1-W per transmitter with uniform intensity over the 3 dB beamwidth. The effective receiver diameter is less than the physical ISOC area because all incident photons at the terminal cannot be collected by detectors alone. Ten to twelve detectors in the truncated icosahedron geometry are visible on any given face not including blind spots introduced by the bus or solar panels.

Table 17: LEO Terminal Parameters [54], [105], [162]

	Value	Units
BER	1.00E+09	-
PPM	2.00E+00	-
Pointing Loss	-2.00E+00	dB
Access Delay	1.00E-03	sec
Alignment Delay	3.00E+00	sec
Transmitter Parameters		
Output Power	1.00E+00	W
1/e2 Beamwidth	3.00E+02	urad
Transmitter Losses	-1.00E+00	dB
Receiver Parameters		
Primary Aperture Diameter	2.13E+01	cm
FOV	4π	urad
Receiver Losses	-1.00E+00	dB
Sensor Gain	1.00E+02	-
Excess Noise Factor	3.95E+00	-
Responsivity	5.00E+01	%
Dark Noise	1.00E-01	nA

BW	1.00E+09	Hz

Assuming a minimum incident angle of 30°, the effective area of a bare MarkTech APD 07-005 receiver is 0.22% of the physical area (17.09 mm^2). By adding a biconvex or fisheye lens with a focal length of 10 mm and 6 mm clear diameter, the effective receiver area increases to 31.34% the physical area (25 cm^2) [105]. In the modified transmitter geometry with 7.2 mm diameters, the ~30% physical area assumption holds. While the number of vertices is reduced, more area is available at each point for detector arrays and larger focusing lenses.

Background noise sources include starlight, planet reflections, and solar interference within the system optical bandwidth. All sources will result in increased dark current levels when incident on the ISOC receiver. To mitigate noise current, it is assumed links will occur during eclipse. While this greatly reduces dark current otherwise produced by solar interference, star light and planet shine increase the noise floor and requires more received power to maintain the same BER and capacity performance.

4.4.3.1 TDMA Relay

The individual link capacity as a function of range between nodes is given in Figure 24 for the TDMA relay case. While data rate is sensitive to separation range, the relative range between spacecraft is small (30 km). Similar behavior to the analysis presented in Section 4.3 is seen in the ISOC analysis. The individual link capacity is relatively constant over time due to bandwidth limitations. Differences in relative range create discrepancies in individual links between terminals. For example, in Figure 26, ISOC 3 to ISOC 2 range is on average shorter than the ISOC 3 to ISOC 0 range, which leads to different supported data rates. The individual data rates however are all close ~ 250 Mbps and vary by ~4 kbps peak-to-peak. System capacity fluctuations can also be observed, but the system maintains a mean throughput of ~2 Gbps.

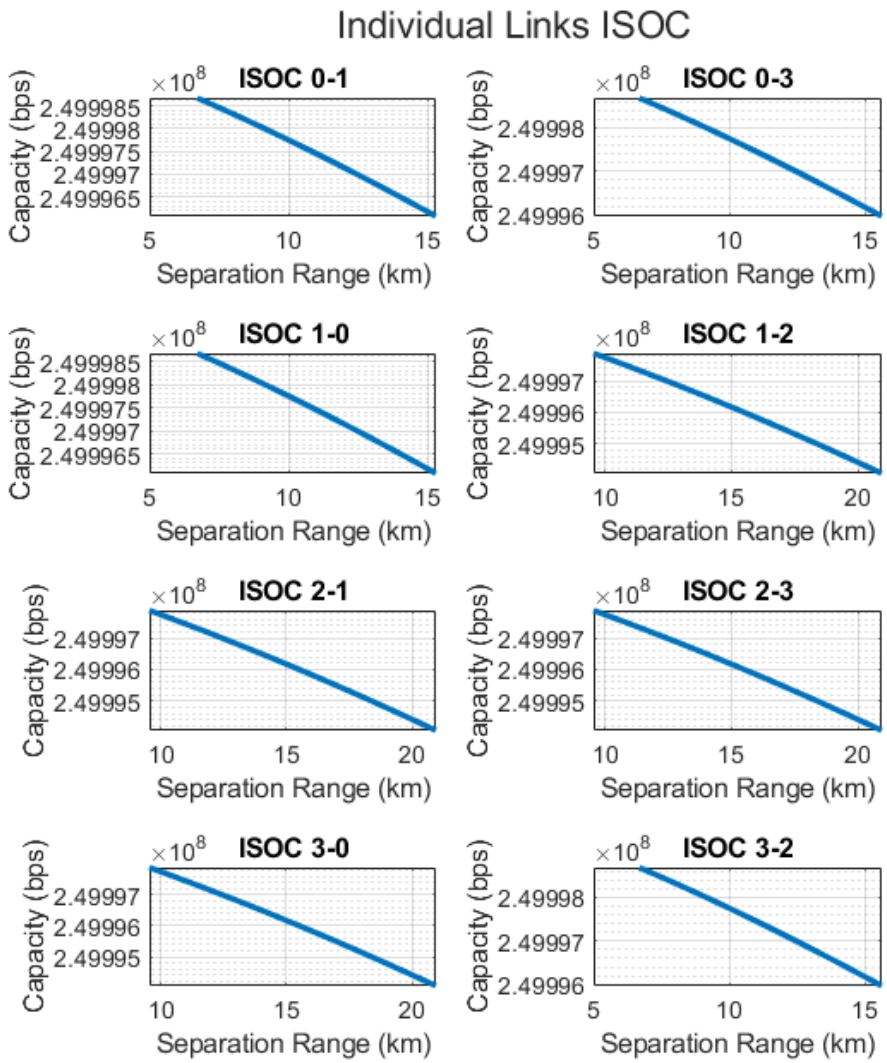

Figure 25: Individual Link Capacity vs. Range for TDMA Relay in LEO. Individual data rates are limited by bandwidth and average ~249 Mbps across all ranges.

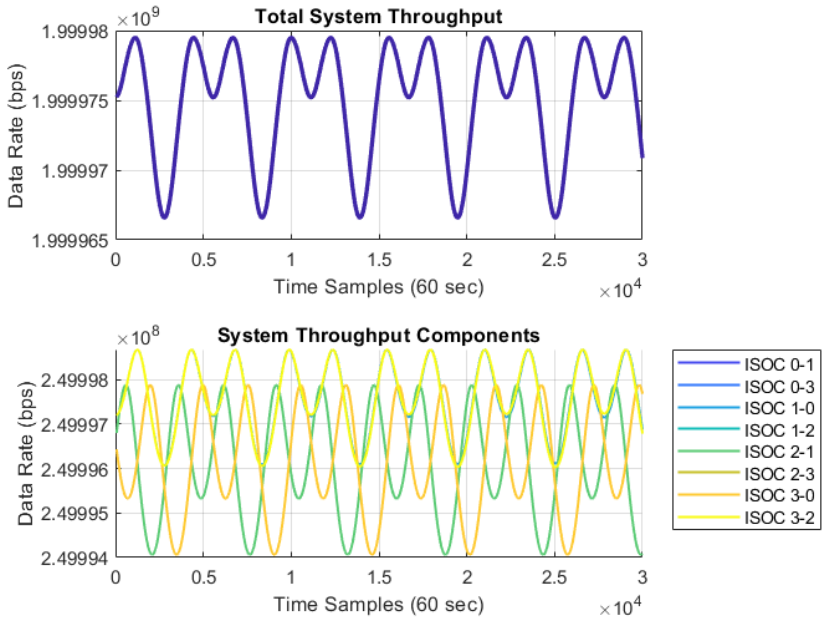

Figure 26: System Throughput for TDMA Relay in LEO. Differences in range lead to variations in data rate.

The system delay is shown in Figures 28-29. Like the capacity figures, individual delay is shown first followed by system-level performance. ISOC, even with access delay components, is dominated by the allocated alignment delay set to a constant 3 seconds. The alignment method for ISOC has not been defined. ISOC AoA could be used to assist or acquire links, however, the time it takes for the control system to converge is undefined [54]. Alignment delay would need to be on the order of milliseconds to impact the overall system-level delay.

The total round-trip time it takes to send a 50MB data payload through the network is ~6.4 seconds with the TDMA relay (blue axis, Figure 29). The majority of this time is spent in access delay wherein nodes are waiting for their turn to transmit. The right axis of Figure 29 captures the total time it takes for a single node to transmit the full data payload given the instantaneous capacity and is limited by link bandwidth.

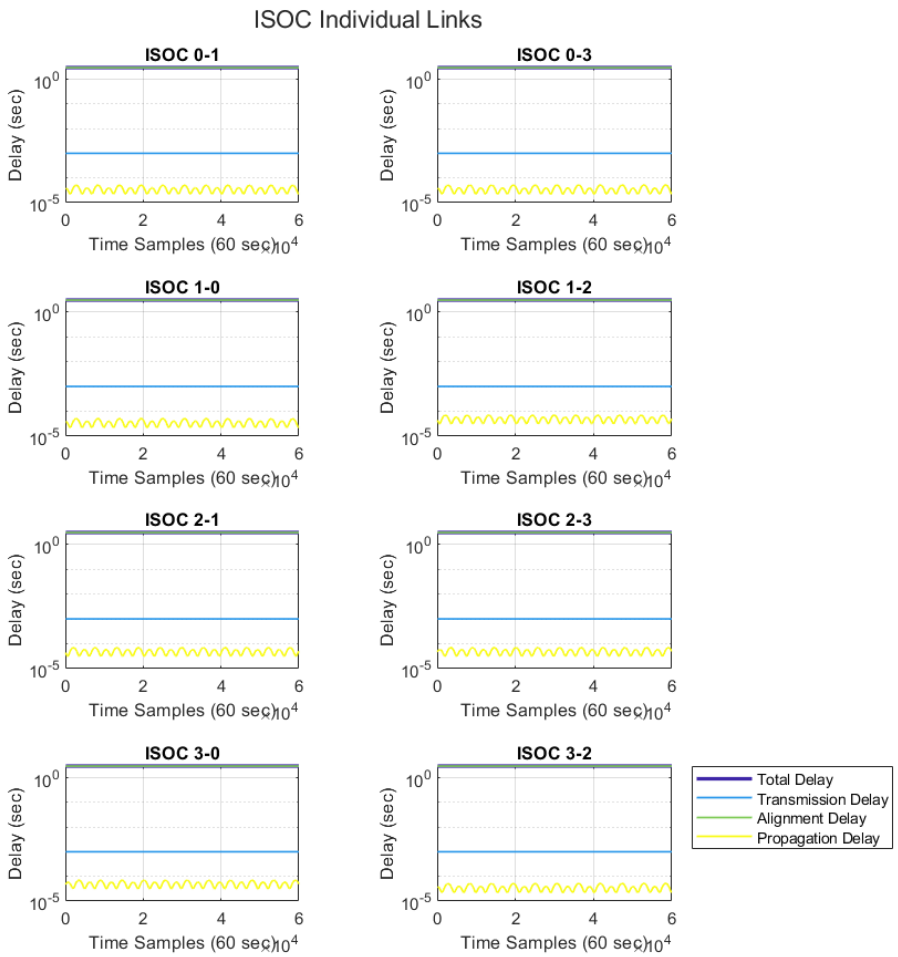

Figure 27: Individual Delay Components for TDMA Relay in LEO. Total delay and alignment delay are virtually equal and are plotted at the top of each graph, meaning total delay is dominated by alignment time.

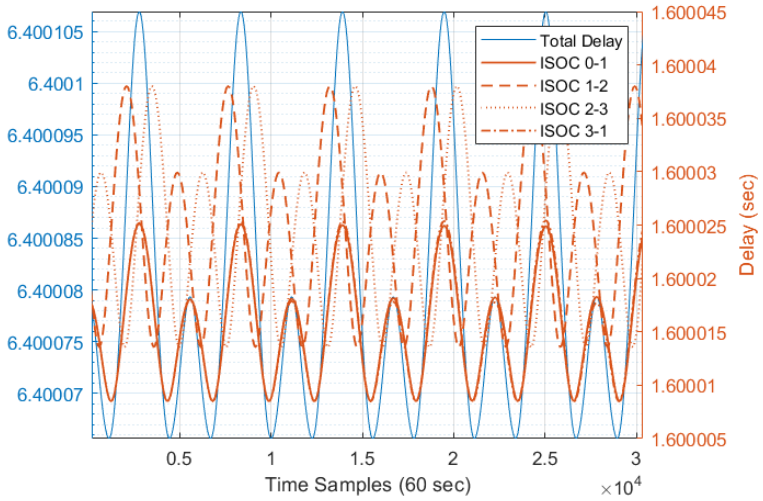

Figure 28: System Delay for TDMA Relay in LEO. Total delay is the roundtrip time through the network (left) and individual delay is the time it takes for each transmitter to send data to its receiver (right)

4.4.3.2 TDMA Mesh

Mesh assumes all nodes can connect with each other. The individual data rates vs. range remain the same, which is expected given the number of users is constant and the terminal architecture did not change. The system throughput increased to ~3 Gbps, which is expected as the number of links increased by a total of four, and each link supports 250 Mbps.

The individual delay results match the relay results as the model inputs are constant. The system-level delay also remains at 6.4 seconds, which intuitively follows as the number of links to form a closed-loop within the network remains constant. Note that in order to estimate a single round-trip instance, an underlying mesh algorithm is added to pick a combination of nodes to form a closed loop within the network. This choice is made by finding the minimum amount of time to get from ISOC 0 to all the nodes then back to ISOC 0. In actuality, this information will not be known to the satellites a priori unless equipped with a stellar orbit propagator or informed by operators on the ground.

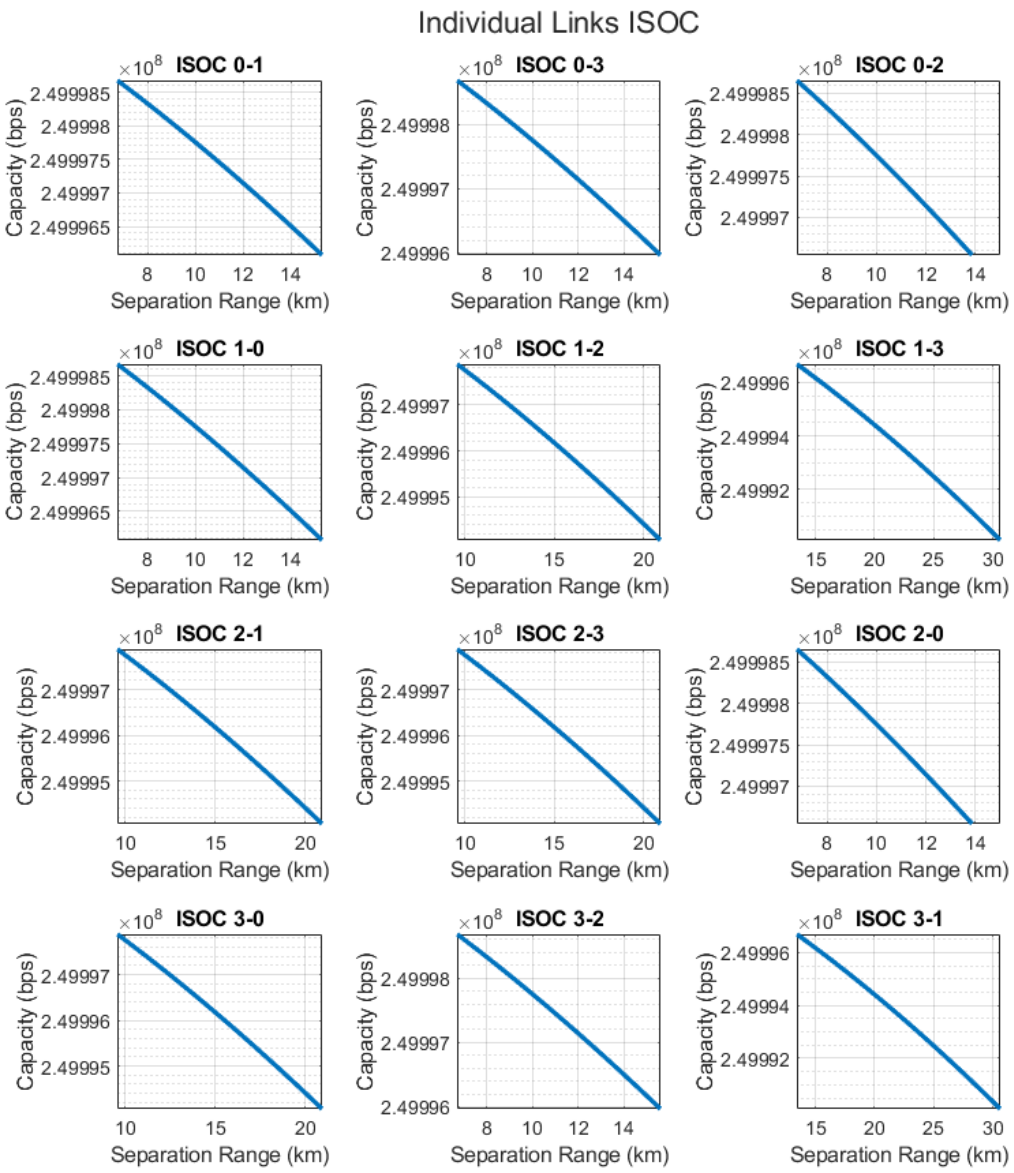

Figure 29: Individual Link Capacity vs. Range for TDMA Mesh in LEO. Mesh network supports additional links compared to the relay architecture.

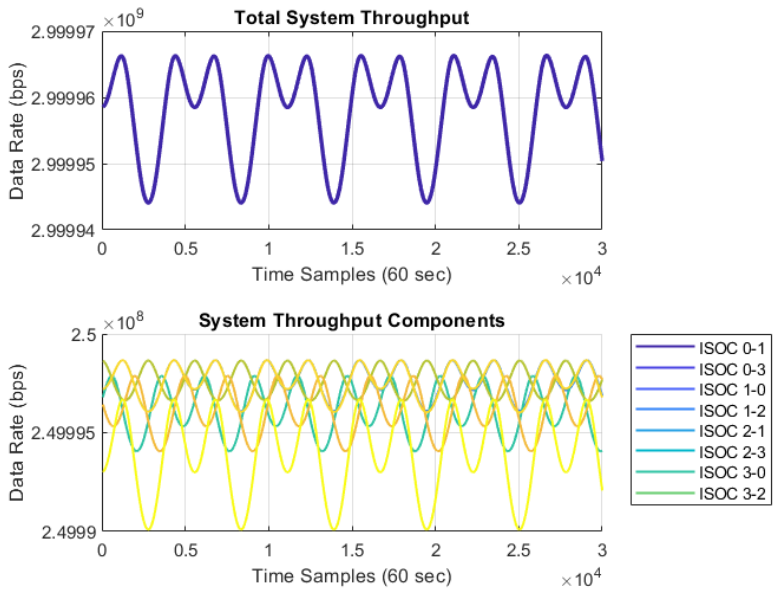

Figure 30: System Capacity for TDMA Mesh in LEO. Differences in link range result in different individual data rates between terminals.

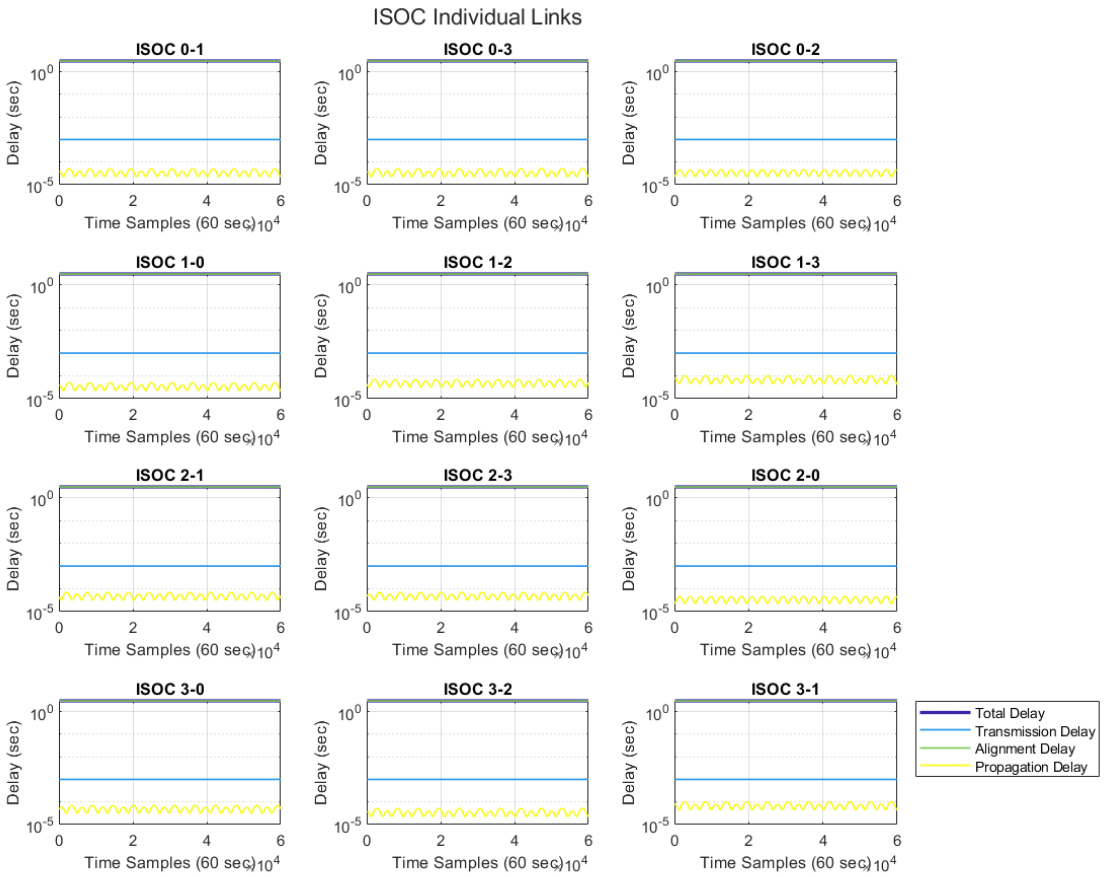

Figure 31: Individual Delay Components for TDMA Mesh in LEO. Like the relay case, total delay and alignment delay are virtually equal and are plotted at the top of each graph, meaning total delay is dominated by alignment time.

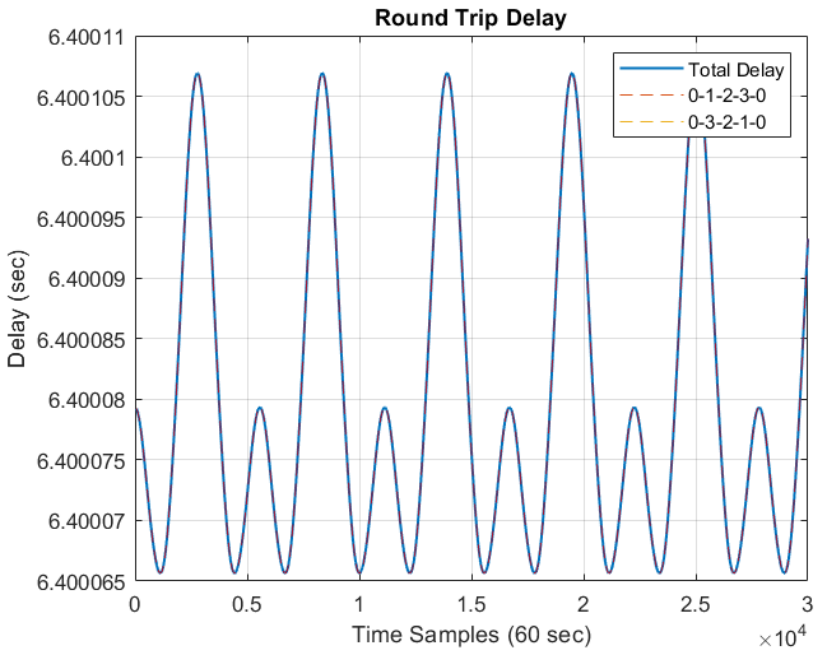

Figure 32: Round Trip Delay for TDMA LEO Mesh. The underlying mesh algorithm chooses a path with the highest link capacity (blue, Total Delay). Two manual path combinations were chosen to compare delay performance (dotted). There is no difference in performance between the two selected cases (plotted on top of each other), meaning the network can choose either path to achieve the same delay performance.

4.4.3.3. WDMA Relay

Adding multiple wavelengths for a WDMA system results in 4X higher individual link components for the relay system compared to the TDMA case. This follows the expectation that the individual link capacity will be reduced proportional to the inverse of the number of users. Similarly, the total system capacity is proportional to the number of users in the system. In this case, because each user can have up to two simultaneous links, the system capacity is a product of the number of links and number of users. This results in a system capacity of about 8 Gbps.

Like the TDMA scenarios, individual delay is nearly equal to the alignment delay. The transmission delay, however, or the time it takes to send 50 MB through the network, was reduced by a factor of 4 as users did not need to wait for a transmission interval. To send the full 50 MB packet takes 400 ms in the WDMA relay case and is limited by achievable data rate.

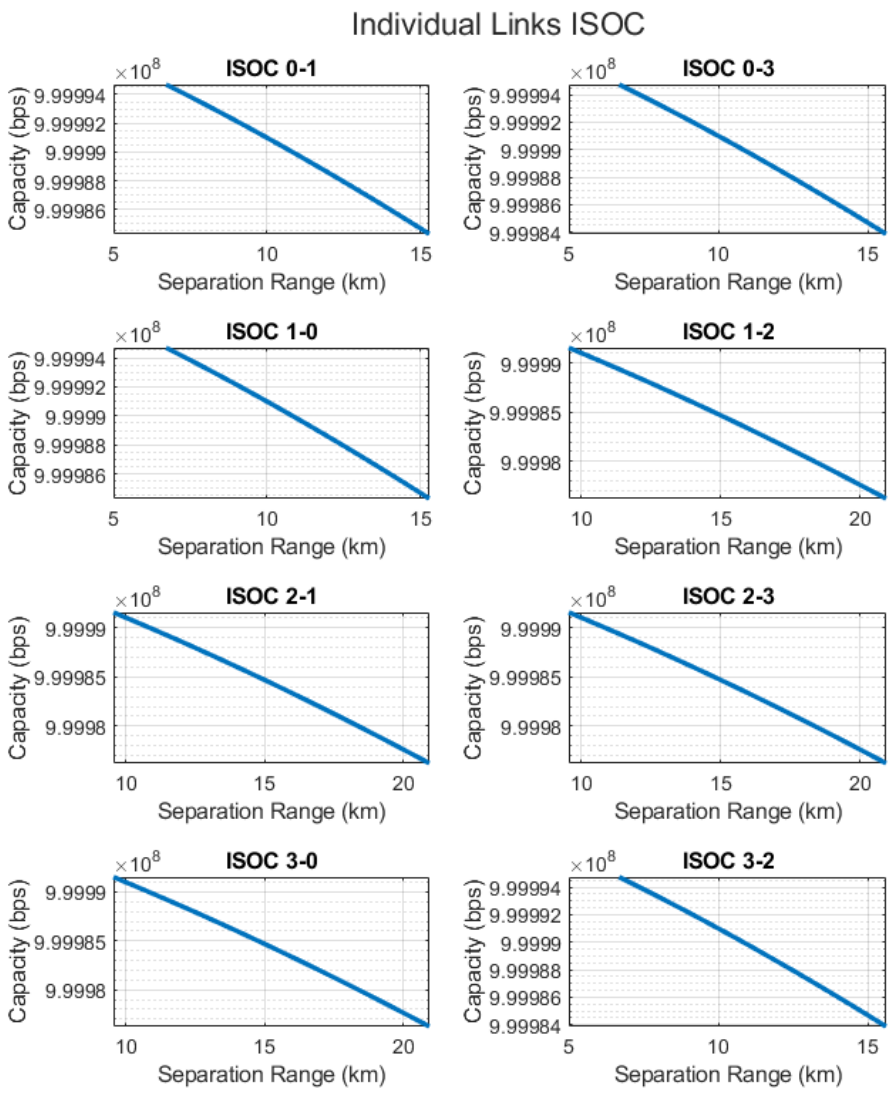

Figure 33: Individual Link Capacity vs. Range for WDMA Relay in LEO. Individual data rates for WDMA links are 4X higher compared to TDMA.

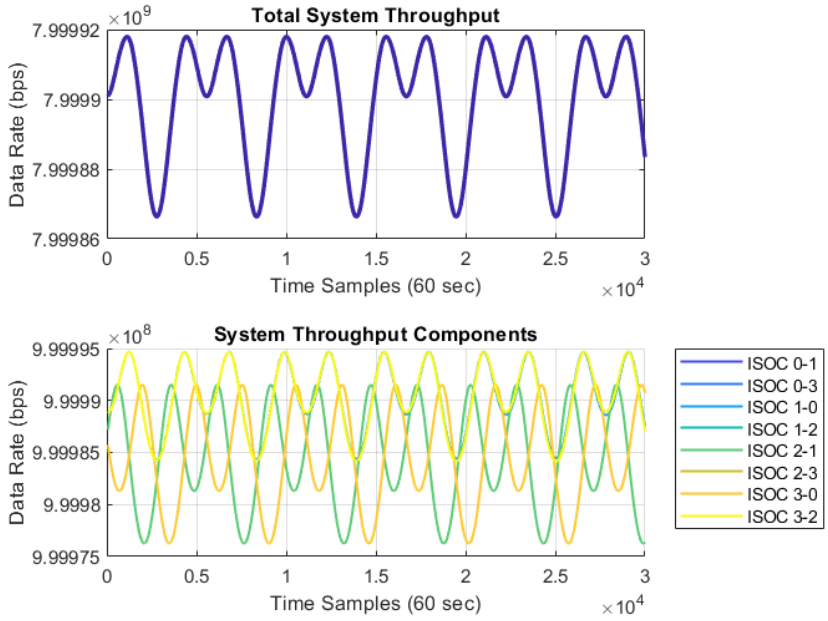

Figure 34: Total System Throughput for WDMA Relay in LEO.

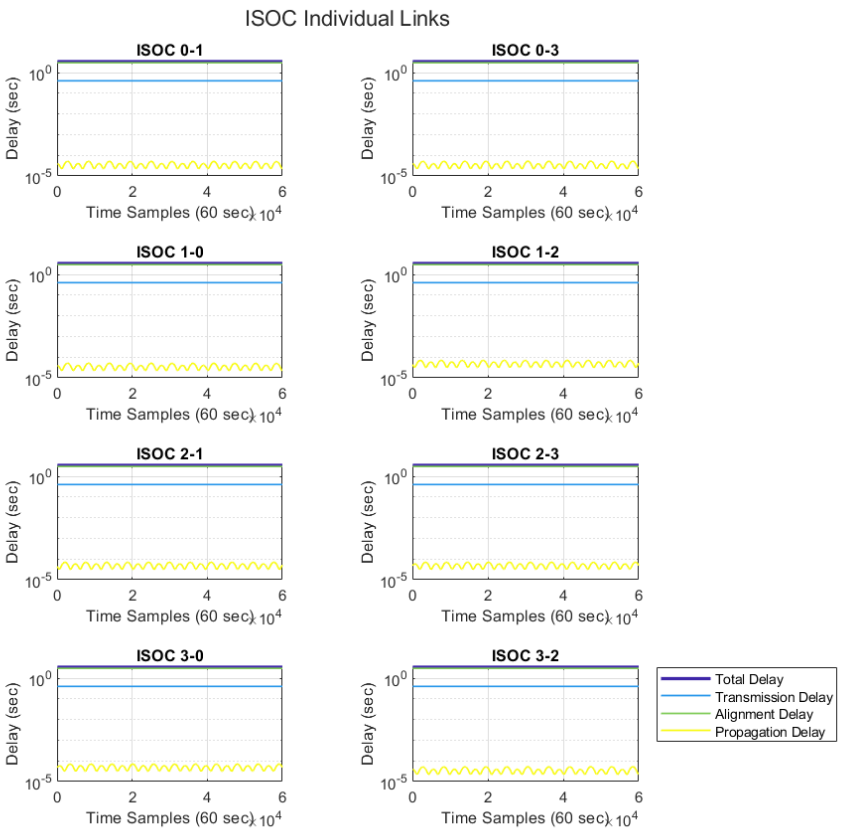

Figure 35: Individual Delay Components for WDMA Relay in LEO. Total delay is dominated by alignment delay.

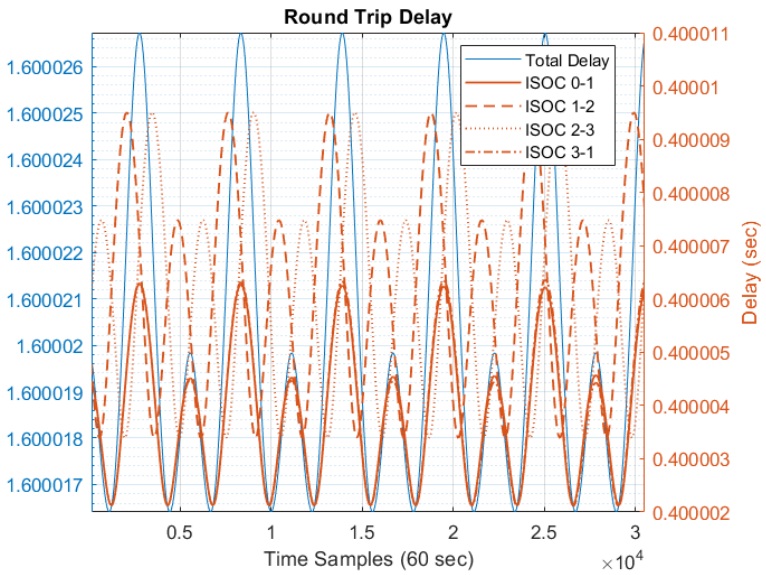

Figure 36: Round Trip Delay for WDMA Relay in LEO. Individual delay is reduced compared to TDMA as users do not need to wait for an allocated time slot.

4.4.3.4 WDMA Mesh

Individual link performance is unchanged for the WDMA mesh case. The system throughput behaves like the WDMA relay case, and is a product of the number of users, number of supported links, and capacity of each link. Compared to TDMA relay and mesh and WDMA relay, WDMA mesh has the highest system throughput at 12 Gbps. The delay is unchanged from the WDMA relay scenario. Table 18 summarizes the values for each scenario.

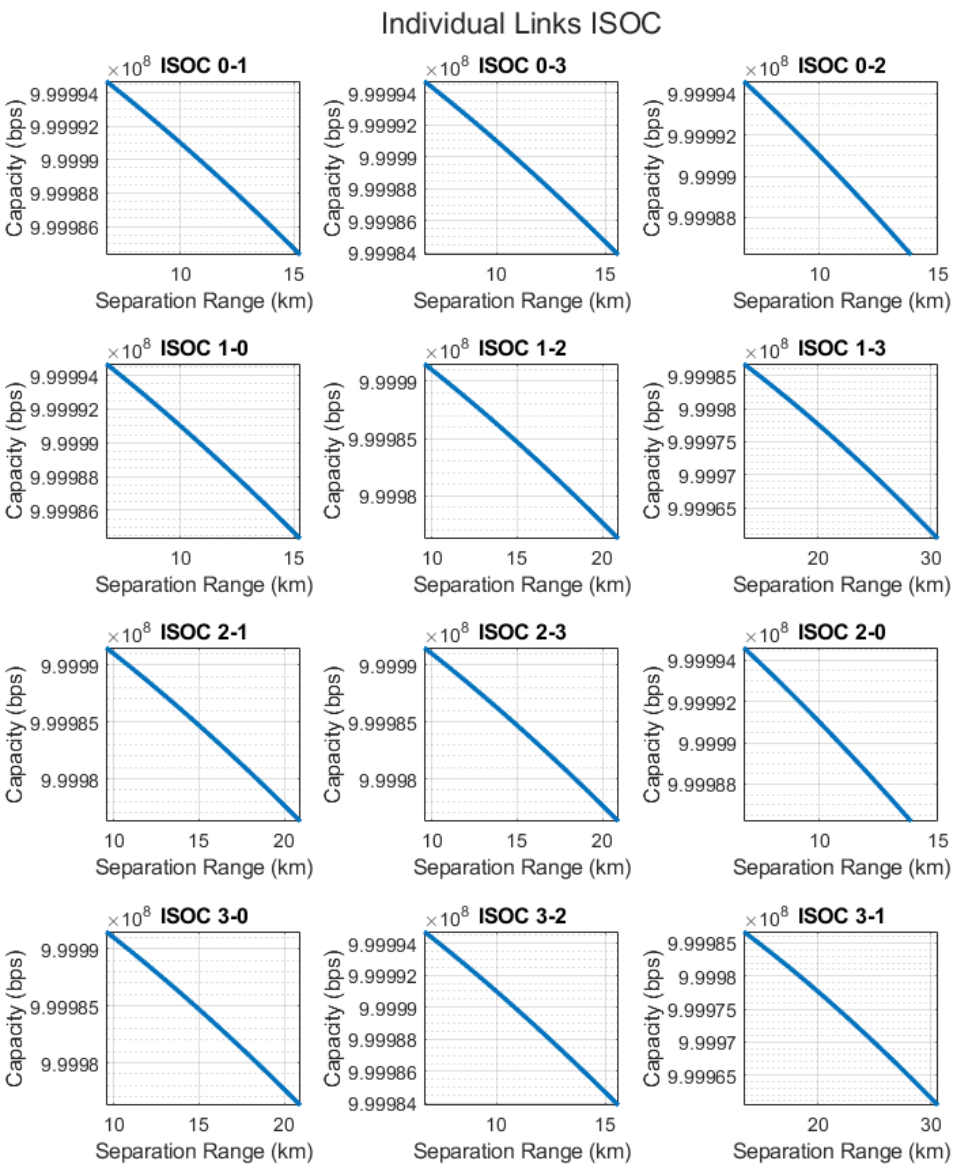

Figure 37: Individual Link Capacity vs. Range for WDMA Mesh in LEO

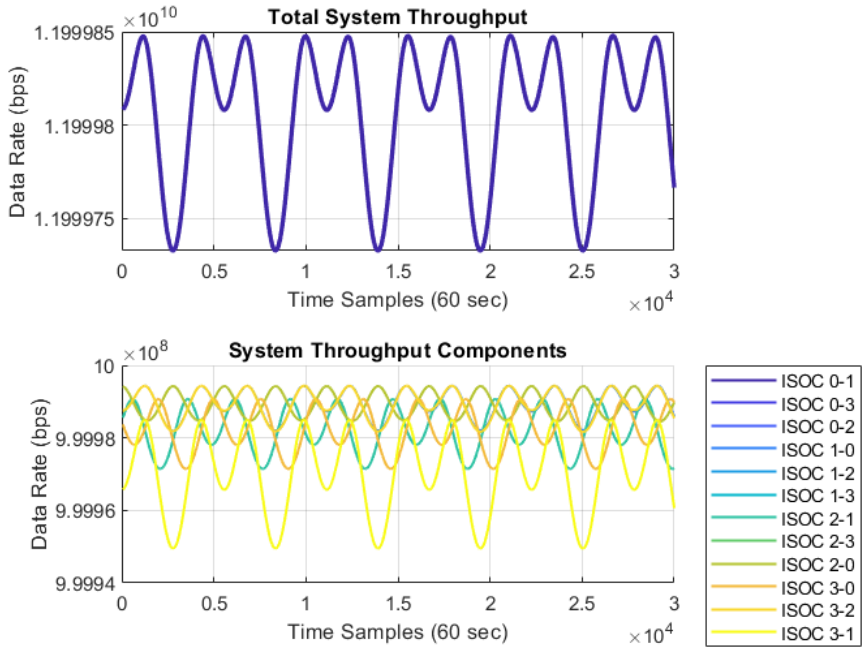

Figure 38: System Throughput for WDMA Mesh in LEO

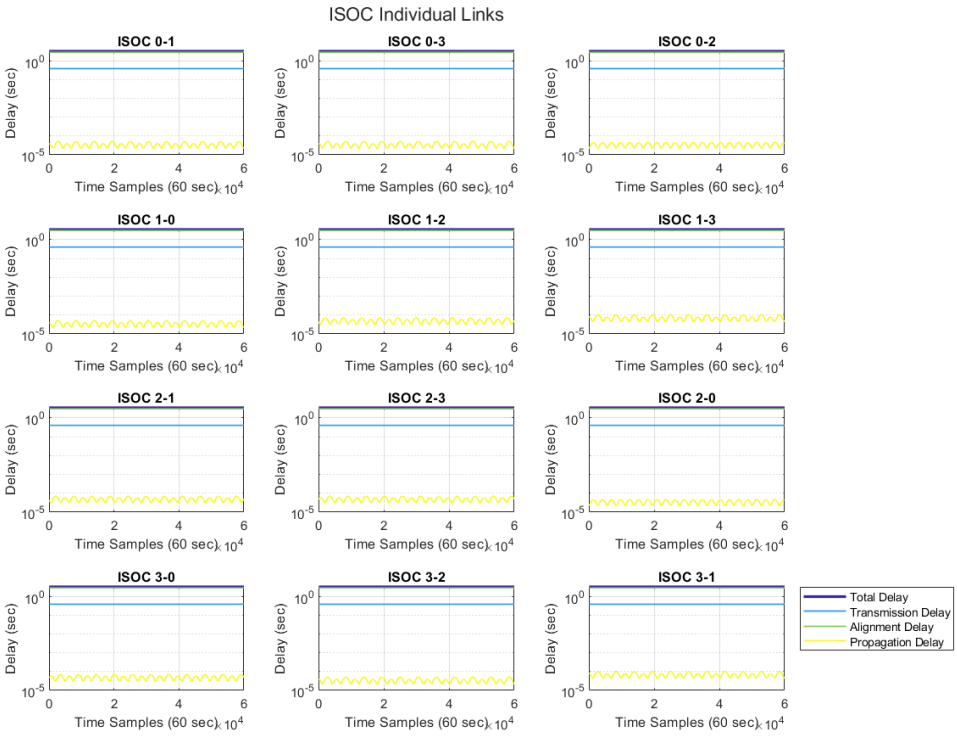

Figure 39: Individual Delay Components for WDMA Mesh in LEO

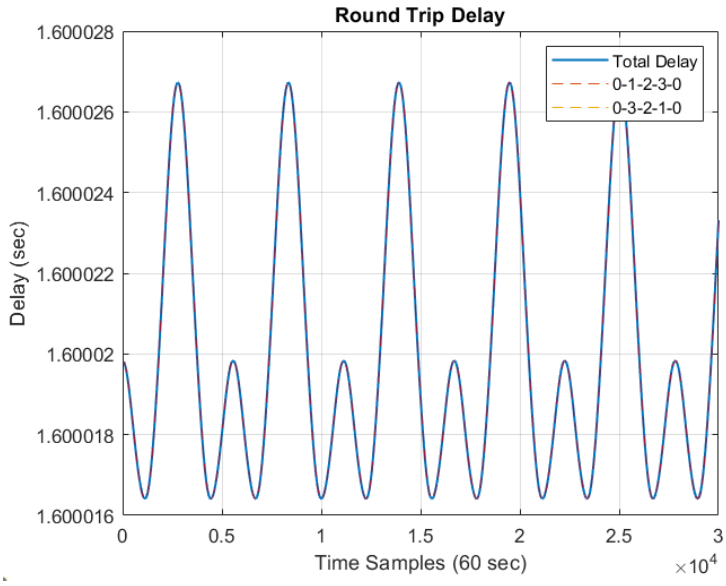

Figure 40: Round Trip Delay for WDMA Mesh in LEO. The underlying mesh algorithm chooses a path with the highest link capacity (blue, Total Delay). Two manual path combinations were chosen to compare delay performance (dotted). There is no difference in performance between the two selected cases (plotted on top of each other), meaning the network can choose either path to achieve the same delay performance.

4.4.3.5 WDMA vs TDMA

Figure 42 shows a direct comparison of the throughput and round-trip delay for all scenarios. The results appear flat as the variations for each output are much smaller than their mean values (kbps vs Mbps). TDMA relay and mesh and WDMA relay and mesh delay are equal and are difficult to discern from the graph alone. WDMA mesh supports the highest system capacity at 12 Gbps and ties for lowest total delay at 1.6 sec. As shown in the TDMA vs WDMA trades, WDMA is difficult to outperform with TDMA alone.

Table 18: Summary of Results from the LEO Swarm Case Across Network Configurations and Access Method

	TDMA		WDMA	
	Relay	Mesh	Relay	Mesh
Max Delay (sec)	6.40	6.40	1.60	1.60
Min Delay (sec)	6.40	6.40	1.60	1.60

Average Delay (sec)	6.40	6.40	1.60	1.60
Max Data Rate (Mbps)	2000.00	3000.00	7990.00	12000.00
Min Data Rate (Mbps)	2000.00	3000.00	7990.00	12000.00
Average Data Rate (Mbps)	2000.00	3000.00	7990.00	12000.00

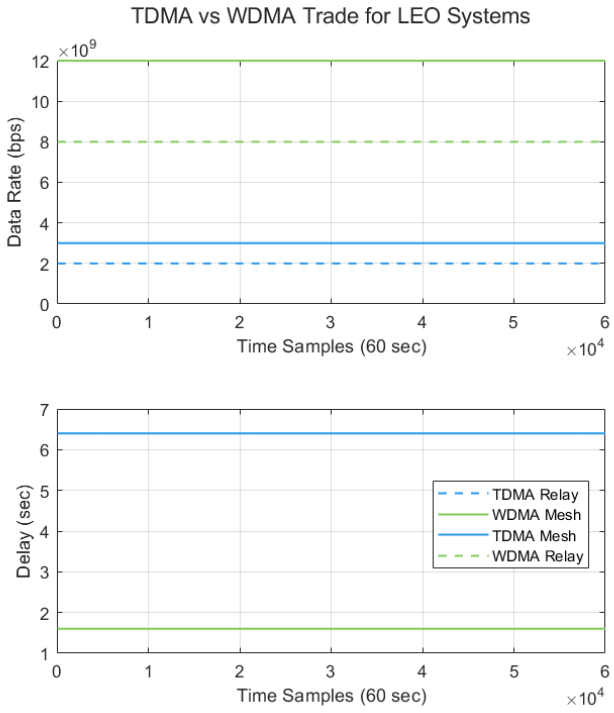

Figure 41: Access Method and Network Configuration Comparison for LEO Applications. Individual link capacity is bandwidth limited and the range between individual users is relatively constant, which results in a seemingly constant system capacity and total delay.

4.4.3.6 PICs vs Fiber

We also consider the performance trade between PICs vs fiber for LEO terminals. The WDMA mesh case was chosen to compare the two technologies. PICs must offer a competitive advantage for wide-spread adoption, and thus is compared to the current highest-performing fiber system. Figure 43 shows overlayed system throughputs.

Despite the additional bandwidth requirements for PICs due radiation-induced shifts, the overall system throughput is comparable to the fiber-based system. The difference between average throughput is 26.74 kbps, which is orders of magnitude lower than their operational data rate. The predicted mass for the PIC and fiber terminal are 1.77 kg and 4.55 kg, respectively. The corresponding mass efficiency for the PIC is 6.8×10^3 Mbps/kg, and the fiber is 2.6×10^3 Mbps/kg. Although the PIC-based system has a lower throughput overall, the 20 kbps is marginal compared to the SWaP savings (captured by mass efficiency) that is offered by PICs.

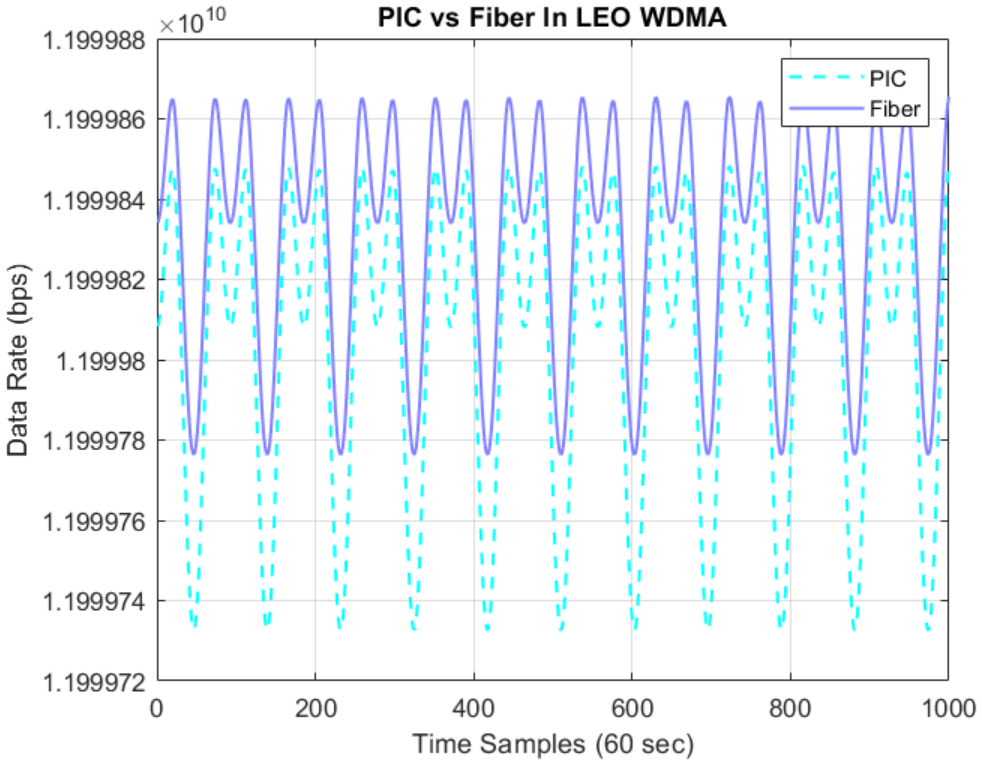

Figure 42: PICs vs Fiber for LEO Systems. Variations in data rate are caused by varying range between users.

This approach comes with many challenges and caveats, one being how to build a free-space coupled PIC transceiver with high optical throughput. The beam quality, sometimes known as the M^2 factor, is a quantitative measure of how gaussian a beam is. High-power PICs use large active areas to effectively increase the power at which the material saturates to achieve > 100-mW outputs. A side-effect of this approach is creating spatial modes that result in non-Gaussian beams, or beams with poor M^2 factors. PIC outputs coupled to free-space tend to have large divergences,

similar to bare fiber. Poor beam quality and large divergences impact the overall link budget in ways that are not captured in this analysis but may be prohibitive in the proposed terminal architecture.

A potential solution could be to develop a terminal analogous to Spatial Combining Power Amplifiers (SPCAs) and Monolithic Millimeter wave Integrated Circuits (MMICs) [163]. Instead of scaling power on chip, the output signals from an array of PICs could be coupled into a free-space resonator cavity where they accumulate power proportional to the number of transmitters in the array. Using four, 250-mW transmitters could prove to be a novel and viable temporary solution until photonics reach a scalable solution. Synchronization will be key, and minimizing reflections with the cavity is crucial to retain timing characteristics needed for PPM. The definition and design of such a terminal is out of the scope of this thesis, but spatial power combining at optical frequencies have been proven robust, especially for mitigating atmospheric turbulence [97], [148].

Despite the low TRL and additional risk factors, the added benefit of a PIC-based terminal in a WDMA mesh architecture is substantial. A factor of 2.62X improvement to mass efficiency may be gained. LEO missions, especially in Cubesat platforms, offer opportunities to test and raise the TRL of modest output power terminals (~1 W) with a relatively low number of users. Given the use case and the performance metrics, a WDMA mesh architecture with a PIC transceiver is recommended for a LEO scenario.

4.5 Deep Space Network

4.5.1 Mission Configuration

For the deep-space scenario, an interplanetary relay between Mars and Earth was simulated with spacecraft positioned at Earth, Mars, Sun-Earth Lagrange 4 (L4) and 5 (L5) points and Sun-Mars L4 and L5. Also known as libration points, Lagrange points are areas where the gravitation forces between massive bodies reach equilibrium. L4 and L5 are positioned 60° from the midline bisecting the two massive bodies, with L4 leading (+60°) and L5 lagging (-60°). L4 and L5 points were chosen over L1, L2, and L3 due to increased orbital stability [164].

Other analyses have proposed positioning spacecraft at L1 or L2 points of other bodies, such as Sun-Jupiter [165], because of the proximity to the planetary body and lack of naturally-occurring satellites. Due to the gravity gradient surrounding the L4 and L5, these points can attract

and capture asteroids, which are also known as Trojans. Despite the additional collision risk, L4 and L5 orbital stability translates to less station-keeping requirements over the mission life.

Planetary trajectory data is generated for Earth, Mars, and Lagrange points using JPL's Horizons tool [166]. Using a heliocentric frame of reference, ephemeris data is generated for the planetary bodies from January 01, 2022 through January 1, 2027. The Lagrange positions for each body are then estimated by applying a 60° rotation matrix [164].

Solar conjunction, a period when Mars and Earth are obscured from view and communications due to solar interference, prevents continuous coverage and 100% availability between the planets. Depending on the level of solar activity, this translates to keep-out angles < 2.3° between the Sun-Earth-Probe (SEP) [167].

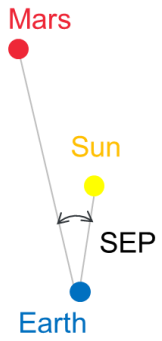

Figure 43: Simplified diagram of a Sun-Earth-Probe geometry. Mars is depicted as the probe.

Optical communication links require additional angular separation margin to maintain communications (~12° [140]) due to the ground receiver sensitivity to background light as well as operational constraints (e.g., thermal management for the primary aperture). Figure 44 shows the Sun-Earth-Mars (SEM), Sun-Mars-Earth (SME), and Earth-Sun-Mars (ESM) angles for a five-year period with a January 1, 2022 epoch. The solar conjunction angle is marked to identify blackout periods between Earth and Mars.

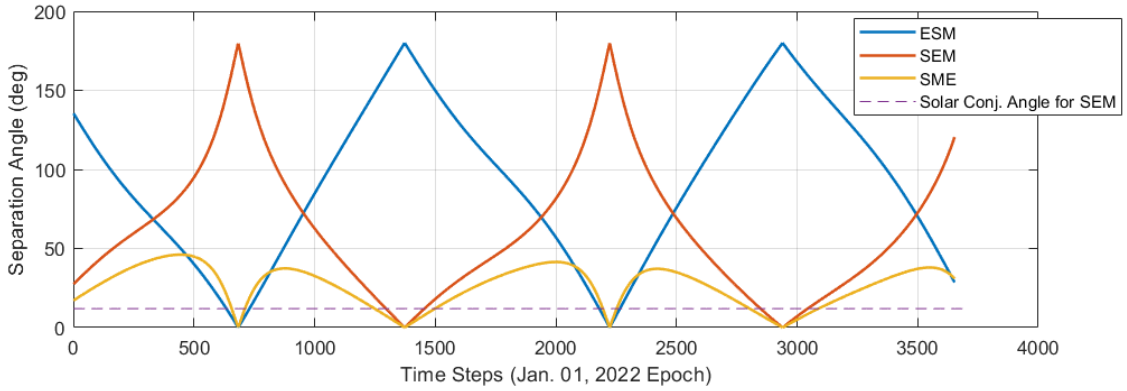

Figure 44: Earth Sun Mars (ESM), Sun Earth Mars (SEM), and Sun Mars Earth (SME) Angles vs. Time

This analysis assumes the cutoff angle extends to all users within the network and < 12° SEP and SPE angles are considered blackout periods. The Earth-Sun-Mars angle captures this information with a single curve and is used in subsequent figures to depict solar conjunctions. Note that as shown in [140], 100% link availability is not possible with an Earth-Mars link alone.

Positioning spacecraft at Sun-Mars and Sun-Earth L4 and L5 points can enable 100% availability. Figure 45 shows the proposed network configuration and Figure 46 shows the relative angles between each point with labeled keep-out angles.

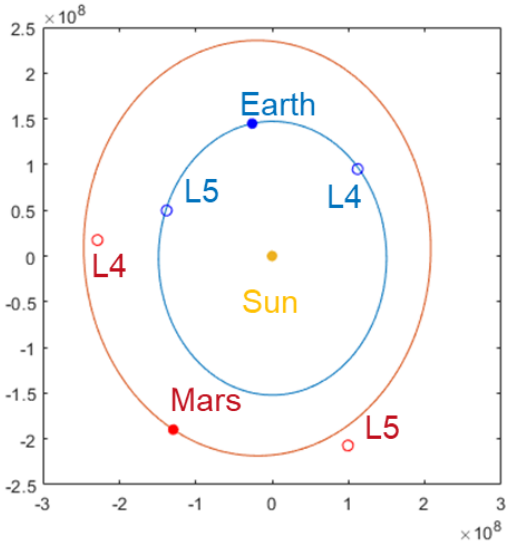

Figure 45: Deep-space network configuration between Mars and Earth using L4 and L5 points from each planet.

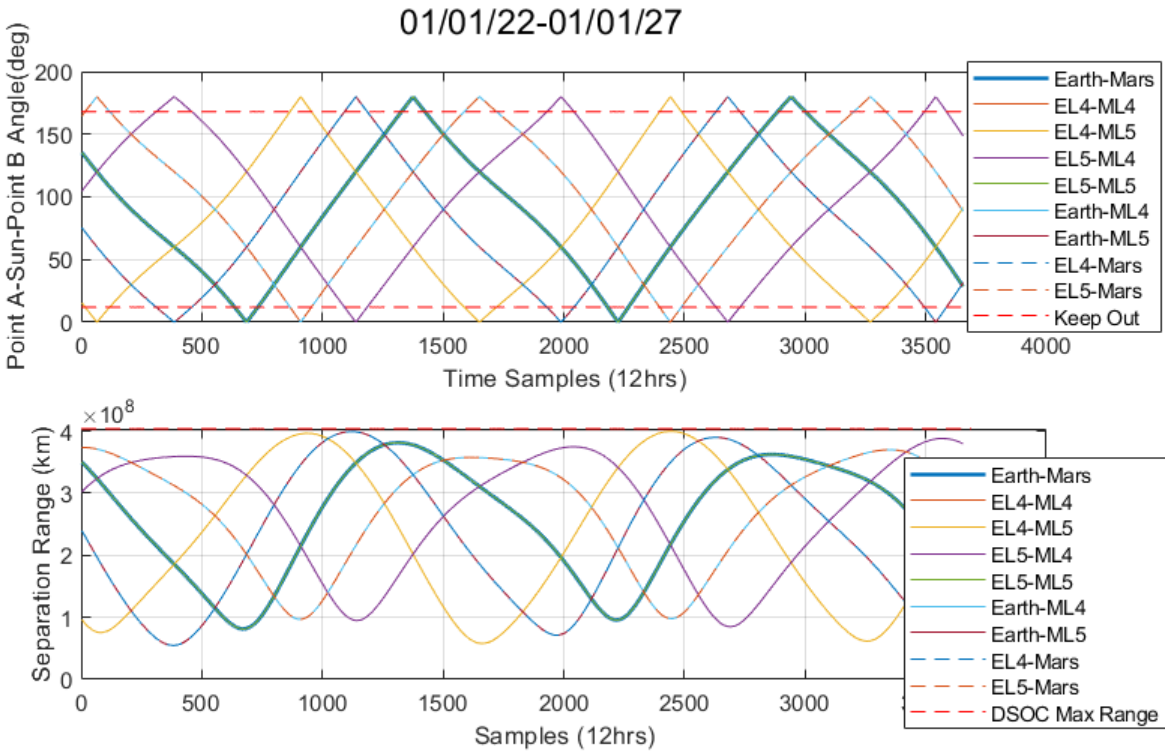

Figure 46: Relative Angles Between Deep Space Network Nodes with Keep Out Angles. EL4-Mars overlaps with Earth-ML4 and EL4-Mars with Earth ML5.

Continuous coverage can be achieved through several combinations of nodes. If all nodes have access to one another, constant coverage is easily achieved, with additional links that may act as contingency links in the event of a node outage. A subset of connections could also achieve continuous coverage. Using Earth-Mars, Earth L4-Mars L5, Earth L5-Mars L5, Earth- Earth-L4 and Earth L5, and Mars-Mars L4 and Mars L5, the angle between nodes at any given time does not exceed 12°.

4.5.2 Link Analysis

The reference terminal architecture used for the deep-space case builds on the incremental improvements to the current DSOC state-of-the-art proposed by [66]. Biswas identifies key improvements required to increase data rates from deep space, which include increasing the space and ground aperture sizes and increasing the transmitter output power. For the deep space scenario in this work, a 50-cm aperture diameter and 20-W transmitter are used for the space platform, and an 8-m ground station is assumed. The space-based receiver is a photon counting

detector using an SNSPD-TDC is used, however, the dark current value is set to 10^3 times higher than the Earth-based receiver due to lack of cryogenic cooling on the spacecraft [145]. Propagation delay, access delay (if applicable), alignment delay, and transmission delay are accounted for in the system delay calculation. It is assumed alignment delay is 2.5X propagation delay to allow for signal round-trips and to close the pointing loop between terminals.

Table 19: Deep Space Terminal Parameters [66], [123], [145], [147]

	Space	Ground	Units
BER	1.00E+09		-
PPM	16		-
Pointing Loss	-1.17		dB
Access Delay	60		sec
Alignment Delay	2.5X Propagation		sec
Transmitter Parameters			
Output Power	20		W
1/e2 Beamwidth	8		urad
Transmitter Losses	-1		dB
Receiver Parameters			
Primary Aperture Diameter	5.00E-01	8	m
FOV	50	80	urad
Receiver Losses	-1.54		dB
Sensor Efficiency	70%		-
Dark Noise	1.00E+07	1.00E+04	counts
BW	1.00E+09	1.00E+09	Hz

Results for TDMA are presented first in Sections 4.5.2.1-2. First, the DSOC relay case is presented. Mars is connected to its Lagrange points as well as directly to Earth when not in solar conjunction. The latter is included as representative of current deep space architecture, such as the MRO-DSN link [141]. ML4 is connected to EL5, ML5 is connected to EL4, and Earth is connected to its Lagrange points as well as Mars. All links are bidirectional but not symmetric as it is assumed Earth uses a larger aperture for receiving.

4.5.2.1 TDMA Relay

The capacity between each node pair is shown in Figure 47 as a function of capacity vs. range. The highest data rates can be seen between any node and Earth due to the increased receiver aperture size. The data rate is lowest between space-based nodes due to smaller receiver apertures.

The total data throughput over the simulated period is shown in Figure 48. Gray areas representing solar conjunctions are shown together with the data rate curves to provide context to the sharp changes in data rate. Only four curves, representing the connection between the Lagrange points and their respective planet, show insensitivity to solar-induced outage periods and maintain constant coverage within the network. On average, this configuration maintains an average of 42.26 Mbps total system throughput. Table 20 summarizes both the throughput and delay for all scenarios.

Sharp transitions in the data rate and delay can be seen across all scenarios due to solar conjunction. These are especially prominent when the Earth-Mars link cannot be established. Continuous, uninterrupted links are provided between the Lagrange points and their respective planet.

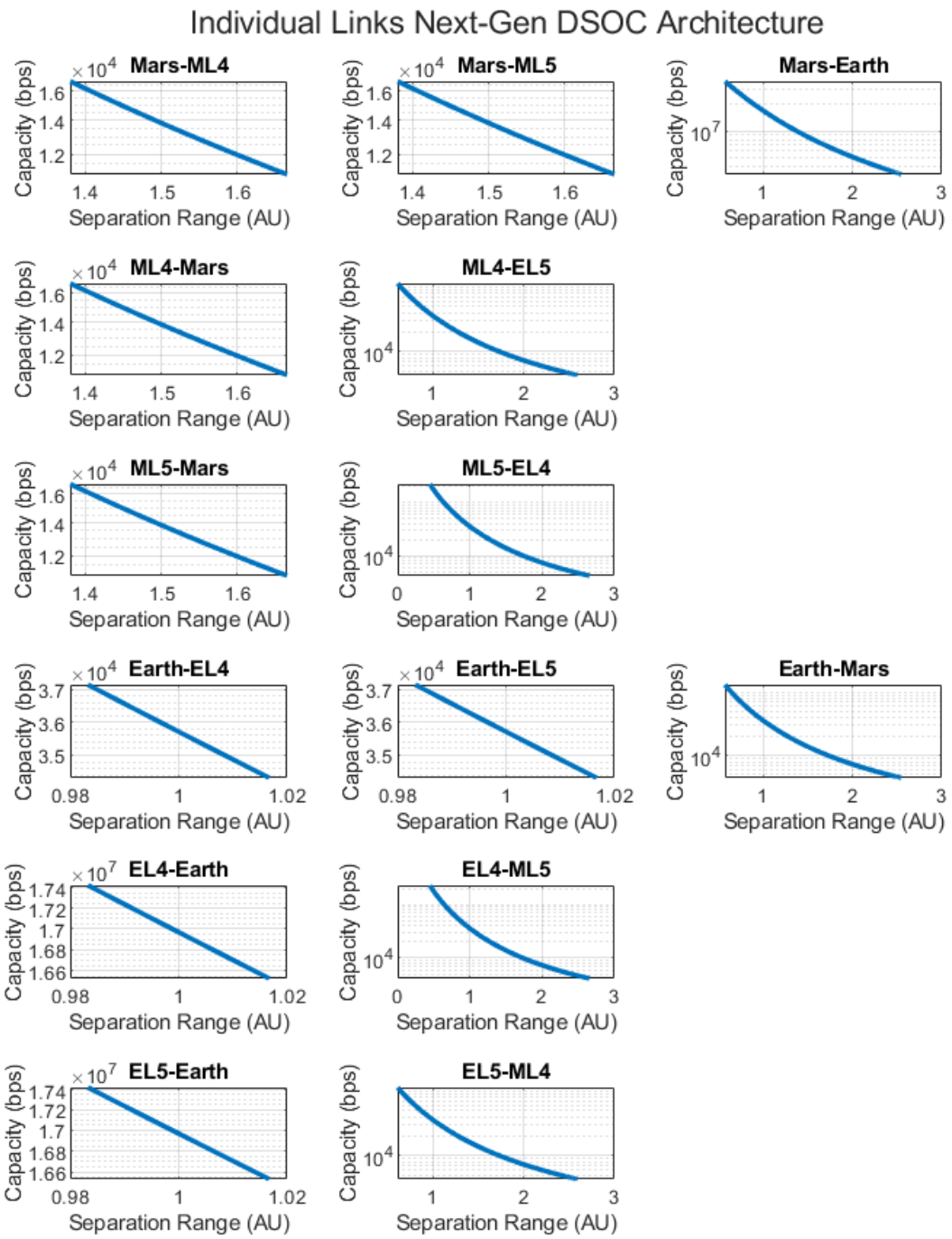

Figure 47: Individual Link Capacity vs. Range for TDMA Relay in Deep Space. Earth links support higher capacity due to the 8-m Earth receiver.

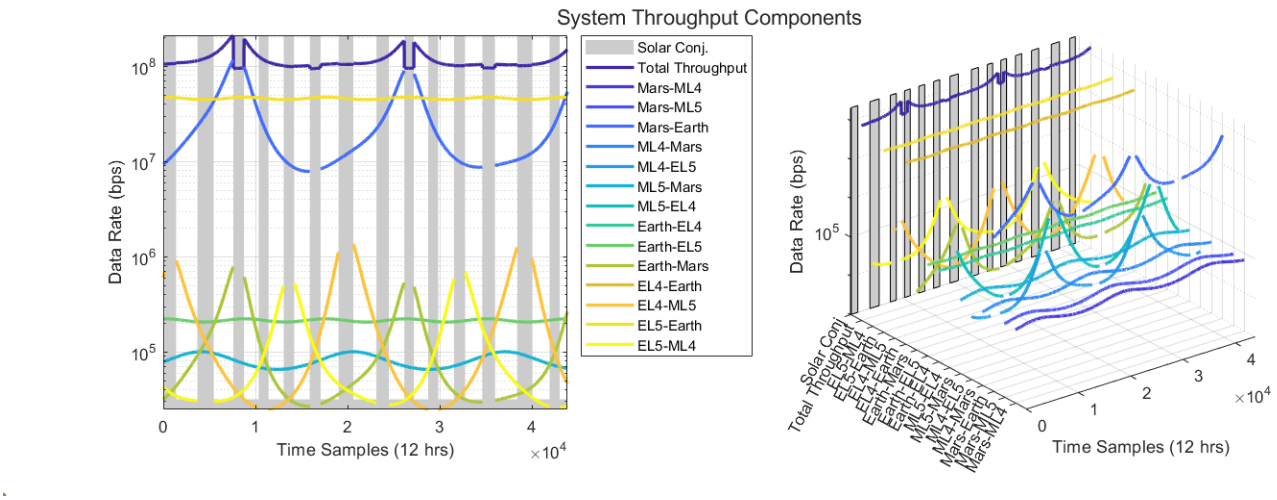

Figure 48: System Throughput for TDMA Relay in Deep Space. Solar conjunction periods are marked in grey.

Delay components between each node within the network is shown in Figure 48. As expected from the transmission slot trade study in Section 4.2.2, the individual delay, or time it takes to get data from one node to the next, is **dominated by propagation delay** and alignment delay. The round-trip delay for the relay architecture looks at the path between Mars and Earth and back. While an Earth-Mars link is assumed in the relay configuration, the round-trip delay looks at only the path from Mars to Earth and back through other nodes (*i.e.*, Mars to ML4 to EL5 to Earth, etc). This delay is captured in Figure 50. On average, the round-trip delay is 7.34 hours. This is primarily driven by the low data rates between the Lagrange points in the network (*i.e.*, ML4-EL5 and ML5-EL4).

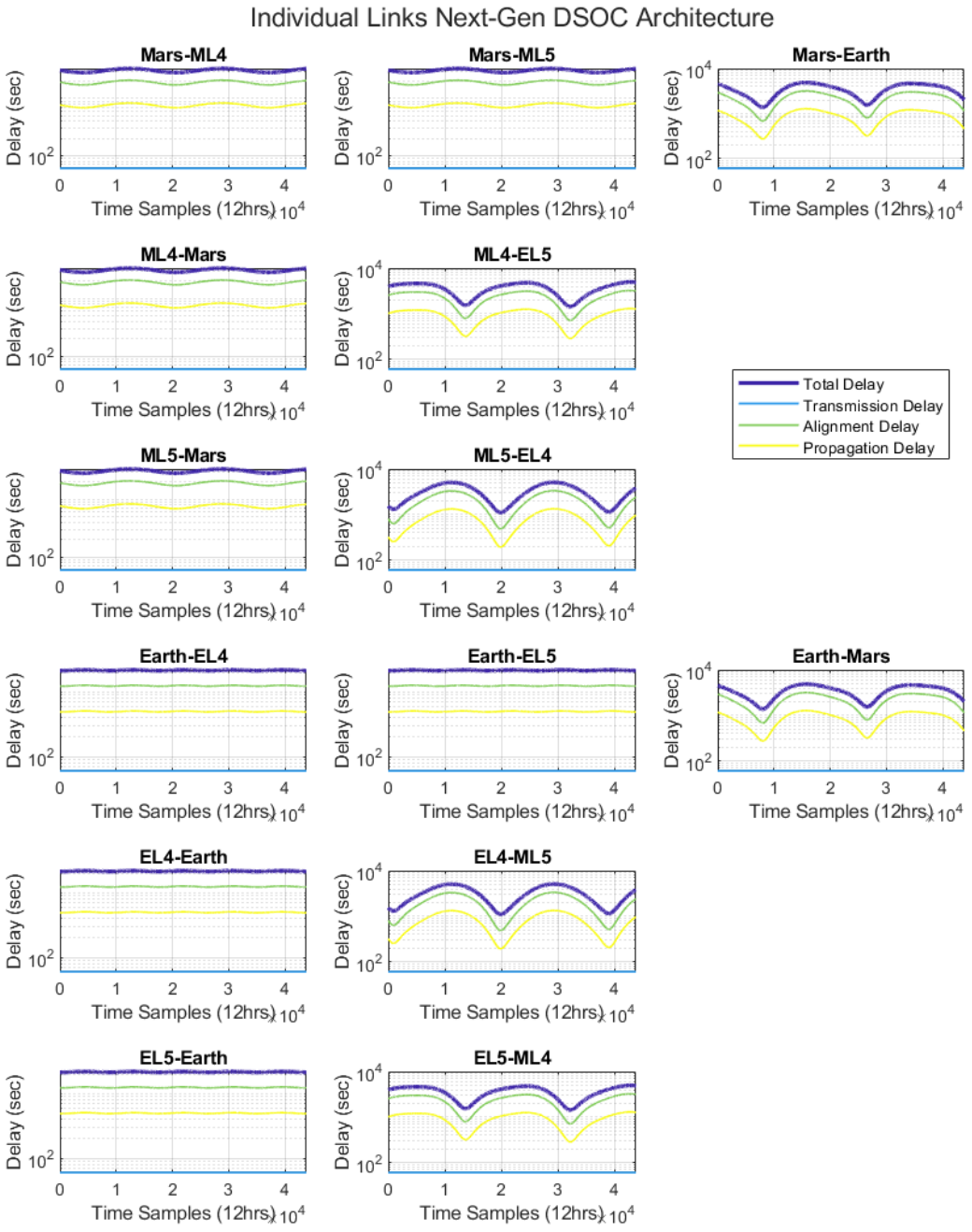

Figure 49: Individual Delay Components for TDMA Relay in Deep Space. Individual delay is dominated by propagation delay.

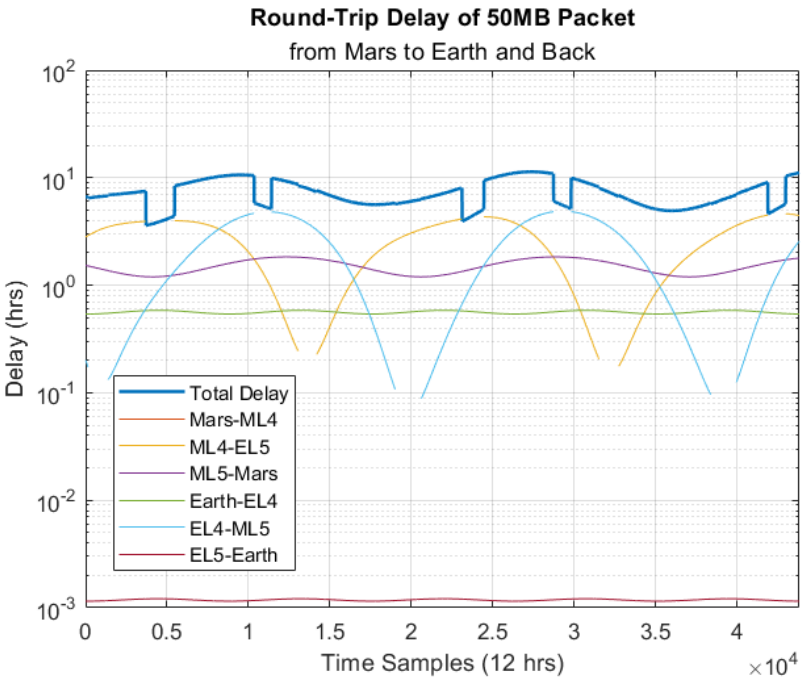

Figure 50: Round Trip Delay From Earth to Mars and Back Through the Relay Network. The sharp transitions are due to solar conjunction periods.

4.5.2.2 TDMA Mesh

Additional links are included for the mesh scenario assuming each node can support up to 3 links. The average system throughput is 59.75 Mbps and delay is 2.97 hrs. The increase in capacity compared to the TDMA relay is largely due to the additional nodes that can establish a direct link with Earth. Although Earth is further from neighboring nodes, the data rate is higher due to the increased aperture size.

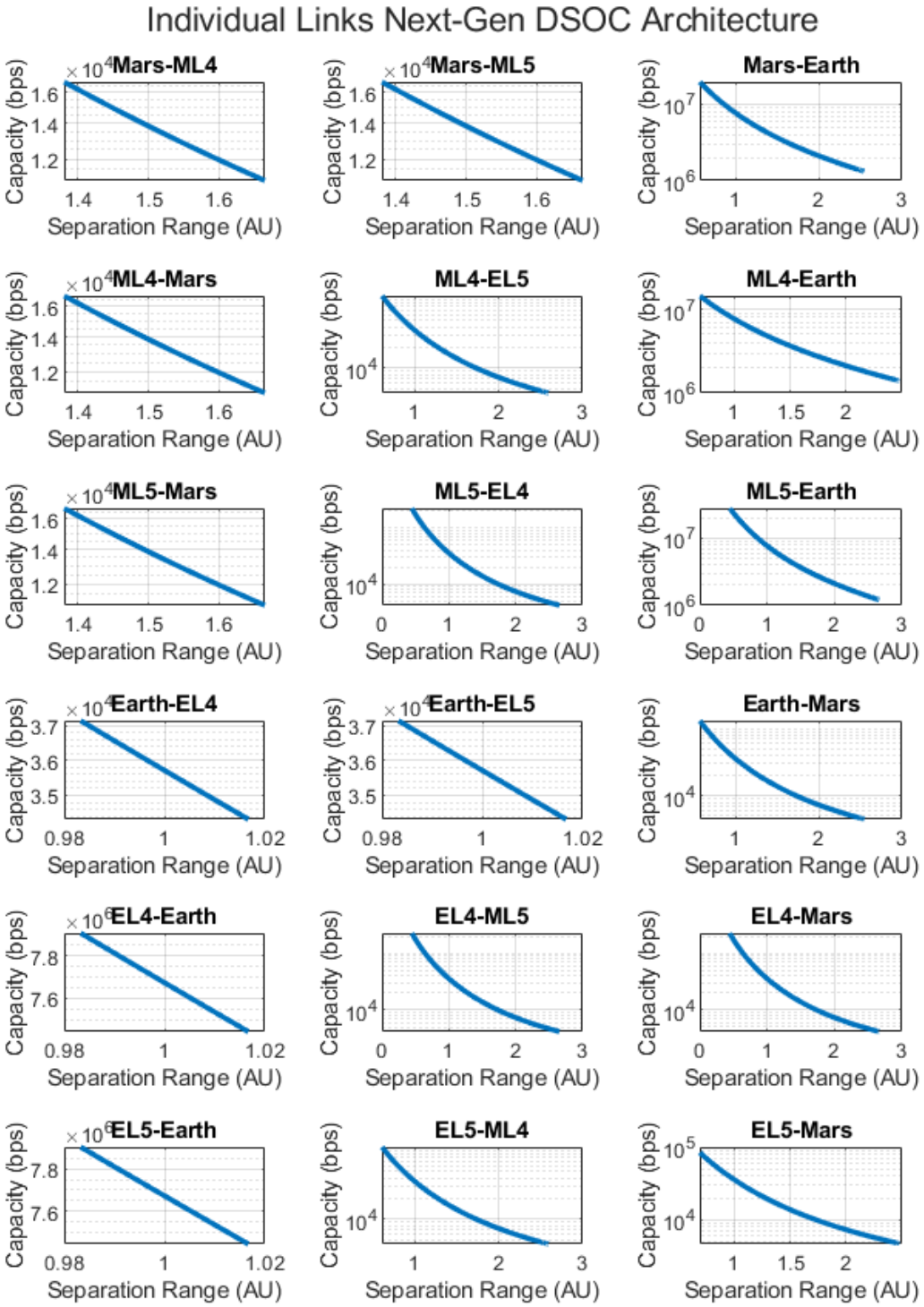

Figure 51: Individual Link Capacity vs. Range for TDMA Mesh in Deep Space

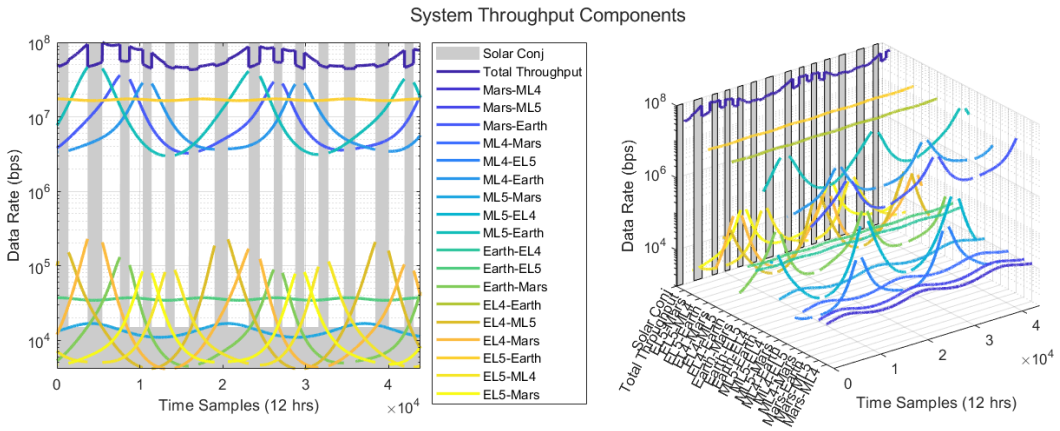

Figure 52: System Throughput for TDMA Mesh in Deep Space

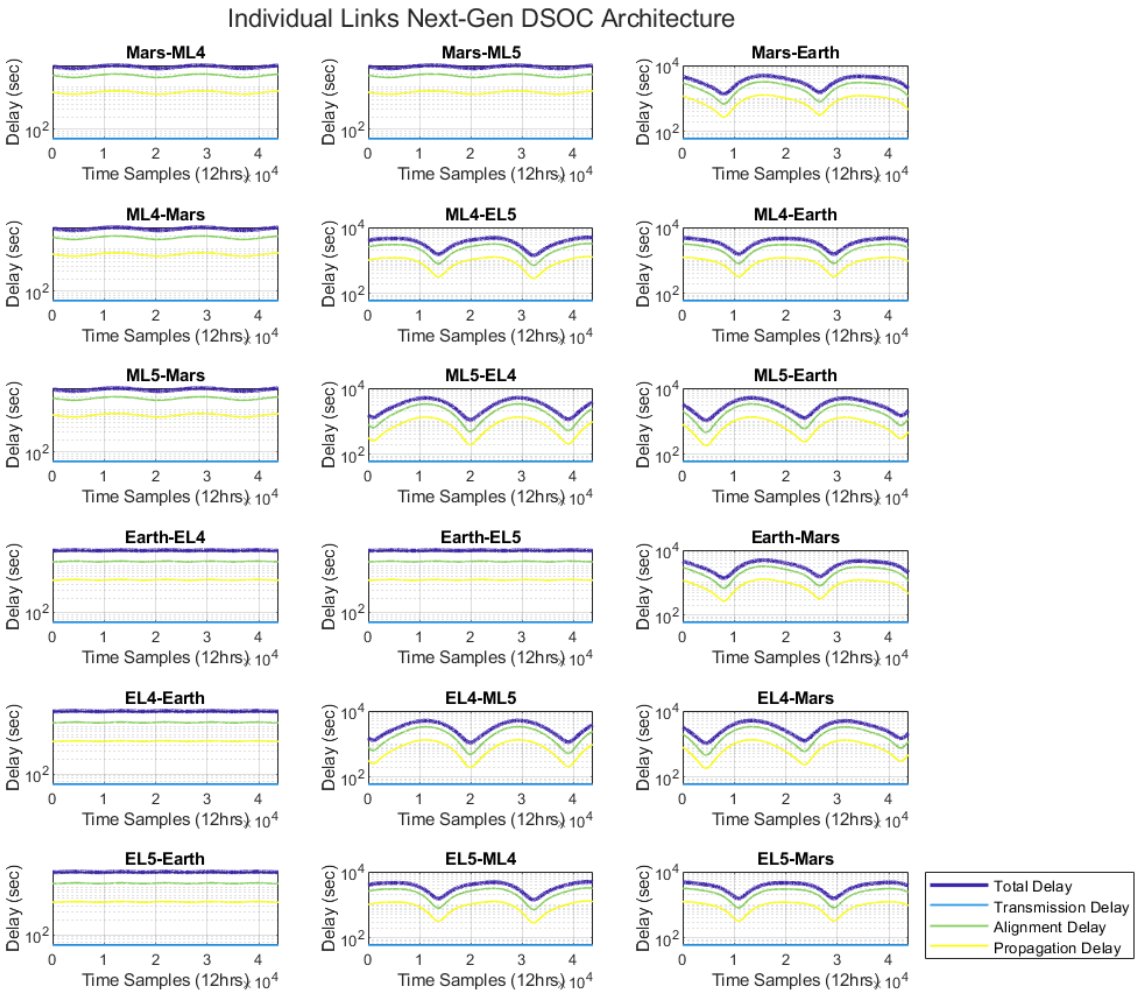

Figure 53: Individual Delay Components for TDMA Mesh in Deep Space. Individual delay is dominated by transmission delay.

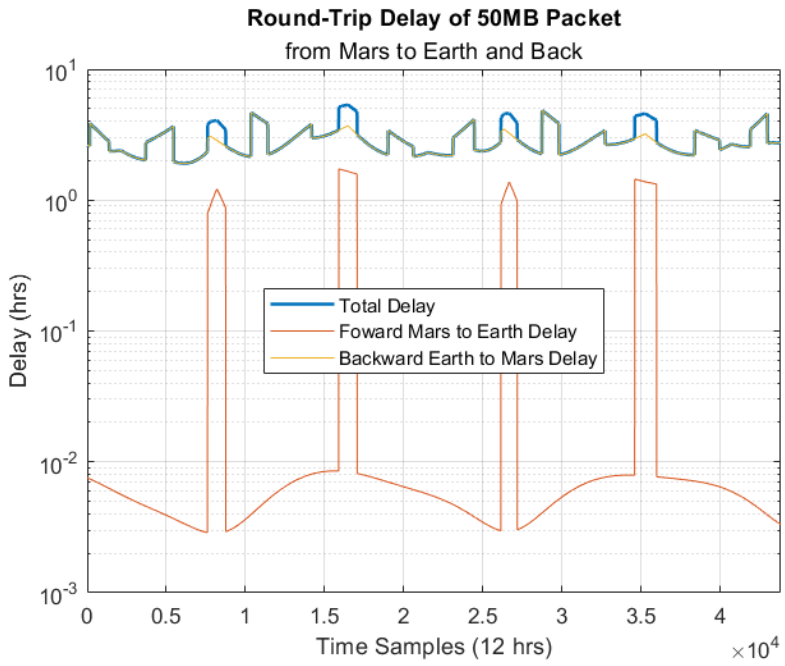

Figure 54: Round Trip Delay From Earth to Mars and Back. Asymmetry in the link forward link (Mars to Earth) vs. Backward link (Earth to Mars) is due to higher supported data rates to Earth from a larger receiving aperture. Jumps in delay are due to solar conjunction link outages.

4.5.2.3 WDMA Relay

Individual WDMA relay links support higher data rates as the link is not spread over multiple time slots. Transmission delay becomes a large component for individual links and thereby the total round-trip delay. This seems counterintuitive at first as the transmission delay is expected to go down as the capacity increases, however, this shift is due to a change in access method. TDMA transmission delay is kept low because it is bounded by the individual slot transmissions. WDMA however can transmit until transferring the full data volume, which is what this analysis assumes, subject to solar conjunction. The bottlenecks in data transfer occur between the Lagrange points and between the Mars-ML4 and Mars-ML5 points. This is due to reduced link capacity from smaller aperture sizes on the space terminal.

For brevity, the WDMA relay-specific individual links and delay figures have been removed as they are redundant with Figure 55.

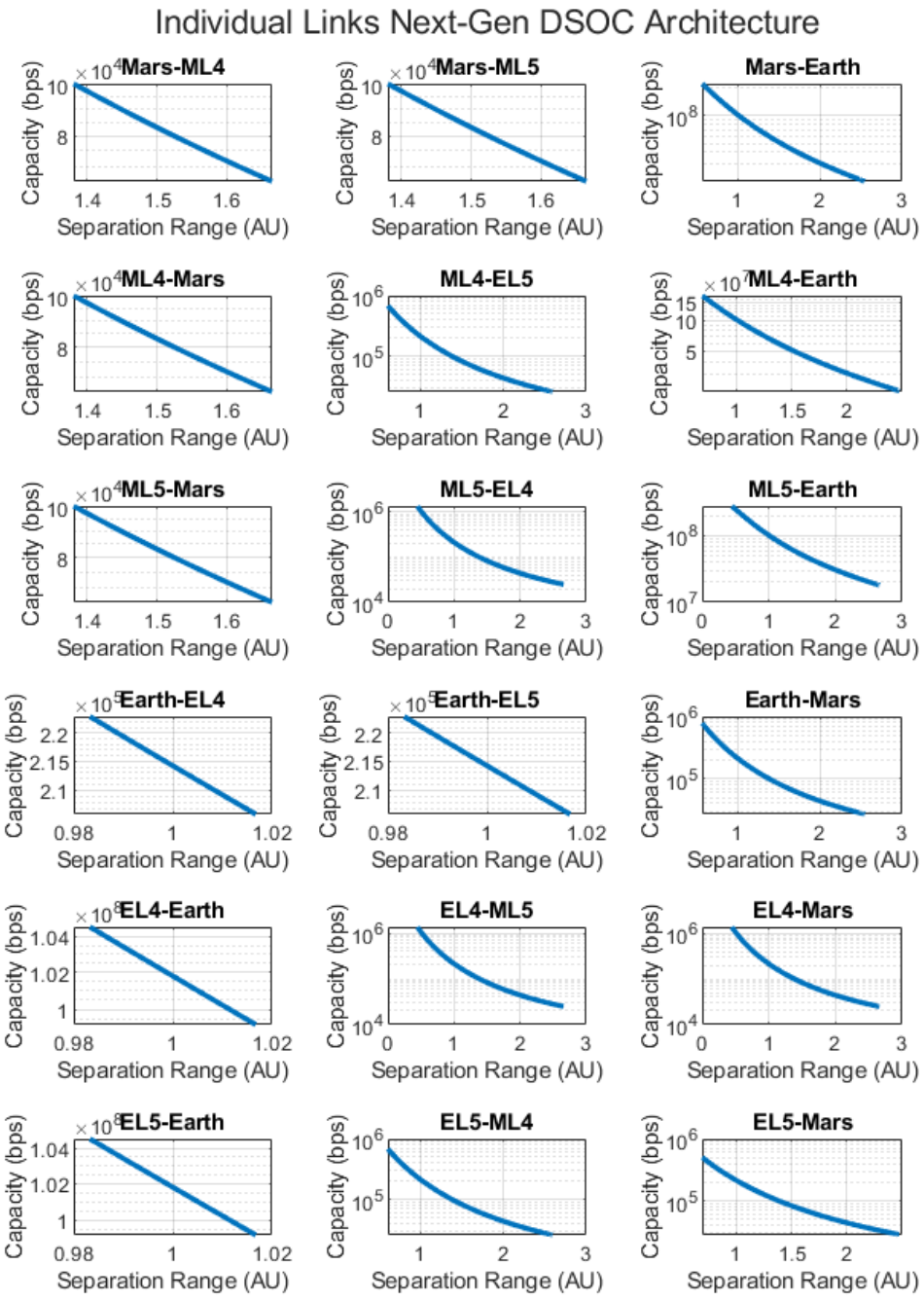

Figure 55: Individual Link Capacity vs. Range for WDMA in Deep Space

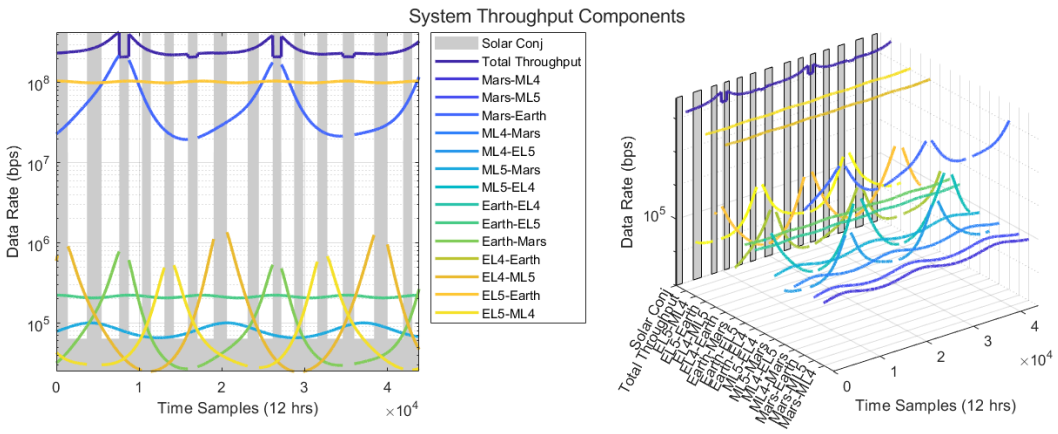

Figure 56: System Throughput for WDMA Relay in Deep Space. Solar conjunction periods are denoted in gray.

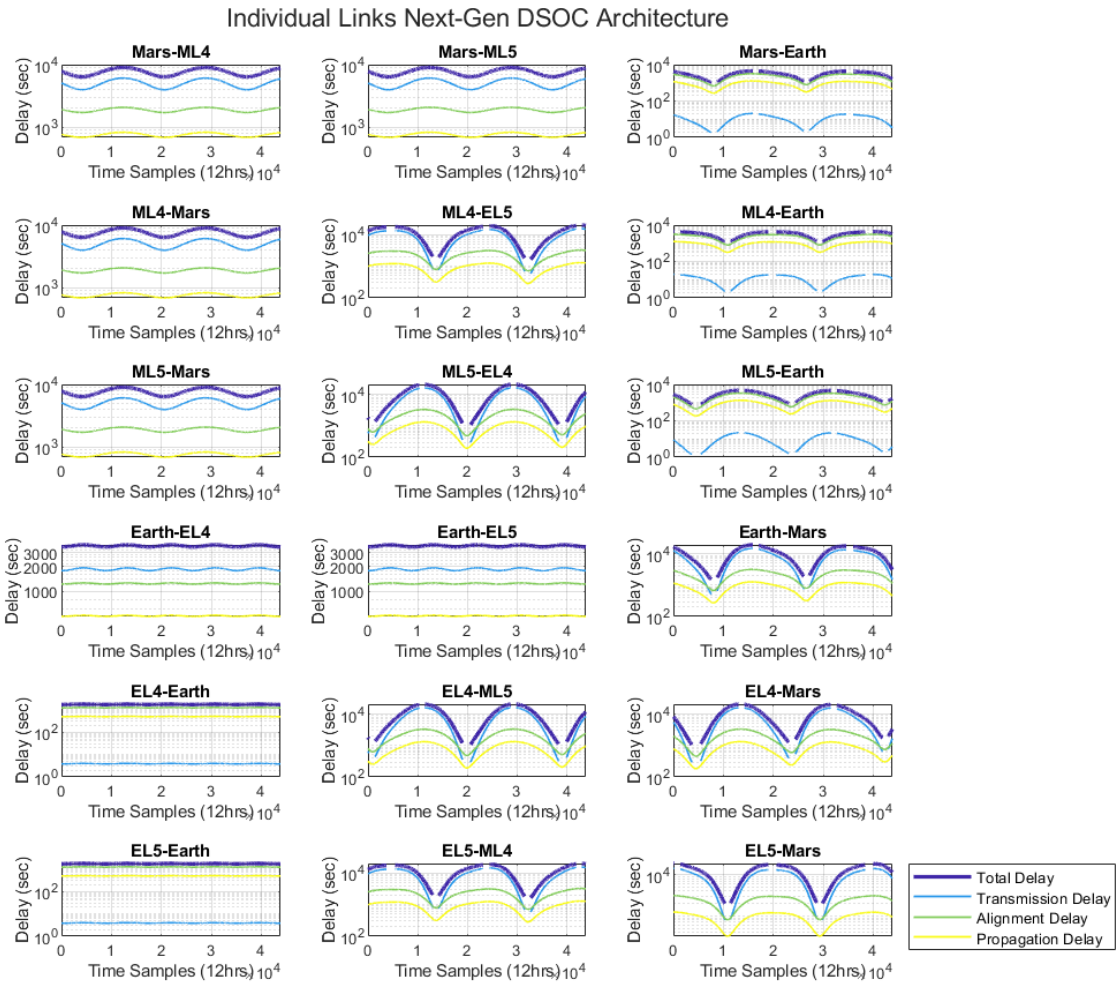

Figure 57: Individual Delay Components for WDMA in Deep Space

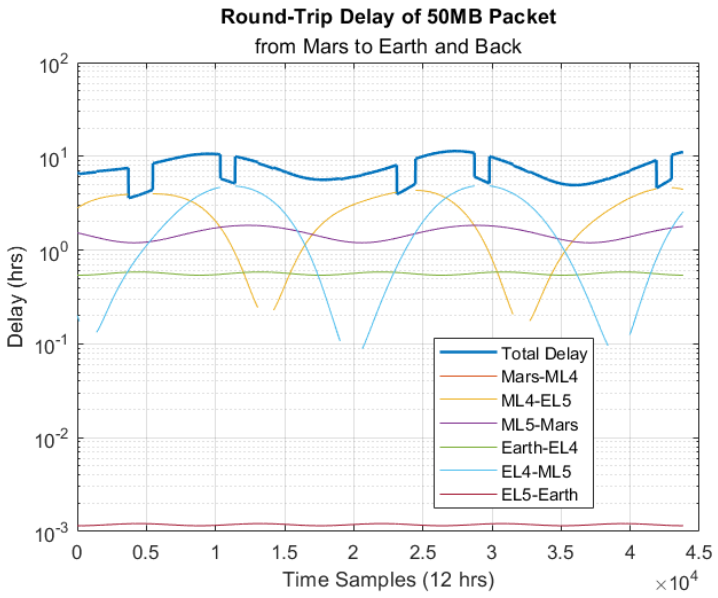

Figure 58: Round Trip Delay

4.5.2.4 WDMA Mesh

As in the TDMA case, the additional links supported by mesh boost the system capacity to its highest value of 358 Mbps. Delay is also reduced to its lowest value of 2.48 hrs. This is primarily limited by the return link from Earth to Mars. The average data rate between a direct Earth-to-Mars link is ~50 kbps due to the smaller Mars aperture size. The underlying mesh optimization doesn't typically choose this path because of the low data rate and opts to route the data to either EL4 or EL5 instead of directly to Mars. This creates another hop and a subsequent, unavoidable link between two of the space-based terminals, further increasing the round-trip delay. The forward link to Earth is much faster because of the increased link capacity.

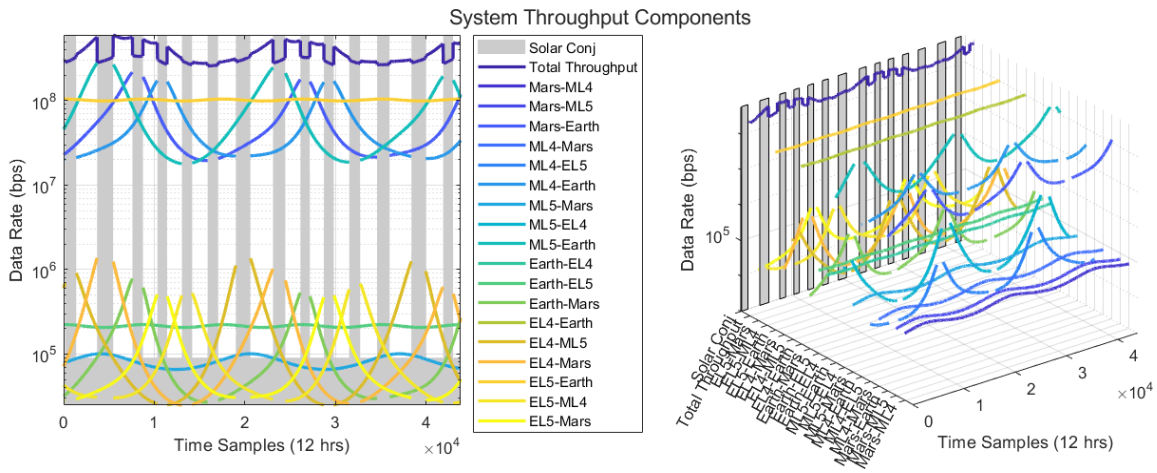

Figure 59: System Throughput for WDMA Mesh in Deep Space

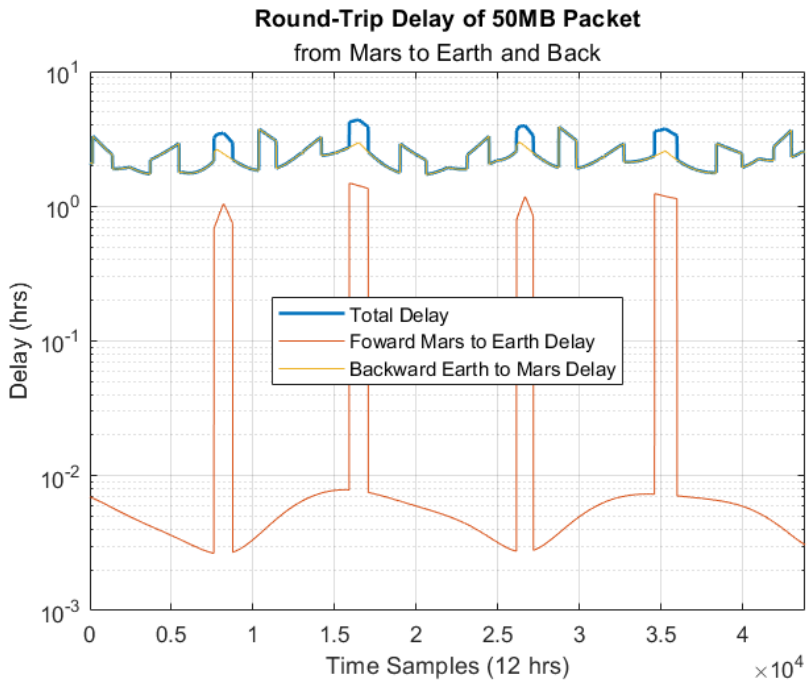

Figure 60: Round Trip Delay From Earth to Mars and Back. Sharp transitions are due to solar conjunction periods creating additional hops in the network.

4.5.2.5 TDMA vs WDMA

A comparison between all the scenarios is shown in Figure 61. A constant offset due to the inverse relationship between links and users can be seen in the TDMA systems. As in the LEO systems,

WDMA is difficult to outperform. Mesh continues to offer the highest system throughput due to the increased number of supported links.

Table 20: Summary of Access Method and Network Configuration Performance for Deep Space

	TDMA		WDMA	
	Relay	**Mesh**	**Relay**	**Mesh**
Max Delay (hrs)	11.36	5.36	10.49	4.39
Min Delay (hrs)	3.59	1.91	3.32	1.72
Average Delay (hrs)	7.34	2.97	6.78	2.48
Max Data Rate (Mbps)	71.02	100.25	426.13	601.52
Min Data Rate (Mbps)	34.43	42.96	206.59	257.74
Average Data Rate (Mbps)	42.26	59.75	253.58	358.49

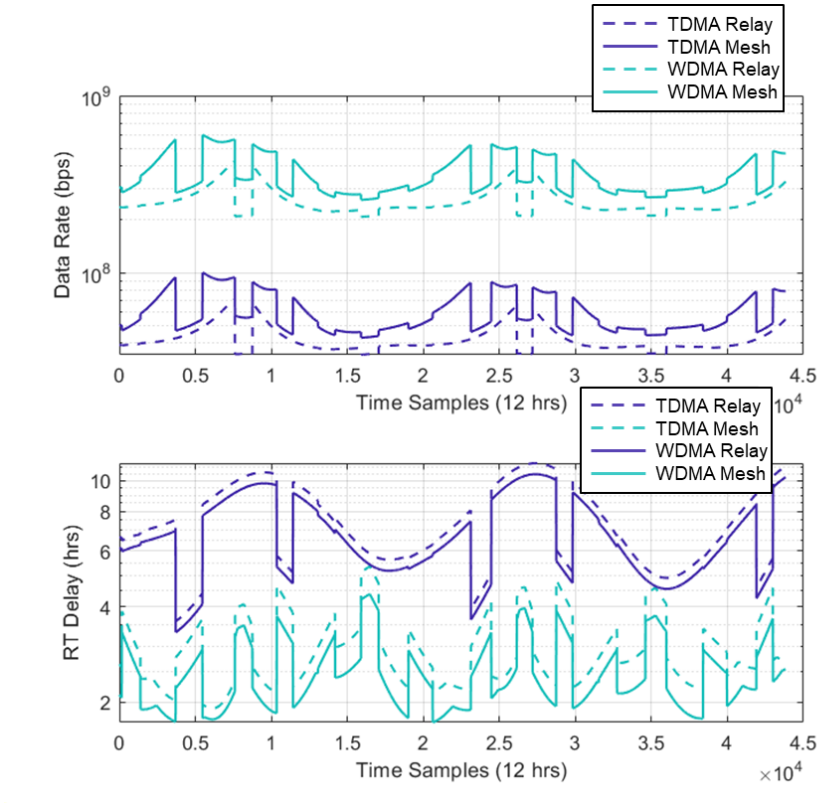

Figure 61: Access Method and Network Configuration Comparison for Deep Space

4.5.2.5 PICs vs Fiber

A single case is used to compare PICs to their fiber terminal counterparts. In order to be a competitive candidate, especially for deep-space applications which require higher levels of fidelity to operate, PICs must outperform fiber based terminals. Summarized in Section 4.5.2.5, WDMA mesh networks are the highest performer, followed by WDMA relay networks. Figure 62 shows the throughput performance of WDMA PICs vs. fiber terminals.

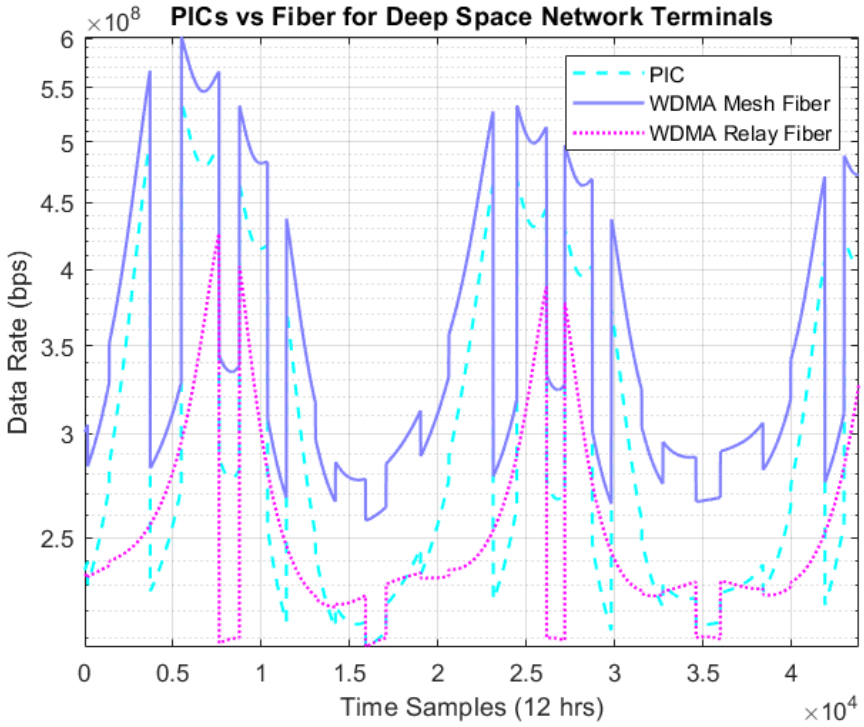

Figure 62: PICs vs Fiber in WDMA for Deep Space. Additional bandwidth is assumed for the PIC to manage the radiation-induced wavelength shift.

The mean throughput of the PIC-based transceiver is 297.6 Mbps, which is 44 Mbps higher than WDMA relay and 60.9 Mbps lower than the WDMA mesh. From the WDMA trade studies, the mass of a fiber-based terminal with 6 users at 20-W output power and 50-cm aperture is 173.1 kg and the corresponding PIC mass is 134.67 kg. Note that 3 users are selected instead of 6 as a maximum of 3 links are sustained at any given time, resulting in a frequency reuse factor of 2. The resulting mass efficiency is 1.5 Mbps/kg for the WDMA relay, 2.1 Mbps/kg for the WDMA mesh, and 2.2 Mbps/kg for the PIC mesh. From a mass efficiency perspective, the PIC terminal is the best option for the deep-space network despite its lower overall system throughput. The outstanding

question on how to achieve high output power with PICs is omnipresent, and no solution currently exists to achieve 20 W of output power. Even with something like a spatial power combining amplifier at optical frequencies, at least twenty, 1-W PICs would be required to achieve the desired output power, and likely closer to 25 or 30 accounting for losses in the cavity and electro-optic conversion. Synchronization is also key in spatial power combining, and though it has been demonstrated at lower rates [97], spatial power combining at narrow slot widths and high data rates has yet to be demonstrated.

Additionally, early data on PICs suggest radiation sensitivity. The deep-space environment is drastically different than the LEO environment and deep-space mission durations are typically longer. These two factors increase the likelihood of an anomalous event, and PICs have insufficient data to prove they are low-risk for an application in deep-space. Operational mitigations to reset charge-sensitive devices include power cycling on-orbit that can lead to gaps in network coverage if hand-off is not managed properly. Depending on the end-user, unexpected gaps in coverage could be detrimental to the mission (e.g., rover commanding or human communications).

Concerns still remain due to limited output power, limited knowledge about radiation effects on lifetimes, and need for improvement in throughput for PICs. Although Mbps/kg is higher, it may be better to pursue a WDMA mesh network using a fiber-based terminal until these factors can be mitigated.

Chapter 5

Summary and Future Work

5.1 Conclusion

In this thesis, we address supporting multiple simultaneous users in laser communication systems by analyzing the impacts of access methods to network performance, performing trade studies between protocols to understand the limitations and considerations of each, and use a model to evaluate the performance of a LEO and Deep-Space system that can support multiple simultaneous optical links using the proposed protocols. Current transceiver hardware, such as fiber-based systems, are compared with novel PIC technology that could greatly reduce the overall SWaP per terminal. The key metrics for evaluating system performance are system throughput, system delay, and mass efficiency, which give insights into how fast the network can send and receive data as well as the mass (used as a proxy for larger SWaP implications) required to achieve the given performance.

Fulfillment of contribution 1: Development of a Multiuser Lasercom Protocol

Using values found from trade studies, TDMA and WDMA are evaluated along with different network configurations for the LEO and deep space network to find the top performing protocol enabling space-based multi-user optical communications. We show that WDMA support the highest average system throughput and lowest average round-trip delay compared with TDMA. Networks configured with a mesh architecture, wherein all users can connect with all or most of the other users, further improves the throughput and data rate of both systems. In LEO, the average maximum throughput of a 4-user system is 12 Gbps and average round-trip delay is 1.6 seconds.

By using a PIC-based transmitter, the mass efficiency of a LEO terminal can be increased to 6.8 Gbps/kg, suggesting that small satellite and cubesat platforms could achieve 2.5 times higher SWaP efficiency than fiber-based terminals.

The average maximum throughput of the WDMA mesh network in deep space is 358.5 Mbps and the average round trip delay is 2.48 hrs, primarily limited by lower data rates between space-based nodes with small apertures.

PICs offer a slight mass efficiency advantage but cannot support higher system throughput compared to its fiber counterpart. Due to low TRL, higher environmental risks, and higher safety margins required for deep space missions, fiber terminals are recommended for this system.

Fulfillment of contribution 2: Design of a Multiuser Lasercom System

The design and analysis of a space-based laser communication system supporting multiple users is accomplished through the LEO and deep space network scenarios. The LEO case uses an existing LEO cubesat swarm mission, ISOC in Q4, as a baseline. The orbital parameters required for co-orbiting and doppler shift management to ensure crosslink viability are new considerations in this work. For the deep space mission, a network providing continuous coverage between Earth and Mars is designed with spacecraft positioned at the L4 and L5 Lagrange points of each planet.

Fulfillment of contribution 3: Model Verification

The primary uncertainty in modeling an optical communication system stems from estimating the key performance parameters, especially capacity. We validate the performance of this model for a single, point-to-point link space-based optical communication system, DSOC. Compared with existing models, this work estimates the performance of the DSOC system within the current best estimates. Once single link performance was validated, protocol validation is performed by comparing this work to a proposed terrestrial 5G backhaul network using optical communications. A maximum error of 3.5% is found, which shows the underlying assumption for the system level performance generally agrees with current state-of-the-art. The model is then applied to new systems.

5.1 Future Work

Further analysis and design are required to determine if PICs offer a viable alternative to fiber amplifiers. Addressing the power limitations from a device perspective may be infeasible, but alternative solutions exist to overcome single-device power limitations, such as spatial power combining. There are a few key challenges in designing a multi-user PIC-based WDMA terminal that require further investigation:

- Optical resonant cavity design akin to RF SPCAs to sustain short-pulse, high peak-power modulation methods, such as PPM.

- Synchronization methods for commanding multiple PICs simultaneously.
- Collimating and correcting poor output beam quality, an unfortunate characteristic of high-power PICs.
- Free-space optics design tolerant of multiple wavelengths spanning the full C-band. This work assumes the full C-band can be coupled from free-space to fiber where it can be subsequently demultiplexed based on wavelength, but the underlying free-space to fiber design is non-trivial. In a lens-based system, chromatic aberrations change the focal length of the system for different wavelengths. This can result in wavelength-dependent insertion loss wherein a few users will have a lower and potentially link-prohibitive SNR. Mirrors are difficult to manufacture and require tighter alignment tolerances due to their 2X angle multiplier *i.e.*, a small misalignment θ results in a 2θ beam misalignment. There is an implicit manufacturability question given multiple terminals are required to form the proposed networks and maintain precision alignment across all terminals may be infeasible.
- Environmental testing to determine PIC reliability and quantify risks.

From a modeling perspective, this work could be extended to mega-constellations to evaluate and improve system performance. This work only captures the performance of systems using PPM, which is optimal for photon-starved links such as deep-space, but limits the performance in an environment like LEO. Extending this model to include other modulations schemes, such as BPSK, DPSK, QPSK, etc., would give more representative outputs for systems using coherent communications.

Additional protocols or hybrid protocols could be added to expand trade studies and inform future system design. We analyze WDMA and TDMA, but the performance of the combination of the two and eliminated options, such as contentious multiple access methods (e.g., Carrier Sense Multiple Access) or CDMA, SDMA, etc., with multiuser optical communications is unknown. Tailoring a custom protocol that is tolerant to long propagation delay times (i.e., for deep-space) would also be beneficial.

References

[1] D. O. Caplan, “Laser communication transmitter and receiver design,” in *Journal of Optical and Fiber Communications Reports*, 2007, vol. 4, no. 4–5, pp. 225–362.

[2] S. Dolinar, B. Moision, and B. Erkmen, “Fundamentals of Free-Space Optical Communication Keck Institute for Space Studies (KISS) Workshop on Quantum Communication, Sensing and Measurement in Space Pasadena, CA,” 2012.

[3] H. Hemmati, “Deep Space Optical Communications,” in *Deep Space Communications and Navigation Series*, 2005.

[4] M. de Kok, J. Velazco, and M. Bentum, “CubeSat Array for Detection of RF Emissions from Exoplanets using Inter-Satellite Optical Communicators,” in *2020 IEEE Aerospace Conference*, 2020, pp. 1–12.

[5] C. Payne *et al.*, “Laser Crosslink Atmospheric Sounder to Investigate the Effects of Deep Convection on Ozone,” in *32nd Annual AIAA/USU Conference on Small Satellites*, 2018.

[6] J. Wiener, “Application for Fixed Satellite Service by Telesat Canada,” *https://fcc.report/IBFS/SAT-PDR-20161115-00108*, 2016. .

[7] L. Space Exploration Holdings, “Spacex APPLICATION FOR BLANKET LICENSED EARTH STATIONS - Application Narrative,” 2019.

[8] L. Space Exploration Holdings, “Spacex Non-Geostationary Satellite System - Attachment A to FCC Application,” 2016.

[9] L. Space Exploration Holdings, “Spacex non-geostationary satellite system - Attachment A to FCC application,” 2018.

[10] J. Hindin, “Application for Fixed Satellite Service by Kuiper Systems LLC,” *https://fcc.report/IBFS/SAT-LOA-20190704-00057*, 2019. .

[11] The Consultative Committee for Space Data Systems, “RATIONALE, SCENARIOS, AND REQUIREMENTS FOR DTN IN SPACE INFORMATIONAL REPORT,” 2010.

[12] D. Isreal, J. Schier, A. Petro, W. Tai, E. Anzalone, and A. Sharma, “LunaNet Architecture and Concept of Operations,” in *16th International Conference on Space Operations*, 2021.

[13] A. Seas, B. Robinson, T. Shih, F. Khatri, and M. Brumfield, “Optical communications systems for NASA’s human space flight missions,” *https://doi.org/10.1117/12.2535936*, vol. 11180, pp. 182–191, Jul. 2019.

[14] A. C. Clarke, “Extra-Terrestrial Relays,” *Wireless World*, Aug-1945.

[15] H. Keller and H. Salzwedel, “Link strategy for the mobile satellite system iridium,” in *IEEE Vehicular Technology Conference*, 1996, vol. 2, pp. 1220–1224.

[16] I. del Portillo, B. G. Cameron, and E. F. Crawley, “A technical comparison of three low earth orbit satellite constellation systems to provide global broadband,” *Acta Astronaut.*, vol. 159, pp. 123–135, Jun. 2019.

[17] H. Sanchez *et al.*, “Starling1: Swarm Technology Demonstration,” in *Small Satellite Conference*, 2018.

[18] “About TDRS.” [Online]. Available: https://nssdc.gsfc.nasa.gov/multi/tdrs.html. [Accessed: 25-Feb-2022].

[19] “NASA’s Laser Communications Tech, Science Experiment Safely in Space | NASA.” [Online]. Available: https://www.nasa.gov/press-release/nasa-s-laser-communications-tech-science-experiment-safely-in-space-0. [Accessed: 25-Feb-2022].

[20] D. M. Cornwell, “NASA’s optical communications program for 2017 and beyond,” *2017 IEEE Int. Conf. Sp. Opt. Syst. Appl. ICSOS 2017*, pp. 10–14, May 2018.

[21] “Communications with Earth - NASA Mars.” [Online]. Available: https://mars.nasa.gov/mars2020/mission/communications/. [Accessed: 25-Feb-2022].

[22] H. Yoon, “Pointing system performance analysis for optical inter-satellite communication on CubeSats,” Massachusetts Institute of Technology, Cambridge, 2017.

[23] E. Clements *et al.*, “Nanosatellite optical downlink experiment: design, simulation, and

prototyping," *Opt. Eng.*, vol. 55, no. 11, p. 111610, Sep. 2016.

[24] J. Godles and R. Terry, "Telesat Canada requests modification of its authorization to provide US market access from its NGSO low earth orbit constellation," *https://fcc.report/IBFS/SAT-MPL-20200526-00053*, 2020. .

[25] L. Space Exploration Holdings, "Spacex V-Band Non-Geostationary Satellite System - Attachment A to FCC Application," 2017.

[26] "Optical Communications Benefits | NASA." [Online]. Available: https://www.nasa.gov/directorates/heo/scan/opticalcommunications/benefits/. [Accessed: 22-Feb-2022].

[27] E. A. Park, D. Cornwell, and D. Israel, "NASA's Next Generation ≥100 Gbps Optical Communications Relay," *IEEE Aerosp. Conf. Proc.*, vol. 2019-March, Mar. 2019.

[28] E. Clements, "Probabilistic methods for systems engineering with application to nanosatellite laser communications," Massachusetts Institute of Technology, Cambridge, 2018.

[29] Federal Communications Commission, "REGULATORY FEES FACT SHEET FY 2021 REGULATORY FEES-INTERNATIONAL AND SATELLITE SERVICES," 2021.

[30] Federal Communications Commission, "FCC Fact Sheet Streamlining Licensing Procedures for Small Satellites," 2018.

[31] K. Araki *et al.*, "Experimental operations of laser communication equipment onboard ETS-VI satellite," in *Free-Space Laser Communication Technologies IX*, 1997, vol. 2990, pp. 264–275.

[32] T. Tolker-Nielsen and G. Oppenhauser, "In-orbit test result of an operational optical intersatellite link between ARTEMIS and SPOT4, SILEX," in *Free-Space Laser Communication Technologies XIV*, 2002, vol. 4635, pp. 1–15.

[33] A. Alonso, M. Reyes, and Z. Sodnik, "Performance of satellite-to-ground communications link between ARTEMIS and the Optical Ground Station," in *Optics in Atmospheric Propagation and Adaptive Systems VII*, 2004, vol. 5572, p. 372.

[34] Y. Fujiwara *et al.*, “Optical inter-orbit communications engineering test satellite (OICETS),” *Acta Astronaut.*, vol. 61, no. 1–6, pp. 163–175, Jun. 2007.

[35] R. Fields *et al.*, “NFIRE-to-TerraSAR-X laser communication results: satellite pointing, disturbances, and other attributes consistent with successful performance,” in *Sensors and Systems for Space Applications III*, 2009, vol. 7330, p. 73300Q.

[36] H. Zech *et al.*, “LCT for EDRS: LEO to GEO optical communications at 1,8 Gbps between Alphasat and Sentinel 1a,” in *Unmanned/Unattended Sensors and Sensor Networks XI; and Advanced Free-Space Optical Communication Techniques and Applications*, 2015, vol. 9647, p. 96470J.

[37] J. M. Perdigues *et al.*, “The ESA’s optical ground station for the EDRS-A LCT in-orbit test campaign: upgrades and test results,” in *https://doi.org/10.1117/12.2296098*, 2017, vol. 10562, pp. 833–841.

[38] D. Tröndle *et al.*, “Alphasat-Sentinel-1A optical inter-satellite links: run-up for the European data relay satellite system,” in *Free-Space Laser Communication and Atmospheric Propagation XXVIII*, 2016, vol. 9739, p. 973902.

[39] F. Heine, G. Mühlnikel, H. Zech, S. Philipp-May, and R. Meyer, “The European Data Relay System, high speed laser based data links,” in *2014 7th Advanced Satellite Multimedia Systems Conference and the 13th Signal Processing for Space Communications Workshop, ASMS/SPSC 2014*, 2014, vol. 2014-January, pp. 284–286.

[40] D. M. Boroson *et al.*, “Overview and results of the Lunar Laser Communication Demonstration,” in *Free-Space Laser Communication and Atmospheric Propagation XXVI*, 2014, vol. 8971, p. 89710S.

[41] B. S. Robinson, D. M. Boroson, D. A. Burianek, and D. V. Murphy, “Overview of the lunar laser communications demonstration,” in *Free-Space Laser Communication Technologies XXIII*, 2011, vol. 7923, p. 792302.

[42] B. V. Oaida, M. J. Abrahamson, R. J. Witoff, J. N. Bowles Martinez, and D. A. Zayas, “OPALS: An optical communications technology demonstration from the International Space Station,” in

IEEE Aerospace Conference Proceedings, 2013.

[43] O. V. Sindiy, M. J. Abrahamson, A. Biswas, M. W. Wright, J. H. Padams, and A. L. Konyha, "Lessons learned from optical payload for lasercomm science (OPALS) mission operations," in *AIAA SPACE 2015 Conference and Exposition*, 2015.

[44] D. R. Kolev *et al.*, "Overview of international experiment campaign with small optical transponder (SOTA)," in *2015 IEEE International Conference on Space Optical Systems and Applications, ICSOS 2015*, 2016.

[45] H. Takenaka *et al.*, "Experimental results of satellite-to-ground laser communications link through atmospheric turbulence using SOTA," in *https://doi.org/10.1117/12.2296179*, 2017, vol. 10562, pp. 1252–1259.

[46] Z. Sodnik, N. Karafolas, B. Cugny, C. Fuchs, and C. Schmidt, "Update on DLR's OSIRIS program," in *https://doi.org/10.1117/12.2535937*, 2019, vol. 11180, pp. 192–200.

[47] C. Schmidt and C. Fuchs, "The OSIRIS program - First results and Outlook," in *2017 IEEE International Conference on Space Optical Systems and Applications, ICSOS 2017*, 2018, pp. 19–22.

[48] T. S. Rose *et al.*, "Optical communications downlink from a 1.5U Cubesat: OCSD program," in *International Conference on Space Optics — ICSO 2018*, 2018, vol. 11180.

[49] C. Henry, "SpaceX launches 60 Starlink satellites, begins constellation buildout." .

[50] "Space-based Laser Communication Market - A Global and Regional Analysis: Focus on End User, Application, Solution, Component, and Range - Analysis and Forecast, 2021-2031." [Online]. Available: https://www.researchandmarkets.com/reports/5354614/space-based-laser-communication-market-a-global. [Accessed: 13-Feb-2022].

[51] K. Cahoy *et al.*, "The CubeSat Laser Infrared CrosslinK Mission (CLICK)," *https://doi.org/10.1117/12.2535953*, vol. 11180, pp. 358–369, Jul. 2019.

[52] P. Serra, "Integrated, Low-Power Sub-Nanosecond Timing Systems For Space Navigation and Communication," 2018.

[53] J. E. Velazco, “Omnidirectional Optical Communicator,” *IEEE Aerosp. Conf. Proc.*, vol. 2019-March, pp. 1–6, 2019.

[54] J. Velazco *et al.*, “Inter-satellite omnidirectional optical communicator for remote sensing,” in *SPIE 10769, CubeSats and NanoSats for Remote Sensing II, 107690L (2018)*, 2018, vol. 10769, pp. 157–162.

[55] A. Talamante *et al.*, “Deployable Optical Receiver Array Cubesat,” in *SSC*.

[56] B. Robinson *et al.*, “TeraByte InfraRed Delivery (TBIRD): a demonstration of large-volume direct-to-Earth data transfer from low-Earth orbit,” in *https://doi.org/10.1117/12.2295023*, 2018, vol. 10524, pp. 253–258.

[57] C. Schieler *et al.*, “NASA’s Terabyte Infrared Delivery (TBIRD) Program: Large-Volume Data Transfer from LEO,” in *SSC19-VI-02*, 2019.

[58] C. M. Schieler and B. S. Robinson, “Data volume analysis of a 100+ Gb/s LEO-to-ground optical link with ARQ,” in *SPIE 10524, Free-Space Laser Communication and Atmospheric Propagation XXX, 105240L*, 2018, no. February 2018, p. 21.

[59] H. Zech, P. Biller, F. Heine, and M. Motzigemba, “Optical intersatellite links for navigation constellations,” in *International Conference on Space Optics (ICSOS) 2018*, 2019, p. 34.

[60] H. Zech, F. Heine, and M. Motzigemba, “Laser communication terminals for data relay applications: Todays status and future developments,” *2017 IEEE Int. Conf. Sp. Opt. Syst. Appl. ICSOS 2017*, pp. 193–198, May 2018.

[61] F. F. Heine, P. Martin-Pimentel, N. Höpcke, D. Hasler, C. Rochow, and H. Zech, “Status of Tesat Lasercomms activities,” in *SPIE 11678, Free-Space Laser Communications XXXIII; 116780C (2021)*, 2021, p. 8.

[62] Mynaric, “Mynaric selected for DARPA program to lay out future optical communications terminal – Mynaric,” 20-Dec-2021. [Online]. Available: https://mynaric.com/news/mynaric-selected-for-darpa-program-to-lay-out-future-optical-communications-terminal/. [Accessed: 22-Feb-2022].

[63] S. Müncheberg, C. Gal, J. Horwath, H. Kinter, L. Martin Navajas, and M. Soutullo, “Development status and breadboard results of a laser communication terminal for large LEO constellations,” in *SPIE 11180, International Conference on Space Optics (ICSO) 2018; 1118034 (2019)*, 2019, p. 111.

[64] “Thales Alenia Space will provide the Optical Inter Satellite Links for Telesat’s Lightspeed Low Earth Orbit 298-satellite constellation | Thales Group.” [Online]. Available: https://www.thalesgroup.com/en/worldwide/space/press-release/thales-alenia-space-will-provide-optical-inter-satellite-links. [Accessed: 22-Feb-2022].

[65] B. S. Robinson *et al.*, “Laser communications for human space exploration in cislunar space: ILLUMA-T and O2O,” in *10524, Free-Space Laser Communication and Atmospheric Propagation XXX; 105240S (2018)*, 2018, p. 28.

[66] A. Biswas *et al.*, “Deep space laser communications,” *https://doi-org.libproxy.mit.edu/10.1117/12.2217428*, vol. 9739, no. 15, pp. 209–223, Mar. 2016.

[67] A. Biswas, M. Srinivasan, S. Piazzolla, and D. Hoppe, “Deep Space Optical Communications,” in *SPIE 10524, Free-Space Laser Communication and Atmospheric Propagation XXX*, 2018, no. 105240U.

[68] A. Biswas *et al.*, “Status of NASA’s Deep Space Optical Communications Technology Demonstration,” in *IEEE International Conference on Space Optical Systems and Applications*, 2017.

[69] A. N. Bozovich, “Space Qualification of Photonic Integrated Circuits (PICs) for Next Generation Optical Communications,” in *2019 NEPP Electronics Technology Workshop*, 2019.

[70] A. Bozovich, “Photonic Integrated Circuits (PICs) for Next Generation Space Applications,” in *IRTUAL 2020 NEPP Electronics Technology Workshop (ETW)*, 2020.

[71] “Cisco Transceiver Modules - Cisco 400G QSFP-DD Cable and Transceiver Modules Data Sheet - Cisco.” [Online]. Available: https://www.cisco.com/c/en/us/products/collateral/interfaces-modules/transceiver-modules/datasheet-c78-743172.html#Specifications. [Accessed: 11-Jan-2022].

[72] H. Zimmermann, “OSI Reference Model-The ISO Model of Architecture for Open Systems Interconnection,” *IEEE Trans. Commun.*, vol. 28, no. 4, pp. 425–432, 1980.

[73] “Windows Network Architecture and the OSI Model - Windows drivers | Microsoft Docs.” [Online]. Available: https://docs.microsoft.com/en-us/windows-hardware/drivers/network/windows-network-architecture-and-the-osi-model. [Accessed: 22-Feb-2022].

[74] European Telecommunications Standards Institute, “Digital Video Broadcasting (DVB); Second Generation DVB Interactive Satellite System (DVB-RCS2); Part 1: Overview and System Level specification Technical Specification,” 2014.

[75] M. Tropea, P. Fazio, F. De Rango, and A. F. Santamaria, “Novel MF-TDMA/SCPC switching algorithm for DVB-RCS/RCS2 return link in railway scenario,” *IEEE Trans. Aerosp. Electron. Syst.*, vol. 52, no. 1, pp. 275–287, Feb. 2016.

[76] A. S. Tanenbaum and D. J. Wetherall, “The Medium Access Control Sublayer,” in *Computer Networks*, 5th ed., Prentice Hall, 2011, pp. 257–355.

[77] International Telecommunication Union (ITU) Radiocommunication Sector, “P.676-9 : Attenuation by atmospheric gases,” 2012.

[78] I. del Portillo, B. Cameron, and E. Crawley, “A Technical Comparison of Three Low Earth Orbit Satellite Constellation Systems to Provide Global Broadband,” in *International Astronautical Congress*, 2018, no. October, pp. 1–5.

[79] ETSI, “Digital Video Broadcasting (DVB); Second generation framing structure, channel coding and modulation systems for Broadcasting, Interactive Services, News Gathering and other broadband satellite applications (DVB-S2),” *ETSI EN 302 307 V1.2.1*, vol. 1, pp. 1–78, 2009.

[80] General Dynamics, “2.4M C & Ku-Band Rx/Tx Antenna Series 1240.” 2012.

[81] D. Rowen *et al.*, “The NASA Optical Communications and Sensor Demonstration Program: Proximity Operations,” in *SmallSat Conference*, 2018.

[82] U. Zaman, R. Torun, A. Janzen, M. Y. Peng, J. Velazco, and O. Boyraz, “Design Tradeoffs and Challenges of Omnidirectional Optical Antenna for High Speed, Long Range Inter CubeSat Data Communication,” in *Small Satellite Conference 2018*, 2018, pp. 1–7.

[83] H. Ito, T. Tatebe, H. Abe, and T. Baba, “Wavelength-division multiplexing Si photonic crystal beam steering device for high-throughput parallel sensing,” *Opt. Express*, vol. 26, no. 20, p. 26145, 2018.

[84] W. J. Miniscalco and S. A. Lane, “Optical space-time division multiple access,” *J. Light. Technol.*, vol. 30, no. 11, pp. 1771–1785, 2012.

[85] D. M. Boroson, R. S. Bondurant, and D. V. Murphy, “LDORA: a novel laser communications receiver array architecture,” *Free. Laser Commun. Technol. XVI*, vol. 5338, p. 56, Jun. 2004.

[86] N. D. Fox, W. L. Maynard, E. S. Clarke, and R. C. Bruno, “GSFC conceptual design study for an intersatellite optical multiple access communication system,” in *Free-Space Laser Communication Technologies III*, 1991, vol. 1417, no. June 1991, p. 452.

[87] D. Divsalar, M. Thill, D. J. Israel, S. Dolinar, M. Shaw, and M. Peng, “Optical CDMA for a constellation of CubeSats,” *IEEE Aerosp. Conf. Proc.*, vol. 2018-March, pp. 1–11, 2018.

[88] R. K. Z. Sahbudin, T. T. K. Chun, S. B. A. Anas, S. Hitam, and M. Mokhtar, “SAC-OCDMA over hybrid FTTx free space optical communication networks,” *J. Telecommun. Inf. Technol.*, vol. 2015, no. 2, pp. 52–58, 2015.

[89] K. Sasaki, N. Minato, T. Ushikubo, and Y. Arimoto, “First OCDMA experimental demonstration over free space and optical fiber link,” in *OFC/NFOEC 2008 - 2008 Conference on Optical Fiber Communication/National Fiber Optic Engineers Conference*, 2008, pp. 25–27.

[90] A. Jurado-Navas *et al.*, “asynchronous free-space optical CDMA communications system for last-mile access networks,” *Opt. InfoBase Conf. Pap.*, pp. 5–7, 2014.

[91] B. Hamzeh and M. Kavehrad, “OCDMA-coded free-space optical links for wireless optical-mesh networks,” in *IEEE Transactions on Communications*, 2004, vol. 52, no. 12, pp. 2165–2174.

[92] K. Sayano, I. A. Nguyen, and J. K. Chan, “Demonstration of multichannel optical CDMA for free-space communications,” in *Free-Space Laser Communication Technologies XIII*, 2001, vol. 4272, pp. 38–49.

[93] R. Radhakrishnan, W. W. Edmonson, F. Afghah, R. M. Rodriguez-Osorio, F. Pinto, and S. C. Burleigh, “Survey of Inter-Satellite Communication for Small Satellite Systems: Physical Layer to Network Layer View,” *IEEE Commun. Surv. Tutorials*, vol. 18, no. 4, pp. 2442–2473, 2016.

[94] R. Radhakrishnan, W. W. Edmonson, F. Afghah, J. Chenou, and R. M. R.-O. Q.-A. Zeng, “Optimal Multiple Access Protocol For Inter-Satellite Communication in Small Satellite System,” in *The 4S Symposium*, 2014.

[95] S. Ennis and J. Dukes, “CubeSat networks: Balancing power with satellite-to-ground data throughput,” 2017.

[96] D. O. Caplan, J. J. Carney, R. E. Lafon, and M. L. Stevens, “Design of a 40 Watt 1.55μm uplink transmitter for Lunar Laser Communications,” in *Free-Space Laser Communication Technologies XXIV*, 2012, vol. 8246, p. 82460M.

[97] D. Engin *et al.*, “Highly reliable and efficient 1.5μm-fiber-MOPA-based, high-power laser transmitter for space communication,” in *SPIE 9081, Laser Technology for Defense and Security X; 90810G (2014)*, 2014, vol. 9081.

[98] E. Clements *et al.*, “Integration and Testing of the Nanosatellite Optical Downlink Experiment,” in *Cubesat Developers Workshop*, 2017.

[99] R. Kingsbury, “Optical communications for small satellites,” Massachusetts Institute of Technology, 2015.

[100] N. Bergano *et al.*, *Optical Fiber Telecommunications IIIA*, Third. Academic Press, 1997.

[101] Z. Khan *et al.*, “Single-Mode 940 nm VCSELs with narrow divergence angles and high-power performances for fiber and free-space optical communications,” *IEEE Access*, vol. 8, pp. 72095–72101, 2020.

[102] M. Yoshikawa, A. Murakami, J. Sakurai, H. Nakayama, and T. Nakamura, "High power VCSEL devices for free space optical communications," *Proc. - Electron. Components Technol. Conf.*, vol. 2, pp. 1353–1358, 2005.

[103] S. Liverman, H. Bialek, A. Natarajan, and A. X. Wang, "VCSEL Array-Based Gigabit Free-Space Optical Femtocell Communication," *J. Light. Technol.*, vol. 38, no. 7, pp. 1659–1667, Apr. 2020.

[104] A. Sevincer, M. Bilgi, M. Yuksel, and N. Pala, "Prototyping multi-transceiver free-space-optical communication structures," in *IEEE International Conference on Communications*, 2010.

[105] A. Aguilar, J. Velazco, and K. Cahoy, "Simultaneous Optical Links with the Inter-Satellite Omnidirectional Optical Communicator," in *IEEE Aerospace Conference Proceedings*, 2020, pp. 1–8.

[106] L. D. Edmunds, C. E. Barnes, and L. Z. Scheick, "An Introduction to Space Radiation Effects on Microelectronics," May 2000.

[107] H. Zhao, S. Pinna, S. T. Brunelli, B. Song, F. Sang, and J. Klamkin, "High-power integrated indium phosphide transmitter for free-space optical communications," in *Optics InfoBase Conference Papers*, 2019, vol. Part F138-, no. LIV, pp. 2–3.

[108] H. Zhao *et al.*, "High-Power Indium Phosphide Photonic Integrated Circuits," in *IEEE Journal of Selected Topics in Quantum Electronics*, 2019, vol. 25, no. 6, pp. 1–10.

[109] A. N. Bozovich, "NEPP Space Qualification Efforts for Photonic Integrated Circuits (PICs) Sponsored by: NASA Electronics Parts and Packaging (NEPP)," in *NASA Electronic Parts and Packaging Electronics Technology Workshop (ETW)*, 2021.

[110] S. Alt, "Photonic Integrated Circuit (PIC) Device Structures: Background, Fabrication Ecosystem, Relevance to Space Systems Applications, and Discussion of Related Radiation Effects."

[111] J. Campbell, "High power diffraction-limited tapered diode lasers at 885 nm and 980 nm | SPIE Photonics West," in *SPIE Photonics West*, 2022.

[112] P. Leisher, ">3W diffraction-limited 1550 nm diode laser amplifiers for LIDAR | SPIE

Photonics West," in *SPIE Photonics West*, 2022.

[113] G. Tzintzarov and J. Cressler, "Radiation Effects in Integrated Silicon Photonic Systems," in *NASA Electronics Parts and Packaging Electronics Technology Workshop (ETW)*, 2021.

[114] F. Gambini, N. Andriolli, V. Nurra, M. Chiesa, F. Petroni, and S. Faralli, "Study of Low-Dose Long-Exposure Gamma Radiation Effects on InP DBR Cavity Lasers from Generic Integration Technology," *Lect. Notes Electr. Eng.*, vol. 550, no. 9783030119720, pp. 77–82, Sep. 2018.

[115] K. A. Dean *et al.*, "Sandia's Radiation-Tolerant Silicon and InP Photonics Platforms with Multi-Project Wafer Runs."

[116] L. Zhu and J. Zhou, "Protocol analysis and simulation of inter-satellite communication for formation flying systems," *2009 Int. Conf. Wirel. Commun. Signal Process. WCSP 2009*, no. 60971081, pp. 1–4, 2009.

[117] N. M. E. E. Appel, "Nanolink: A data link layer protocol for the Cubesat," Technische Universität München, 2015.

[118] M. Atakora and H. Chenji, "A Multicast Technique for Fixed and Mobile Optical Wireless Backhaul in 5G Networks," *IEEE Access*, vol. 6, pp. 27491–27506, 2018.

[119] J. E. Velazco, "Q4 – A CubeSat Mission to Demonstrate Omnidirectional Optical Communications," pp. 6–11, 2019.

[120] J. A. Salehi, "Code Division Multiple-Access Techniques in Optical Fiber Networks - Part I: Fundamental Principles," *IEEE Trans. Commun.*, vol. 37, no. 8, pp. 824–833, 1989.

[121] H. T. Friis, "A Note on a Simple Transmission Formula," *Proc. IRE*, vol. 34, no. 5, pp. 254–256, 1946.

[122] M. E. Thomas, "Infrared- and millimeter-wavelength continuum absorption in the atmospheric windows: Measurements and models," *Infrared Phys.*, vol. 30, no. 2, pp. 161–174, Jan. 1990.

[123] A. Biswas and S. Piazzolla, "The Atmospheric Channel."

[124] D. L. Fried, “Optical Resolution Through a Randomly Inhomogeneous Medium for Very Long and Very Short Exposures,” *JOSA, Vol. 56, Issue 10, pp. 1372-1379*, vol. 56, no. 10, pp. 1372–1379, Oct. 1966.

[125] L. Andrews and R. Phillips, “Imaging Systems Analysis,” in *Laser Beam Propagation through Random Media, Second Edition*, 2005, pp. 607–643.

[126] B. L. Edwards, D. Israel, K. Wilson, J. Moores, and A. Fletcher, “Overview of the Laser Communications Relay Demonstration Project,” in *SpaceOps 2012 Conference*, 2012.

[127] B. Moision and H. Xie, “An Approximate Link Equation for the Direct-Detected Optical PPM Link,” 2014.

[128] S. B. Alexander, *Optical Communication Receiver Design*. SPIE, 1997.

[129] A. Rosenqvist, “A Layman’s Interpretation Guide to L-band and C-band Synthetic Aperture Radar data,” 2018.

[130] “Hyperspectral MWIR Imaging System SOC750.” [Online]. Available: https://surfaceoptics.com/products/hyperspectral-imaging/soc750/. [Accessed: 11-Jan-2022].

[131] A. Biswas, H. Hemmati, S. Piazzolla, B. Moision, K. Birnbaum, and K. Quirk, “Deep-space Optical Terminals (DOT) Systems Engineering,” 2010.

[132] L. A. Coldren, “Photonic-Integrated-Circuits for Coherent Communication and Sensing,” 2018.

[133] V. Rosborough, F. Gambini, J. Snyder, L. Johansson, and J. Klamkin, “Integrated transmitter for deep space optical communications,” in *2016 IEEE Avionics and Vehicle Fiber-Optics and Photonics Conference, AVFOP 2016*, 2016, vol. 2, pp. 207–208.

[134] J. Fridlander *et al.*, “Photonic integrated transmitter for space optical communications,” in *SPIE 10910, Free-Space Laser Communications XXXI, 1091026*, 2019, vol. 1091026, no. March 2019, p. 80.

[135] M. Lu *et al.*, “Highly integrated optical heterodyne phase-locked loop with phase/frequency

detection," *Opt. Express*, vol. 20, no. 9, p. 9736, Apr. 2012.

[136] D. J. Kebort *et al.*, "Monolithic Four-Channel (QUAD) Integrated Widely Tunable Transmitter in Indium Phosphide," *IEEE J. Sel. Top. Quantum Electron.*, vol. 24, no. 1, 2018.

[137] M. L. Mashanovitch *et al.*, "Monolithic Tunable Interferometric Transmitter (TunIT) in Indium Phosphide," *IEEE J. Sel. Top. Quantum Electron.*, vol. 23, no. 6, 2017.

[138] A. Biswas, "Deep Space Optical Communications (DSOC)," in *Outer Planets Assessment Group (OPAG) Meeting*, 2014.

[139] A. Biswas, "Deep Space Optical Communications (DSOC)," in *NASA Technical Interchange Meeting on Active Optical Systems for Supporting Science, Exploration, and Aeronautics Measurements Needs*, 2018, pp. 1–4.

[140] A. Biswas *et al.*, "Status of NASA's deep space optical communication technology demonstration," in *2017 IEEE International Conference on Space Optical Systems and Applications, ICSOS 2017*, 2018, pp. 23–27.

[141] J. Taylor, D. K. Lee, and S. Shambayati, "Mars Reconnaissance Orbiter," in *Deep Space Communications*, vol. 13, J. Taylor, Ed. 2014, pp. 201–262.

[142] A. Biswas *et al.*, "Deep space laser communications," in *https://doi-org.libproxy.mit.edu/10.1117/12.2217428*, 2016, vol. 9739, no. 15, pp. 209–223.

[143] K. Alexander *et al.*, "Photon counting camera for the NASA deep space optical communication demonstration on the PSYCHE mission," *https://doi-org.libproxy.mit.edu/10.1117/12.2520617*, vol. 10978, no. 13, pp. 30–40, May 2019.

[144] M. Shaw, "Superconducting Nanowire Nanowire Single Photon Single Detectors Opportunities for HEP SNSPD Device Concept," no. December, 2019.

[145] E. E. Wollman *et al.*, "Development of superconducting nanowire single-photon detector arrays for current and future deep-space optical communication," in *International Superconductive Electronics Conference*, 2019.

[146] M. Shaw *et al.*, “Superconducting Nanowire Single Photon Detectors for Deep Space Optical Communications,” in *683rd WE-Heraeus Seminar*, 2018.

[147] M. D. Shaw *et al.*, “Arrays of WSi Superconducting Nanowire Single Photon Detectors for Deep-Space Optical Communications,” in *Conference on Lasers and Electro-Optics (CLEO)*, 2015, pp. 18–19.

[148] W. T. Roberts, “Discovery deep space optical communications (DSOC) transceiver,” *Free. Laser Commun. Atmos. Propag. XXIX*, vol. 10096, no. February 2017, p. 100960V, 2017.

[149] “Wavelength-Division Multiplexing (WDM) | Fiberlabs Inc.” [Online]. Available: https://www.fiberlabs.com/glossary/about-wdm/. [Accessed: 28-Jan-2022].

[150] J. R. Wertz, D. Everett, and J. Puschell, *Space Mission Engineering: The New SMAD*, 6th ed. Microcosm Press, 2011.

[151] The CubeSat Program, “6U CubeSat Design Specification PROVISIONAL The CubeSat Program, Cal Poly SLO 6U CubeSat Design Specification Rev. PROVISIONAL (CP-CDS-PROVISIONAL) Document Classification X Public Domain 6U CubeSat Design Specification PROVISIONAL The CubeSat Program, Cal Poly SLO CHANGE HISTORY LOG Effective Date Revision Description of Changes 6U CubeSat Design Specification PROVISIONAL The CubeSat Program, Cal Poly SLO,” 2016.

[152] OneWeb, “About Us – OneWeb Satellites.” .

[153] “Starlink - Satellite Missions - eoPortal Directory.” [Online]. Available: https://directory.eoportal.org/web/eoportal/satellite-missions/s/starlink. [Accessed: 28-Jan-2022].

[154] “In Depth | LADEE – NASA Solar System Exploration.” [Online]. Available: https://solarsystem.nasa.gov/missions/ladee/in-depth/. [Accessed: 28-Jan-2022].

[155] “Spacecraft - NASA Mars.” [Online]. Available: https://mars.nasa.gov/mro/mission/spacecraft/. [Accessed: 28-Jan-2022].

[156] R. J. Aniceto, “100 Gbps Optical Coherent Modem for Low Earth Orbit Optical Inter-Satellite

Links by Signature redacted S .. Signature redacted Signature redacted Signature redacted Signature redacted," Massachusetts Institute of Technology, 2019.

[157] The Consultative Committee for Space Data Systems (CCSDS), "Optical Communications Physical Layer Communications," 2019.

[158] Consultative Committee for Space Data Systems (CCSDS), "Optical Communications Coding and Synchronization," *Ccsds 142.0-B-1*, no. August, 2019.

[159] J. Conklin *et al.*, "Preliminary Results from the CHOMPTT Laser Time-Transfer Mission," *Proc. AIAA/USU Conf. Small Satell. SSC19-VI-03.*, 2019.

[160] K. Shtyrkova, I. Gaschits, and D. O. Caplan, "Extension of matched optical filtering to scalable multi-channel high-sensitivity photon-counting applications (Conference Presentation)," in *SPIE 11272, Free-Space Laser Communications XXXII, 112720S*, 2020, vol. 11272, p. 112720S.

[161] B. S. Robinson *et al.*, "TeraByte InfraRed Delivery (TBIRD): a demonstration of large-volume direct-to-Earth data transfer from low-Earth orbit," in *Free-Space Laser Communication and Atmospheric Propagation XXX*, 2018, vol. 105240V, p. 31.

[162] J. E. Velazco, "Omnidirectional Optical Communicator," *IEEE Aerosp. Conf. Proc.*, vol. 2019-March, Mar. 2019.

[163] L. A. Samoska *et al.*, "A W-Band Spatial Power-Combining Amplifier using GaN MMICs," *2018 15th Eur. Radar Conf. EuRAD 2018*, pp. 329–332, 2018.

[164] N. Cornish and Goddard Space Flight Center, "The Lagrange Points," 1998.

[165] C. W. Chandler, "The Case for Deep Space Telecommunications Relay Stations," 2004.

[166] "Horizons System." [Online]. Available: https://ssd.jpl.nasa.gov/horizons/app.html#/. [Accessed: 15-Jan-2022].

[167] C. M. Ho, D. D. Morabito, and R. Woo, "Solar corona effects on angle of arrival fluctuations for microwave telecommunication links during superior solar conjunction," *Radio Sci.*, vol. 43, no. 2, 2008.

Appendix A: Thruster Sizing for Co-Orbiting LEO Swarms

The proposed LEO swarm orbit is within attainable thruster maneuvers for a 6U cubesat platform. The change in velocity required to reach the desired orbits and subsequent thruster sizing can be found by solving a Hohmann transfer:

$$\Delta v = v_e - v_c$$

$$v_c = \sqrt{\frac{\mu_E}{a_c}}$$

$$v_e = \sqrt{\mu_E \left(\frac{2}{r_p} - \frac{2}{r_a + r_p}\right)}$$

$$a_c = r_p$$

Where Δv is the change in velocity required to reach a target orbit in meters per second (in this case, the target orbit is the elliptical orbit), v_c is the circular orbit velocity in meters per second, v_e is the elliptical orbit velocity in meters per second, μ_E is the standard gravitational parameter of Earth in meters cubed per seconds squared, (m^3-s^{-2}), a_c is the semimajor axis of the circular orbit, which is also equal to the periapsis distance in the elliptical orbit r_p in meters, and r_a is the apoapsis distance of the elliptical orbit in meters.

The STK analysis assumes $ISOC_0$ sits in a circular orbit of 410 km, while the others are in an elliptical orbit with apogee and perigee values of 416 km and 403 km, respectively. By assigning r_a to 6788.1×10^3 m and r_p to 6794.9×10^3 m, the change in velocity required to raise the orbit from 403 km to 416 km is 3.67 m/s.

To find the delta-v required to raise the orbit from 403 km to 410 km then circularize requires an additional Hohmann transfer iteration. To get to an elliptical orbit with a perigee altitude of 410 km from a circular orbit with an altitude of 403 km, a change in velocity of 1.98 m/s is required. Circularizing the orbit to match both perigee and apogee altitudes 410 km, requires an additional 1.98 m/s change in velocity. The total delta-v needed 403 km to a 410 km orbit raise is 3.95 m/s.

Using the VACCO Standard MiPS 857-g cold-gas thruster [VACCO], the total delta-v supported can be calculated by:

$$\Delta v = -I_{sp} g_0 \ln\left(\frac{m_{dry}}{m_{wet}}\right)$$

$$I_{sp} = \frac{T\Delta t}{\Delta m\, g_0}$$

Where Δv is the total delta-v available from the thruster, T is the total impulse in Newton seconds given as 336 N-sec for the referenced model, g_0 is the gravitational constant on Earth in meters per seconds squared, m_{dry} is the dry mass of the spacecraft in grams, m_{wet} is the wet mass including propellant in grams, I_{sp} is the thruster specific impulse Δt is the firing time for the thrusters in seconds, and Δm is the change in mass in grams.

Using the 6U mass maximum set by the cubesat standards to conform to commercial launch pods, it is assumed the wet mass of the ISOC spacecraft is 12 kg [6U_std]. Change in mass is the propellant mass, which is specified as 857 g in the VACCO datasheet [VACCO]. The dry mass then is 11.14 kg. Assuming each firing takes place in one-second intervals, the specific impulse is 39.96 sec, and the total delta-v for the VACCO thruster is 29.06 m/s, which is almost an order of magnitude higher than the required delta-v for orbital changes.